Development of Multimodal Optical System Guided by Optical Coherence Tomography

by

Sang hoon Kim

Department of Biomedical Engineering
Duke University

Date:_____
Approved:

_____
Adam Wax, Supervisor

_____
Kathryn Nightingale

_____
Sina Farsiu

_____
Michael Gehm

_____
William Brown

Dissertation submitted in partial fulfillment of
the requirements for the degree of Doctor of Philosophy in the Department of
Biomedical Engineering in the Graduate School
of Duke University

2018

ABSTRACT

Development of Multimodal Optical System Guided by Optical Coherence Tomography

by

Sang hoon Kim

Department of Biomedical Engineering
Duke University

Date:_____
Approved:

_____
Adam Wax, Supervisor

_____
Kathryn Nightingale

_____
Sina Farsiu

_____
Michael Gehm

_____
William Brown

An abstract of a dissertation submitted in partial
fulfillment of the requirements for the degree
of Doctor of Philosophy in the Department of
Biomedical Engineering in the Graduate School of
Duke University

2018

Copyright by
Sang hoon Kim
2018

Abstract

The goal of this dissertation is to develop multimodal light scattering techniques using optical coherence tomography (OCT) to improve clinical diagnosis. OCT is a non-invasive optical imaging technique that utilizes low coherence interferometry to detect reflected and scattered light from a sample to produce depth resolved images. OCT is an emerging technology for a wide range of biomedical applications, with its largest impact in the field of ophthalmology to assess retinal morphology and abnormalities. Due to its excellent axial resolution, OCT has been often jointly used with a variety of other optical techniques in multimodal platforms for enhanced characterization of biological tissues.

The first section discusses the development of a multimodal optical system that combines OCT and angle-resolved low coherence interferometry (a/LCI). Similar to OCT, a/LCI utilizes low coherence interferometry for depth gating, but instead of imaging, it measures the angular dependence of scattered light as a function of depth to retrieve depth-resolved nuclear morphology measurements. However, since a/LCI is not an imaging modality, it can produce ambiguous results when the measurements are not properly oriented to the tissue structure. Utilization of OCT can resolve this problem, by providing real time image guidance for a/LCI and ensuring proper sample orientation. Moreover, OCT enables the co-registration of light scattering measurements to specific histological layers, which significantly improves the effectiveness of nuclear

morphology determination. Thus, a multimodal system that combines OCT and a/LCI can provide a unique analysis of tissue structure that cannot be assessed using a standalone modality. Using the combined modality, this research develops quantitative biomarkers from *ex vivo* tissue samples to discriminate disease states.

The second portion of the work describes the development of a low-cost, portable OCT system that could significantly increase ease of access, particularly targeted for low resource settings. Although OCT has been adopted as the gold standard for retinal imaging in ophthalmology, the high cost of the clinical system has restricted access to mostly large eye centers and laboratories. Cost reduction and portability have been of interest for numerous optical technologies. Providing a comprehensive low-cost OCT system will open the doors for a wide variety of potential opportunities of OCT guided diagnosis. This section discusses the design and the implementation of a low-cost system, as well as a demonstration of the imaging capabilities that could meet the required performance for retinal imaging in clinical and laboratory studies.

The last section discusses the performance of imaging fiber bundles for light delivery and collection in endoscopic a/LCI. The use of imaging bundle for coherent imaging application has been limited since coherent imaging relies on single mode illumination, which requires expensive scanning optics, to reject higher mode interference. This section investigates the application of more affordable fiber bundles to replace such costly systems. A number of commercial and custom fiber bundles that

could be used for light delivery and collection for the endoscopic probe have been carefully characterized. This characterization will not only help with developing a novel probe design for a/LCI, but also provide valuable insights into the potential application of coherent bundles for general coherent imaging including OCT.

Contents

Abstract iv

List of Tables xi

List of Figures xii

Acknowledgements xvii

1. Introduction 1

    1.1 Motivation 1

    1.2 Document Organization 5

2. Background 6

    2.1 Light Interaction in Biological Tissues 6

    2.2 Optical Coherence Tomography 7

        2.2.1 Low Coherence Interferometry 8

        2.2.2 Time Domain / Fourier Domain OCT 9

        2.2.3 Signal Processing 10

        2.2.4 Image Resolution 11

    2.3 Angle-Resolved Low Coherence Interferometry 13

        2.3.1 a/LCI Schematics 13

        2.3.2 Mie Fitting / T-Matrix Fitting 15

        2.3.3 Optical Correlation Analysis 17

3. Development of Combined 2D a/LCI and OCT Benchtop System 18

    3.1 Motivation 18

3.2 2D a/LCI System Development 19

3.3 OCT Integration with 2D a/LCI System 24

3.4 System Calibration 27

3.4.1 Correlation Calibration Phantom Fabrication 28

3.4.2 Validation of 2D Correlation Measurements 30

3.4.3 System Validation with Microsphere Phantom Measurement 37

3.5 Summary 39

4. Applying the Combined Modality to Develop Quantitative Biomarkers 41

4.1 Investigation of Rat Models of Esophageal Adenocarcinoma 42

4.1.1 Sample / Method 42

4.1.2 Analysis 44

4.1.3 Discussion 58

4.2 Early Detection of Retinal Degeneration in a Mouse Model 61

4.2.1 Preliminary Experiments 61

4.2.2 Methods for Imaging Retina in Intact Eyes 63

4.2.3 Analysis 68

4.2.4 Discussion 74

4.4 Summary 75

5. Development of Low-Cost OCT System 77

5.1 Motivation 77

5.2 Hardware Development 78

5.2.1 Spectrometer 79

5.2.1.1 Design and Implementation 79
5.2.1.2 Sensor and Triggering 82
5.2.1.3 Performance Characterization 84
5.2.2 Light Source 85
5.2.3 Scanning Optics 87
5.2.3.1 Liquid lens Scanning Implementation 87
5.2.3.2 MEMS Mirror Incorporation to Scanning Implementation 97
5.2.3.3 Reference Arm 98
5.2.4 3D Printed Housing and Optical Assemblies 99
5.3 Software Development 100
5.3.1 Synchronization 100
5.3.2 Data Acquisition and OCT Processing 103
5.4 System Characterization 105
5.4.1 System Specification Measurements 105
5.4.2 Comparison with Commercial Systems 107
5.5 System Validation on Biological Samples 109
5.5.1 Ex-vivo Measurements on Porcine Cornea 109
5.5.2 In-vivo Measurement on Mice Retina Systems 111
5.5.3 Discussion 112
5.6 Future Plan 113
5.7 Summary 115
6. Development of Multimodal OCT and a/LCI Endoscopic Probe 116

6.1 Motivation 116

6.2 Imaging Spectrometer 117

6.2.1 Design and Implementation 118

6.2.2 Performance Characterization 129

6.3 Fiber Bundles for a/LCI endoscopic probe 131

6.3.1 Fiber Bundle Characterization 133

6.3.2 OCT Imaging through Fiber Bundle 136

6.4 Summary 143

7. Conclusions 145

Reference 148

Biography 158

List of Tables

Table 3.1. Comparison of center to center spacing measurements using 2D a/LCI correlation analysis and microscope image analysis 35

Table 5.1. Component Cost of Low-Cost OCT systems..... 106

Table 5.2. Specs of the low-cost OCT engine and commercial OCT systems. 109

Table 6.1. FWHM spot size measurement (in μm) for different locations of the beam entrance height at the entrance slit. 131

Table 6.2. The effective core diameter (ECD), core to core spacing (CCS) and open area ratio (OAR) calculation for the commercial fiber bundles and custom fiber bundles. ... 136

List of Figures

Figure 2.1. Diagram of low coherence interferometry system.....8

Figure 2.2. Schematic of a) TD-OCT and b) SD-OCT.....10

Figure 2.3. Schematic of Fourier domain a/LCI system.....14

Figure 2.4. a) Comparison of 1D and 2D a/LCI measurement ranges. b) 2D a/LCI measurement of 10 μm beads. c) Mie fitting example using the beads phantom 16

Figure 3.1. Wavelength measurement of Ti:Sapphire laser (a) before and (b) after spectral broadening.....20

Figure 3.2. 2D a/LCI system schematic. 21

Figure 3.3. Zemax simulation showing the wavefront aberration of the illumination beam. (a) optimized for the collimation (b) lens facing the opposite way.....22

Figure 3.4. Zemax simulation showing the wavefront error of the illumination beam (a) optimized for collection beam (b) lens facing the opposite way.....23

Figure 3.5. System geometry of the a/LCI system combined with OCT scanner near the sample plane showing sequential imaging with 2D a/LCI and OCT 25

Figure 3.6. *En face* OCT image and cross sections of the pinhole overlaid with a/LCI beam.....26

Figure 3.7. Bright field microscope image of the fabricated scattering phantoms. a) Type "A". b) Type "B". 30

Figure 3.8. Images of scattering calibration phantom constructed via soft lithography in PDMS.....32

Figure 3.9. Center to center spacing measurement with a/LCI correlation analysis (red) and with bright field microscope image analysis (blue). 34

Figure 3.10. Bright field micscope image and a/LCI measurement of the crypt resembed sample.....37

Figure 3.11. a) OCT en face image of the 8 μm beads sample with b) a cross section. c) OCT en face image of the 10 μm beads sample with d) a cross section 38

Figure 3.12. 2D a/LCI angular scattering measurement of a) 8 μm and b) 10 μm polystyrene spherical beads embedded in PDMS. 39

Figure 4.1. OCT and a/LCI scans of EGDA rat esophagus tissue of well-prepared sample and a poorly prepared sample 45

Figure 4.2. Normalized a/LCI correlation energy vs depth for EGDA rat epithelial tissues for (a) 0 to 200 μm, (b) 10 to 13 μm, and (c) 19 to 22 μm correlation length range..... 48

Figure 4.3. Scattered measuremnet collected via 2D a/LCI corresponding to the ROI layer in Figure 4.2 and Mie fit result 50

Figure 4.4. Radial correlation energy vs correlation length at the marked ROI in Figure 4.2 in log-log scale. 53

Figure 4.5. a) Normalized a/LCI intensity for the 0.225% 260 nm polystyrene beads solution imaged at multiple depths. 54

Figure 4.6. a) Normalized a/LCI intensity and b) amplitde of fitter power law exponent for the beads solution with different number and types of averaging scheme. 55

Figure 4.7. a) Normalized a/LCI intensity and b)amplitdue of fitted power law exponent for the white card stock for different exposure time..... 56

Figure 4.8. a/LCI intensity and analysis for the beads solution, the esophageal tissue, and white paper. 58

Figure 4.9. a) OCT image of WT mice retina and b) OCT image of RhoKO mice retina taken after 2D a/LCI scan.. 62

Figure 4.10. a) OCT image of WT mice retina and b) OCT image of RhoKO mice retina taken with a high resolution OCT system.. 63

Figure 4.11. System geometry near the sample plane showing sequential imaging with 2D a/LCI and OCT. 64

Figure 4.12. OCT imaging of retinas for (a) WT, and (b) RhoKO mice. 65

Figure 4.13. *En face* OCT images of mice retina during repositioning the eye along the vertical direction. 66

Figure 4.14. OCT image of a) a fresh WT retina, and b) the same sample after an hour of experiment showing the degradation of the retinal layers over time. 67

Figure 4.15. a) OCT image of wild type mouse retina (scale bar = 100 μm). b) Scattering intensity collected via 2D a/LCI as function of depth vs polar angle θ2. 69

Figure 4.16. a) Angular scattering plane measured with 2D a/LCI and b) coorrelation plane from the same sample at the depth corresponding to OS/RPE. 69

Figure 4.17. Normalized radial correlation energy vs. correlation length obtained by azimuthal integration of correlation of the layers shown in Figure 4.16b 70

Figure 4.18. Histology images for 8 weeks old WT mice and 4, 8 and 12 weeks old RhoKO mice demonstrating the thinning of the retinal layers in RhoKO mice 72

Figure 4.19. Calculated power law exponent across 20-90 μm correlation length range for NFL, OPL and OS/RPE layers for each type of mouse 73

Figure 5.1. a) Schematic of loop spectrometer. Zemax spot diagram of the loop spectrometer design b) at 815 nm, c) 840 nm, and d) at 860 nm..... 80

Figure 5.2. a) Spectrum of the light source acquired with Awaiba sensor with the flipped pixel and after correction. b) FT of a mirror before correction and after.. 83

Figure 5.3. a) Sinewave and b) pulse train at fixed frequency captured by free running Awaiba sensor. c) OCT tape image acquired with Awaiba sensor..... 84

Figure 5.4. a) Argon calibration source spectrum measurement for wavelength calibration and FWHM measurement. b) The spectrometer falloff measurement..... 85

Figure 5.5. Power stability measurement for a) Superlum Minibut, and b) Exalos Butterfly..... 87

Figure 5.6. FWHM spot size measurement at different distance from the center for different lens orientation..... 89

Figure 5.7. FWHM spot size measurement at different distance from the center with multiple lens orientations for a) single lens, and b) double lenses. 90

Figure 5.8. The measured intensity and spot size of the beam scan at the focal plane using the two liquid lenses. 91

Figure 5.9. The measured intensity anf FWHM spot size measurement of the diagonal beam scan using two liquid lenses 92

Figure 5.10. a) The mean distance between spots when 0.1° step jumps are made across the scan. b) FWHM spot size and deviation from the center 93

Figure 5.11. a) The measured intensity of the beam scan and b) FWHM and position measurement at the focal plane with one liquid lens 94

Figure 5.12. a) OCT scan of a tape phantom on a business card. b) Liquid lenses schematics. c) OCT scan of the same sample through extra lens.. 96

Figure 5.13. a) The measured intensity and b) FWHM spot size measurement of the beam scan at the focal plane using a MEMS mirror and a liquid lens. 98

Figure 5.14. a) 3D printed spectrometer housing with mounted optics. b) Interior view of the low cost system engine and c) exterior view. 100

Figure 5.15. a) Pulse train conversion into frame trigger using Arduino. b) The control flow diagram using the Arduino for synchronization 101

Figure 5.16. The system schematic using the Arduino for synchronization. 102

Figure 5.17. The control flow diagram using LabVIEW. b) LabVIEW interface acquiring OCT B-SCAN of a tape phantom. 104

Figure 5.18. a) The OCT B-scan of a scotch tape phantom imaged by (a) low-cost OCT system and (b) Wasatch commercial system. 108

Figure 5.19. a) The OCT image of a porcine cornea, b) lens and iris and c) iridocorneal angle. 110

Figure 5.20. a) The OCT image of a murine ear, b) tail and c) back skin. 111

Figure 5.21. a) OCT image of a live mice retina. b) OCT image of the same mice showing the optical neve head. 112

Figure 6.1. Ray diagram illustration showing tangential focus and sagittal focus. 118

Figure 6.2. Czerny-Turner spectrometer design 119

Figure 6.3. a) Argon calibration source measurement with false colored yellow line at 794 nm. b) Zoomed in image showing the aberration. 120

Figure 6.4. Measured spectrum of broadband light emerging from a pinhole. 121

Figure 6.5. Diagram showing the collimated beam diameter and projected area of the grating in the spectrometer. 127

Figure 6.6. a) Zemax schematic of the imaging spectrometer, b) Seidal diagram and c) Seidal coefficient summary. 128

Figure 6.7. Zemax spot diagram of the imaging spectrometer (a) at 800 nm, (b) at 830 nm and (c) at 860 nm for different object height. 129

Figure 6.8. a) Image of broadband light emerging from a single mode fiber and b) argon calibration source measurement. 130

Figure 6.9. a) OCT image of a coverslip glass on a mirror prior to registration. b) Registered image of a). 132

Figure 6.10. The microscope image of the fiber bundle face for the three commercial bundles and the custom fiber bundles. 135

Figure 6.11. Scanning pattern captured at the distal end of the fiber bundles with both commercial bundles and custom bundles 138

Figure 6.12. The OCT scan of a distal end of the fiber bundles 140

Figure 6.13. The OCT scan of a mirror using the 5 μm core sized Collimated Holes bundles at a) 12.5 mm and b) 25 mm fiber length. 141

Figure 6.14. Scanning pattern captured at the distal end of the fiber bundles for a) 5 μm sized core, and b) 3.2 μm sized core. 142

Figure 6.15. The OCT scan of a mirror using the 4.5 μm core sized Collimated Holes bundles with a) 65 mm length and b) 250 mm length. 143

Acknowledgements

First, I would like to thank my advisor, Dr. Adam Wax for his support and guidance throughout my undergraduate research and PhD program at Duke. He has provided me with great opportunities and motivation in my research field and the work summarized here would not have been possible without his support. I would like to thank my committee members for their time and expertise. Next, I would like to thank the post-docs in the lab, who helped me to advance in research and spent many hours working on experiments together: Dr. Yizheng Zhu, Dr. Michael Giacomelli, Dr. Matt Rinehart, Dr. Thomas Matthews, Dr. Jason Maher, Dr. William Brown, Dr. Ken Chu, and Dr. Zhou. I also thank my colleagues in the lab for their friendship and collaboration: Michael Crose, Derek Ho, William Eldridge, Yang Zhao, Hansang Park, Zach Steelman, Brian Cox, Evan Jelly and Ge Song. Finally, I would like to thank my parents for their love and support.

1. Introduction

1.1 Motivation

Since its introduction in 1991, Optical Coherence Tomography (OCT) has developed over the past decades as an emerging imaging technology over a wide range of biomedical applications [1]. These include intravascular OCT (IV-OCT) for identifying at-risk atherosclerotic plaques [2], detection of neoplasia in the gastrointestinal tract [3] and other organ systems [4-7], real-time surgical guidance[8], and high resolution imaging of biological specimens [9, 10]. Furthermore, OCT has made the largest impact in the field of ophthalmology. Using its fast speed and high sensitivity to acquire *in vivo*, cross sectional image of ocular tissues, spectral domain OCT (SD-OCT) is currently recognized as the state of the art technology to identify retinal morphology and abnormalities [11-13].

In addition, for improved characterization of biological tissues, OCT has been combined with a variety of optical techniques in multimodal platforms [14-16]. Recent examples include work by Maher et al., who developed a co-localized confocal Raman spectroscopy OCT system to study the spatial distribution of topically applied drugs within tissue samples [14], and by Wang et al., who integrated two-photon luminescence with OCT imaging system for characterizing atherosclerotic plaques [15]. Liu et al. demonstrated a multimodal imaging system which combines photoacoustic microscopy and OCT to measure the metabolic rate of oxygen in small animals *in vivo* [16].

Another biomedical modality that could benefit by combining with OCT is angle-resolved low coherence interferometry (a/LCI). a/LCI is an optical technique used to study nuclear morphology in biological samples by collecting elastically scattered light from the sample for various scattering angles and utilizing interferometry to depth gate the measurements [17]. Then, in order to obtain quantitative depth-resolved nuclear morphology measurements, the angular scattering distribution from selected depths within the sample can be analyzed [18]. The enlargement of the nuclei in the basal layer of the epithelium have been shown to be a highly useful biomarker for the early detection of dysplasia, a precancerous tissue state. Therefore, previous studies have utilized a/LCI for evaluating epithelial dysplasia using the nuclear morphology data from esophageal [19], colon [20], and cervical tissue [21].

In addition to a/LCI, sub-cellular structures in tissue have been examined by other interferometric techniques. For example, optical coherence microscopy has been previously used to study morphological changes in neoplastic tissue with high spatial resolution [22]. Also, interferometric synthetic aperture microscopy (ISAM) has been developed to reconstruct the 3D distribution of scattered light from tissue [23]. In addition, micro-optical coherence tomography can greatly enhance the resolution of OCT for use as a tool for studying cellular and subcellular structures [24]. The Fourier transform light scattering (FTLS) technique obtains scattering information from measurements of the optical phase and amplitude for a thin sample [25, 26]. Despite the

high spatial resolution of these techniques, a/LCI offers the distinct advantage of subwavelength measurements of scatterer size at high depth of field while also avoiding the need for an expert observer to interpret the image features.

Previous studies have shown that a/LCI can detect dysplasia in Barrett's esophagus (BE) patients *in vivo* effectively where this precursor to esophageal adenocarcinoma (EAC) was identified with 100% sensitivity and 84% specificity [19]. However, the lack of visual guidance and coverage area using the a/LCI fiber probe have been considered as a limiting factor for clinical application. On the contrary, OCT provides a large scanning area and visual guidance to the region of the interest. Although each standalone modality is not capable of comprehensive diagnosis of dysplasia, the combined modality can provide a more accurate diagnostic tool for cancer screening.

While OCT is the gold standard for retinal imaging in ophthalmology, the high cost of clinical systems (up to $150,000) has restricted its access to mostly large eye centers and laboratories [27]. Thus, development towards a low-cost, portable OCT system could significantly increase the ease of access, particularly in low resource settings, and expand the use of OCT to a wider range of applications which were previously cost prohibitive.

Therefore, cost reduction and system portability have been of interest for numerous optical technologies for the development as point of care medical

applications. These optical imaging modalities includes fluorescence microscopy [28], computational microscopy [29] and cytometry [30]. For OCT, various portable and small OCT systems which incorporate handheld scanners have been developed by multiple research groups. Lu et al. demonstrated a handheld high speed swept-source OCT with a reduced form factor by using a MEMS mirror instead of galvanometer mirrors [31]. Also, Jung et al. developed a handheld OCT system for primary care diagnostics [32]. However, the engines of these systems (which include the light source, spectrometer, PC, and interferometer optics) are still bulky and expensive and limit application of these systems for point of care imaging. Recent efforts in developing a comprehensive low-cost OCT system include a miniaturized, low-cost, fully packaged silicon photonic integrated swept-source OCT [33] and a low-cost handheld linear OCT that could be built using only standard off-the-shelf inexpensive components [34]. However, reductions in size and cost of these systems comes with a significant sacrifice of SNR and reduced imaging depth.

In an effort to develop OCT as a point of care imaging modality, several potential approaches to significantly reduce the cost of the system were identified. First, the OCT engine can be fully constructed using commercial off-the-shelf parts to eliminate the overhead from margin stacking found in existing assemblies and sub-assemblies. In addition, a system level approach can be taken to reduce the cost in both the selection of individual parts and the total construction of the system that meets the targeted

performance, rather than focusing on optimizing an individual part. This approach will allow construction of a comprehensive low-cost portable OCT system with desired system performance despite multiple tradeoffs in component performance to reduce the total cost of the system.

1.2 Document Organization

The dissertation document is organized as follows. Chapter 2 provides literature review that gives context to technical information about light interaction in biological tissue, OCT and a/LCI including theory and image processing. The first topic presents the development of combined 2D a/LCI and OCT benchtop system and calibration process with correlation calibration phantom. The second topic discusses application of the combined 2D a/LCI and OCT modality to develop quantitative biomarkers with long range correlation analysis in *ex vivo* animal tissue. The third topic covers the development and implementation of low-cost, portable OCT system targeted for low resource setting. The fourth and final topic presents imaging fiber bundle characterization and implementation of an imaging spectrometer for development of a multimodal OCT and a/LCI endoscopic system.

2. Background

In this chapter, I present an overview of the background materials needed to provide the technological information relevant to the research presented in the remainder of this document. Section 2.1 provides insight on light interaction in biological tissue, and section 2.2 reviews the general theory and evolution of optical coherence tomography. Section 2.3 introduces the angle-resolved low coherence interferometry technique along with its processing and analysis information.

2.1 Light Interaction in Biological Tissues

Light interaction in biological tissue is mainly governed by scattering and absorption. The two optical properties of the tissue can be represented by scattering coefficient, μ_s and absorption coefficient μ_a which are reciprocally related to the scattering mean free path (MFP) and absorption MFP [35]. The scattering MFP describes the average distance a photon travels before being scattered, and the absorption MFP defines the average distance traveled by a photon before being absorbed. The sum of the scattering coefficient and absorption coefficient yield total attenuation of the tissue and the light penetration in shallow tissue can be described by the attenuation coefficient [36].

Since light penetration depth is limited in tissue, the absorption and scattering coefficient must be minimized in order to maximize the maximal imaging depth. Absorption and scattering are wavelength dependent, and melanin and hemoglobin are

the dominant absorber in tissue which exhibit high absorption at visible and near infrared wavelength [37]. Therefore, the optimal wavelength window for imaging deep within biological tissue lies between 700 nm and 1,300 nm [38]. In this region, the scattering coefficient is generally a few to several orders of magnitude higher than the absorption coefficient [39].

Optical scattering in tissue can be modeled by light scattering in a medium with a continuous but varying refractive index or scattering by discrete particles with surrounding media [40]. Since organelles such as cell nuclei, mitochondria, and other cytoplasmic organelles contribute most to the local index of refraction, light scattering in tissue can be approximated as scattering by discrete sphere or spheroids [41]. For the continuum scattering theory, the tissue is rather composed of interconnected material with different length scales, and the tissue is described with a refractive index correlation function [42].

2.2 Optical Coherence Tomography

Optical coherence tomography (OCT) is an optical technique analogous to ultrasound and based on low coherence interferometry [1]. In order to measure the time of flight for the traveling light, the scattered light from sample is compared with the light that has traveled a known distance through a reference path. Interference of the two light can be demodulated in order to calculate the difference between the distances traveled by the light in the two separate paths. In this section, the theory behind OCT is

provided including a description of OCT system schematic, time domain and Fourier domain OCT, signal processing, and parameters that govern image resolution.

2.2.1 Low Coherence Interferometry

In a typical OCT system, light from a low coherence source is split into a sample beam and a reference beam by a Michelson interferometer scheme as shown in Figure 2.1. Light from the reference path is reflected from a reference mirror and recombined with the sample field at the beam splitter. Similarly, the backscattered light from sample is recombined with the reference arm light and interfered before entering a detector. When low coherence source is employed, the interference of the sample light and reference light is only observed when the distance traveled by each light path is within the coherence length of the light source which is inversely proportional to the bandwidth of the light source [43].

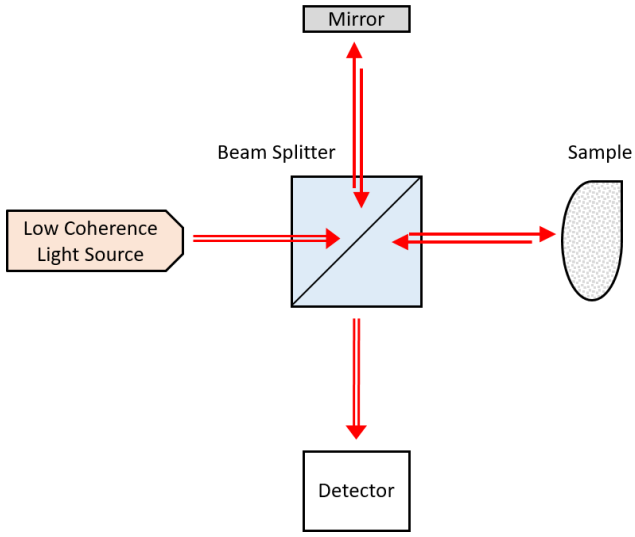

Figure 2.1. Diagram of low coherence interferometry system

2.2.2 Time Domain / Fourier Domain OCT

In a time-domain OCT (TD-OCT) system, a broadband source and a single-channel photodiode are implemented with a position adjustable reference mirror. The light in the sample arm is focused and delivered to the sample by a scanning mirror which is used to scan the focused spot across the sample plane. The path length of the reference arm is manually controlled to achieve path length difference between the sample and reference arms to retrieve the sample reflectivity profile at each depth as shown in Figure 2.2a. However, in recent years, Fourier domain OCT has replaced time domain OCT due to its superior signal to noise ratio resulting from simultaneous multiplexed acquisition [44-46]. Fourier domain OCT is divided into spectral domain OCT (SD-OCT) and swept source OCT (SS-OCT) and the path length of the reference arm is fixed for both Fourier domain systems [47]. In SS-OCT, a single channel photo detector is employed but the source is rapidly swept in wavelength to achieve narrow instantaneous linewidth. In SD-OCT, a broadband light source is used but the collected light is dispersed in wavelength and detected simultaneously with a multi-pixel detector spectrometer instead of a single channel photodetector (Figure 2.2b). The spectrometer spatially separates the interfered beams by wavelength and the dispersed beam is simultaneously recorded on a detector array. The following chapters in the document focus on discussion and utilization of SD-OCT systems.

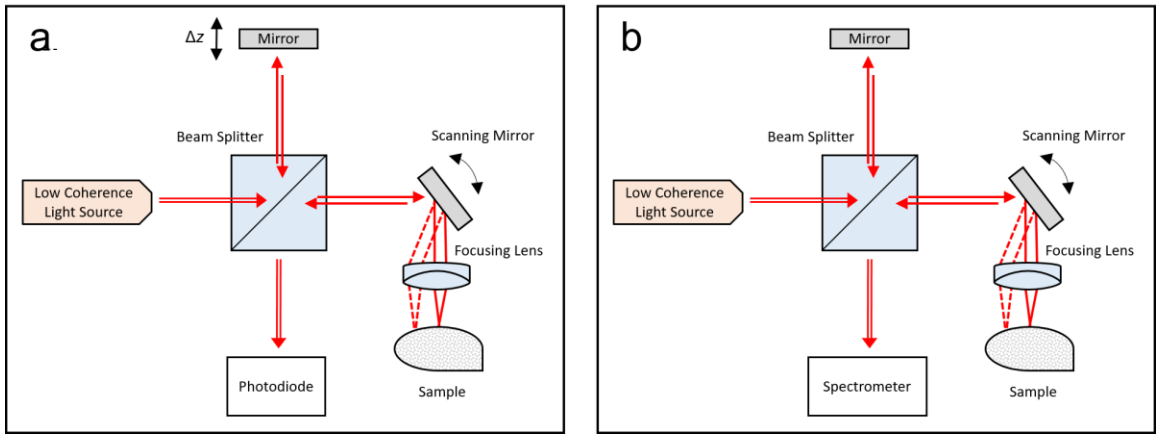

Figure 2.2. Schematic of a) TD-OCT and b) SD-OCT.

2.2.3 Signal Processing

The spectral interference pattern captured by the spectrometer in SD-OCT contains a depth resolved reflection profile of the sample, which can be recovered in post-processing. The signal, I, detected by the spectrometer is given by: [48]

$$I = E_S^{\ 2} + E_R^{\ 2} + 2\,\mathrm{Re}[E_S E_R \cos(2\Delta z k + \phi)], \tag{2.1}$$

where E_s and E_R are the sample and reference fields, $k = 2\pi/\lambda$ is the wavenumber, Δz is the optical path length (OPL) difference between the sample and reference arms, and ϕ is the phase term. The first 2 terms of the equation 2.1 correspond to the intensities of the sample and reference fields while the third term represent the interference between the sample and reference light. The last term can be modulated by the wavenumber of the source and the OPL difference between the sample and the reference arms, where OPL is defined as,

$$OPL = \int_C n(s)ds \qquad 2.2$$

where $n(s)$ is refractive index as function of distance s along path C. In a media of constant index of refraction, OPL can be simply calculated by index of refraction times the physical distance. In SD-OCT, the acquired signal is evenly spaced in wavelength with a grating spectrometer. However, due to chromatic aberration and other wavefront aberrations including spherical aberration, the detected signal is often fitted with a second order or higher polynomial model [49]. Since depth is linear with wave number k, instead of wavelength, interpolation from wavelength space into even wave number space is conducted before taking a Fourier transform, which yields a depth resolved reflection profile of the sample [50]. Additionally, numerical dispersion compensation is generally performed in the Fourier transform step in order to compensate for difference in optical elements between the sample arm and the reference arm [51]. Dispersion mismatch arises due to wavelength dependent propagation speed in the different optical materials in the two arms of the interferometer. This mismatch can be either physically corrected by matching the optics in the sample and reference paths, or it can be corrected numerically by imposing a frequency dependent phase delay in the signal processing steps [52].

2.2.4 Image Resolution

Axial resolution of an OCT system is defined by the coherence length, l_c, of the broadband source by [47],

$$l_c = \frac{2\ln(2)}{\pi}\frac{\lambda_o^2}{\Delta\lambda} \qquad 2.3$$

where λo represent the center wavelength of the source and $\Delta\lambda$ is the full width at half maximum (FWHM) of the source bandwidth. As described in section 2.2.1, interference can be only observed when the difference in path length of sample beam and reference beam is within the coherence length of the source. In order to achieve high axial resolution, OCT requires a broadband source which has a low coherence length for the given center wavelength.

The lateral resolution of OCT systems is simply defined by the spot size at the focal plane similar to that of confocal microscopy [47]. The lateral point spread function of an OCT system, δ_x, can be calculated by,

$$\delta_x = 0.37\frac{\lambda_o}{NA}. \qquad 2.4$$

λo denotes the center wavelength of the source, and NA represent numerical aperture of focusing optics. In order to achieve higher lateral resolution for a given wavelength, the focusing optics in the sample arm must have a high NA. However, there is a tradeoff between the depth of focus and lateral resolution. Therefore, a high NA system would produce a tightly focused spot at the sample plane but with a reduced axial field of view and vice versa.

2.3 Angle-Resolved Low Coherence Interferometry

Angle-resolved low coherence interferometry (a/LCI) collects the angularly scattered light from a sample and utilizes low coherence interferometry to obtain the depth-resolved angular scattering profile of the sample [53]. The angular scattering profile can then be analyzed at each depth using an inverse light scattering model for quantitative analysis of the sample structure. In this section, a/LCI schematics and signal processing using inverse light scattering models are discussed.

2.3.1 a/LCI Schematics

Similar to OCT, the first a/LCI system was developed based on time domain low coherence interferometry and serial scanning with a scanning lens was employed for resolve each scattering angle [53]. However, the system has evolved into a Fourier domain system, and utilization of an imaging spectrometer further facilitated parallel detection of angle dependent scattered light [54, 55]. Different from OCT, the a/LCI system does not share common illumination and collection paths. Therefore, a Mach-Zehnder interferometer scheme is employed instead of a Michelson interferometer design. A simple Fourier domain a/LCI scheme using a Mach-Zehnder interferometer is shown in Figure 2.3.

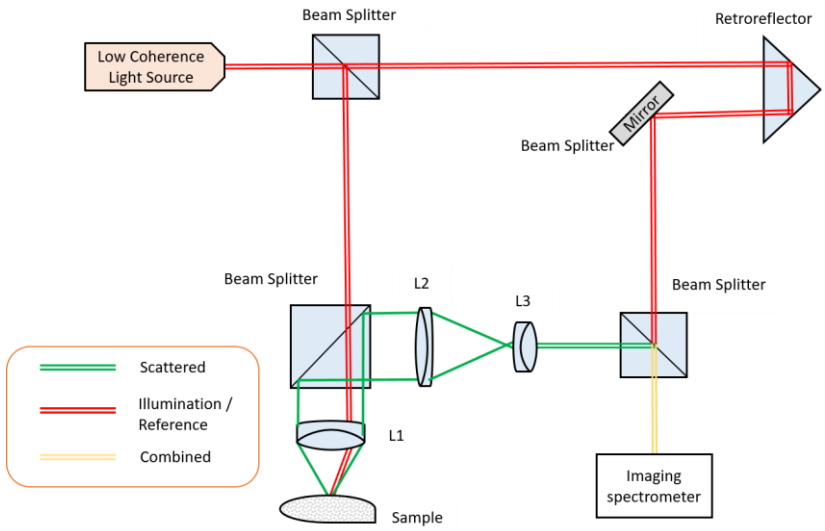

Figure 2.3. Schematic of Fourier domain a/LCI system. L1 lens is offset from the incoming beam in order to illuminate the sample at an angle, and L2 and L3 are used to demagnify the beam size to match the sensor dimension. Red light represent illumination beam and reference beam, green light represent the scattered beam, and yellow light represent the combined beam. Utilization of an imaging spectrometer enable parallel detection of multiple scattering angle.

A major difference between OCT and a/LCI lies in the illumination scheme. a/LCI utilizes a collimated beam instead of a focused spot on a sample, and the illumination beam is incident onto the sample at an angle relative to the optical axis to increase the detectable angular scattering range and avoid specular reflections as shown in Figure 2.3. In OCT, the illumination beam is focused to a few microns on the sample plane which determines the lateral resolution of the OCT system. However, the a/LCI illumination beam is delivered as a collimated beam since the angular scattering information collected with a focused beam will be convolved with the angular span of that beam. In addition, a larger beam diameter, up to a few hundred microns, is required for a/LCI in order to collect the averaged scattering signature from a number of

scatterers at the region of interest (ROI). Recently, the technique has been further developed into a two dimensional technique, 2D a/LCI, by incorporating a scanning galvanometer at the sample collection path [56]. The scanning mirror enables light in different scattering planes to be overlapped at the entrance slit of the spectrometer to detect the entire scattering field in the two transverse scattering planes for various depths within the sample, providing a more detailed description of the scattering structure [57]. A detailed description of 2D a/LCI implementation is described in section 3.2. The 1D and 2D a/LCI measurement range are superimposed on a simulated scattering pattern of a 10 μm polystyrene bead phantom for comparison in Figure 2.4a.

2.3.2 Mie Fitting / T-Matrix Fitting

In order to retrieve nuclear morphology information from an a/LCI angular scattering measurement, the collected data are compared to known scattering theories such as Mie theory or T-Matrix calculations [58]. Mie theory is an exact solution that describes the scattering of an electromagnetic plane wave by a homogeneous sphere whereas T-matrix extends the light scattering model to nonspherical particles [59, 60]. Both scattering theories treat scattering media as discrete particles instead of a continuous random media. Although T-matrix based fitting may provide a more precise model of the scatterer, calculation and fitting of the T-matrix solution requires comparison of the entire 2D scattering field, making it much more computationally intensive compared to Mie theory.

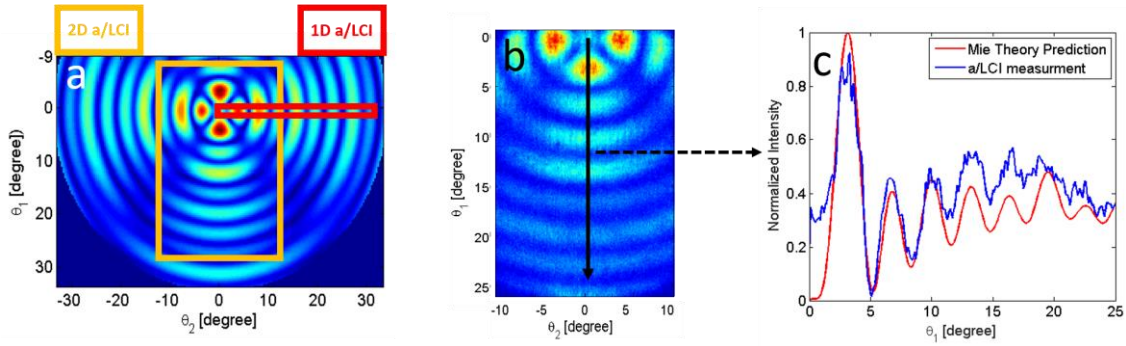

Figure 2.4. a) Comparison of 1D and 2D a/LCI measurement ranges superimposed on a simulated scattering pattern of a 10 μm polystyrene bead. b) 2D a/LCI measurement of 10 μm polystyrene beads in PDMS. The black arrow represents a 1D a/LCI angular profile selected for Mie fitting. c) Low pass filtered a/LCI scattering measurement (blue line) compared to the best Mie theory fit (red line). Figure taken from [61].

For both theory based fitting, a library of simulated scattering distributions is generated for a given source wavelength with varying scatterer size, size % distribution, index of refraction of the scatterer, and index of refraction of the media. Then the depth of interest in the a/LCI measurement is determined and the angular scattering profile from the selected depth is extracted as shown in Figure 2.4b. The angular scattering data is then low pass filtered and de-trended using a second order polynomial subtraction to remove scattering contributions from length scales greater than and smaller than the range of interest. Finally, the processed data are compared to each scattering distribution within the simulated database and the best fit is found using the chi-squared error as shown in Figure 2.4c. In order to ensure the uniqueness of the predicted Mie fit, the chi-squared value of the best fit must first be greater than the chi-squared value when compared to the null solution. Secondly, the chi-squared value of the best fit must be

significantly greater than that of the next best fit by more than 10%. If either criteria is not met, the fit is determined to be a non-unique solution and discarded [18].

2.3.3 Optical Correlation Analysis

In the Mie fitting procedure described above, the high frequency Mie oscillation is filtered out in order to exclude the contribution from the scattering structure much greater than size of the nuclei. However, useful information about scattering structure could be extracted from the filtered portion of the scattering data. A previous study demonstrated that the Fourier transformation of the angular scattering distribution yields the two-point correlation function of the optical field in the Born approximation [53]. The angular distribution of scattered intensity is given by

$$\mathcal{F}[|E(\Theta)|^2] = \mathcal{F}[I(\Theta)] = \Gamma_E(r), \tag{2.5}$$

where $E(\theta)$ is the angular distribution of scattering field, F represents Fourier transform and r is the length scale of the spatial correlation. Therefore, through the Fourier relationship, the achieved spatial resolution of the correlation function is determined by the measured angular range of the scattered field. Similarly, the greatest detectable correlation length is determined by the angular sampling resolution of the scattered field. Example of two dimensional optical correlation using a/LCI measurement is provided in section 3.4.2.

3. Development of Combined 2D a/LCI and OCT Benchtop System

In this chapter, we describe the development of a combined 2D a/LCI and OCT benchtop system. The a/LCI sample arm optics have been redesigned to accommodate an OCT sample arm which was incorporated using a flip mirror to image a co-registered FOV on the same focal plane. The previous 2D a/LCI instrument that was described briefly in section 2.3.1 had a system geometry where the illumination beam was incident from the bottom of the sample [56]. In order to image an intact eyeball, as well as *in-vivo* tissues from an animal model, the 2D a/LCI has been rebuilt to illuminate from the top of the sample instead of the bottom. For system calibration, a 2D phantom was fabricated using photolithography, and the fabrication of the phantom and coregistration/calibration processes are described in detail.

3.1 Motivation

A number of optical techniques have been combined with OCT in multimodal platforms to enhance characterization of biological tissues as described in section 1.1. However, even though a/LCI shares a common depth gating scheme with OCT based on coherence gating, the two modalities have not been combined previously. A multimodal system that combines a/LCI and OCT will provide unique analysis of biological sample structure that cannot be obtained using a single modality alone. OCT can resolve histological layers due to its high axial resolution, and can serve as image guidance for

a/LCI measurements. In addition, a/LCI can resolve sub-cellular features such as nuclear diameter and long range spatial correlations which are limited for OCT imaging due to the lack of transverse resolution and the limited physical dimension of the focused OCT beam. Thus, the two modalities complement each other, and the combined multimodal system will allow better localization of structural features in biological samples and provide a more effective analysis of the depth resolved scattering information.

3.2 2D a/LCI System Development

Light output from a Ti:Sapphire laser (Coherent, Mira-900F, λ = 800 nm) is coupled into a spool of polarization maintaining fiber (50 m, RC PM 850, Corning) for spectral broadening via self-phase modulation. The self-phase modulation results from the optical Kerr nonlinear effect which occurs when intense light propagates through media such as crystals and glasses. The index of refraction of the media is altered by the intense propagating light itself which modifies the propagation properties [62]. After spectral broadening, the light has a bandwidth of 45 nm (FWHM) as shown in the Figure 3.1.

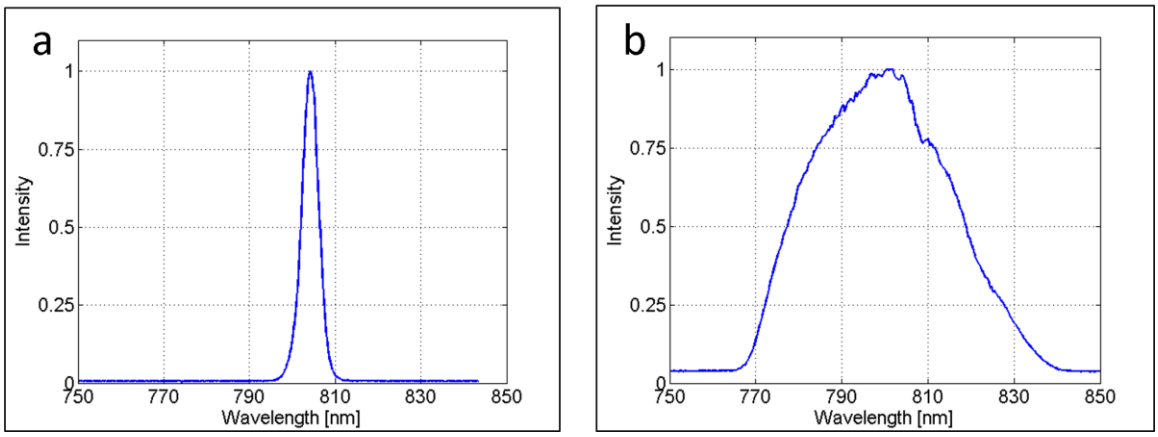

Figure 3.1. Wavelength measurement of Ti:Sapphire laser (a) before and (b) after spectral broadening. The FWHM of the original spectrum is measured to be 4 nm and that of the broadened spectrum is measured to be 45 nm.

The light is split into sample and reference arms in a Mach-Zehnder interferometer using 90:10 fiber splitter (Figure 3.2), and each arm is collimated with a f=10 mm achromatic doublet lens (L1 and L8, Thorlabs, AC050-010-B-ML). The light in the sample and reference arms is p-polarized by a linear film polarizer and a fiber polarization controller (not shown). The light in the sample arm is delivered to the sample following a beam expander composed of a f=150 mm and a f=30 mm achromatic doublet lenses (L2 and L3 Thorlabs, AC254-150-B-ML, and AC254-30-B-ML respectively) resulting in an approximate 400 μm beam diameter at the sample.

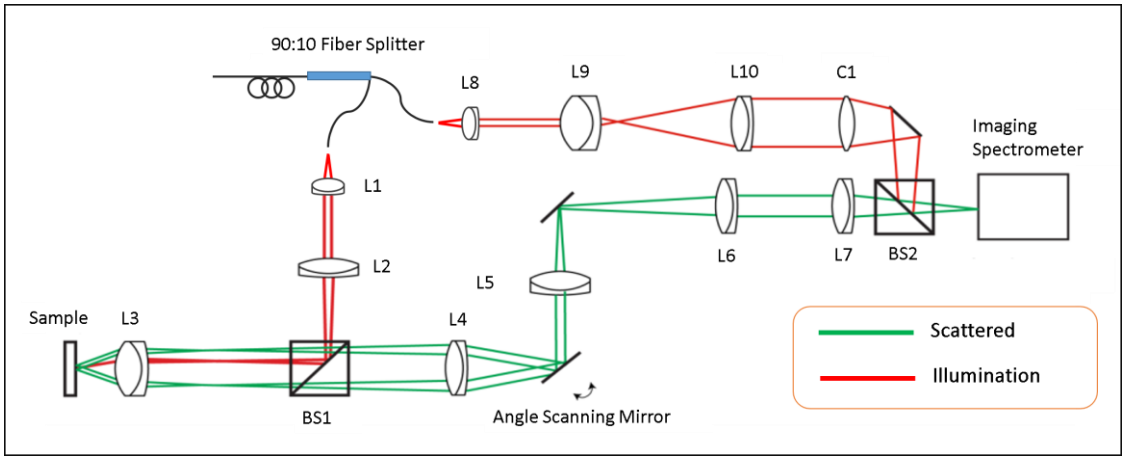

Figure 3.2. 2D a/LCI system schematic. Light from Ti:Sapphire laser (λ = 800 nm, $\Delta\lambda$ = 45 nm) is split into an input to the sample and reference beam (red). Light scattered by the sample (green) is interfered with reference beam and imaged on the entrance slit of the imaging spectrometer for parallel line scan detection. A scanning galvanometer located in between L4 and L5 enable the detection of angle-resolved scattered field over a range of solid angles. Figure taken from [61].

The sample beam, however, is off center at the L3 lens of the beam expander such that, the sample beam has an incidence angle of approximately 13°. When aligning the L3 lens, it is crucial to have the infinity corrected side facing away from the sample. One can be easily tempted to optimize the alignment based on illumination beam shape by placing the L3 lens with the infinity corrected side facing toward sample for better collimation of the illumination beam. However, the illumination beam only uses small fraction of the lens aperture and the collimation error and spherical aberration arising from the less optimized orientation of the lens is fairly small as shown in Figure 3.3, regardless of the orientation. Even when the beam is translated toward the edge of the lens to produce the 13° angle of the incidence beam (red line in Figure 3.3), the illumination beam remain fairly well collimated on both cases.

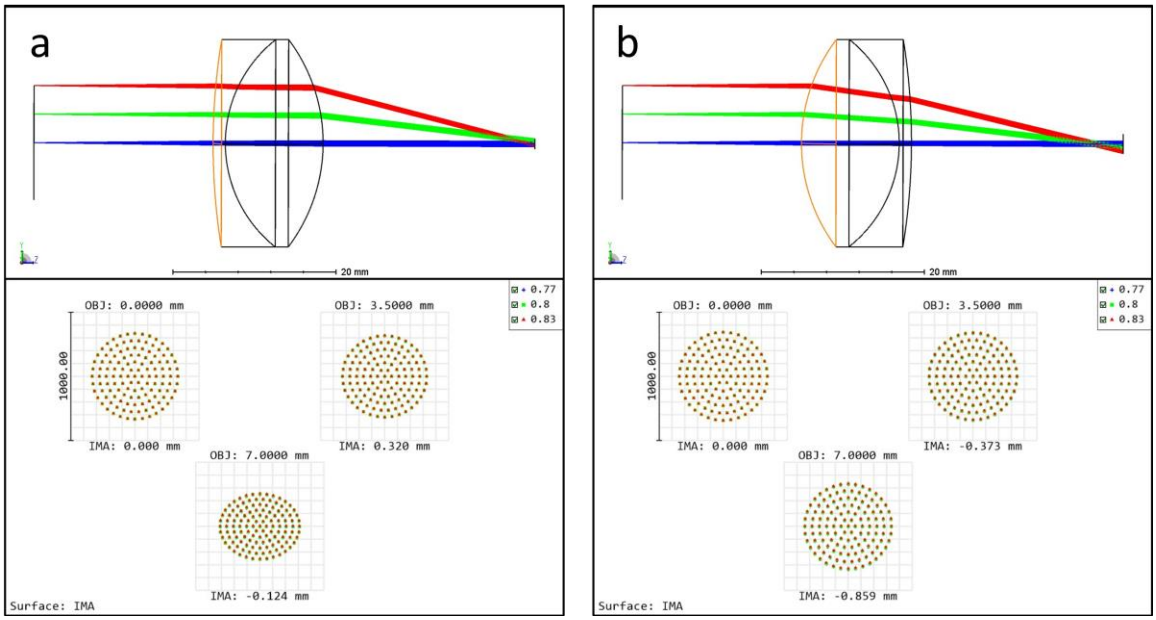

Figure 3.3. Zemax simulation showing the wavefront aberration of the illumination beam (a) when the lens orientation is optimized for the collimation of the illumination beam (infinity corrected side facing toward the sample plane), and (b) when the lens orientation is facing the opposite way (infinity corrected side facing away from the sample plane). The blue beam travels through the optical axis of the lens, green beam hits the sample plane at incidence angle of 6.6° and the red beam hits the sample plane at incidence angle of 13°.

This aberration in the illumination path is very minor compared to the aberration from the collection side when the incorrect lens orientation is implemented. Unlike the illumination path, the collected scattered light uses the entire numerical aperture (NA) of the lens, so that the spherical aberration is at least an order of magnitude higher if the lens is set up with an incorrect orientation as shown in Figure 3.4.

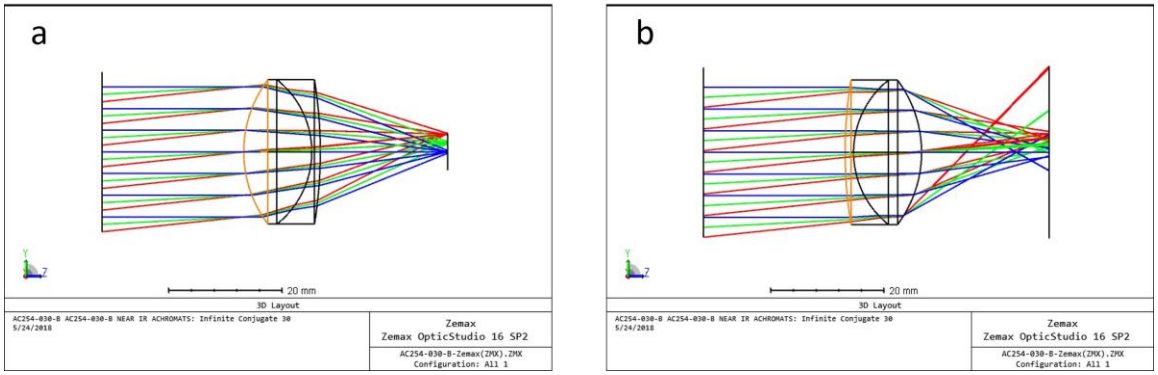

Figure 3.4. Zemax simulation showing the wavefront error of the illumination beam (a) when the lens orientation is optimized for collection beam (infinitely corrected side facing away from the sample plane), and (b) when the lens orientation is facing the opposite way (infinitely corrected side facing toward the sample plane).

Unlike the previous 2D a/LCI system in section 2.3.1, a fold mirror is inserted before the L3 lens to allow the illumination beam to strike the sample from the top. Light scattered by the sample is propagated to the entrance slit of the imaging spectrometer (Princeton instruments, SP-2150) which is located at a conjugate Fourier plane to the sample. The imaging spectrometer has a 150 mm focal length and uses a 600 lp/mm grating. For parallel acquisition of light in one scattering plane, a 640 by 480 pixel CCD array (AVT, Pike F-032) with 7.4 μm square pixel is used as a sensor for the imaging spectrometer. The longer dimension is used for the spectral dimension and the shorter dimension is used for parallel spatial collection, with each channel corresponding to a particular scattering angle. Since the scattered light field collected by the 1 inch lens has a much larger dimension than the size of the sensor, the collected scattered light is demagnified by a factor of 4 using a f=200 mm achromatic doublet and a f=50 mm achromatic doublets lenses (L6 and L7, Thorlabs, AC254-200-B-ML and AC254-050-B-

ML, respectively) to fit within the sensor dimension. The reference field is expanded to match the sensor height (L9 and L10), then focused at the spectrometer slit using a cylindrical lens (C1, Thorlabs, LJ1629RM-B). The sample field is interfered with the reference field at the 90:10 (T/R) beam splitter (BS2) before entering the spectrometer slit. The 90:10 fiber splitter and beam splitter are used to maximize the sample scattered field intensity in Mach-Zehnder setup.

As opposed to OCT which implements a spatial scan, the galvanometer in the 2D a/LCI scheme (Cambridge Technology, 6200H series) sweeps across the Fourier plane of the scattered field, permitting parallel line scan detection of the angle-resolved scattered field over a range of solid angles. The total angular range of this detection scheme is 0.59 rad (34°) along the galvanometer scanning direction and 0.37 rad (21°) along the parallel detection direction. The achieved angular resolution is 0.137° and the system acquires one 2D scattering plane in 4 ms (1 ms integration, 3 ms read out). When 600 angular scans are implemented in an angular scanning step size of 0.057 ° over the scanning axis, the entire 2D scattering field acquisition takes approximately 2 seconds.

3.3 OCT Integration with 2D a/LCI System

The unique aspect of this 2D a/LCI system is the integration of an OCT system for direct comparisons of a/LCI measurements and OCT images of the same region of interest (ROI). A commercial OCT system (Wasatch Photonics, Spark) with λ = 830 nm and $\Delta\lambda$ = 155 nm was incorporated into the multimodal system. The OCT system has

much higher bandwidth compared to the a/LCI system, thus providing excellent axial resolution and depth information. The OCT system has a maximum imaging depth of 1.9 mm, and nominal axial resolution and lateral resolution of 2.0 μm.

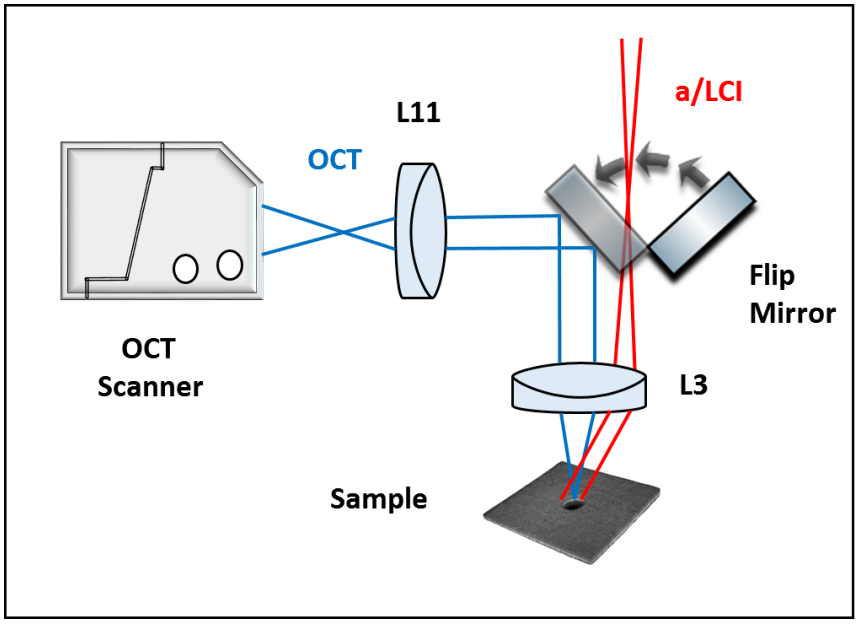

Figure 3.5. System geometry of the a/LCI system combined with OCT scanner near the sample plane showing sequential imaging with 2D a/LCI and OCT. Figure taken from [61].

In order to insert the OCT scanner within the 2D a/LCI system, the OCT beam is relayed through a 4f system to the sample plane. Short focal length lenses (L11, L3, f= 30 mm) are chosen to create the 4f configuration to maintain a unit magnification and to ensure a high enough NA to achieve the desired angular collection range for a/LCI measurements. Additionally, a flip mirror is inserted within the 4f relay to easily switch between the two modalities as shown in Figure 3.5. Thus, although the combined system does not provide simultaneous imaging of the same ROI, each modality can sequentially

access the identical ROI without relocating the sample by just altering the position of the flip mirror. In order to overlap the a/LCI beam with OCT FOV, the 400 μm a/LCI beam is first passed through a 1 mm diameter pinhole at the sample plane. Then, the pinhole is centered in the 5 x 5 mm OCT FOV at the identical sample plane (Figure 3.5). In addition to coregistration of the FOV, the focal plane of the OCT has been matched to that of the a/LCI. The pinhole is placed at the focal plane of the a/LCI first, then the OCT scanner is moved in and out to align its focus at the identical sample plane. The OCT image of the pinhole centered at the center of the OCT FOV which is overlaid with a/LCI illumination beam is shown in Figure 3.6. After the integration of the OCT scanner using the 4f relay, the axial and lateral resolution were measured to be 2.6 μm and 12.3 μm, respectively.

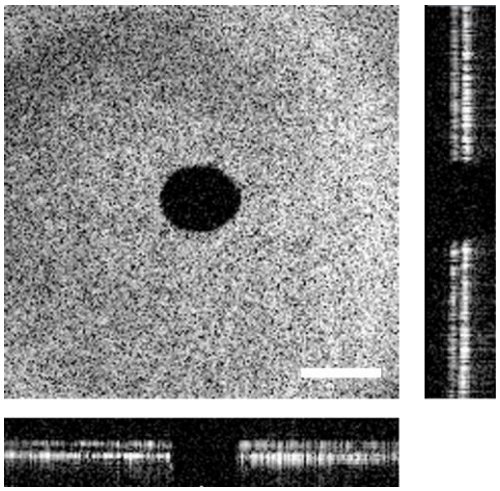

Figure 3.6. *En face* OCT image and cross sections of the pinhole overlaid with a/LCI beam. The scale bar represents 1 mm. Figure taken from [61].

3.4 System Calibration

Previously, the 2D a/LCI system had been calibrated with a scattering phantom containing polystyrene microspheres embedded in polydimethylsiloxane (PDMS) [57]. A phantom with known polystyrene microsphere size typically ranging from 6 to 20 μm was fabricated, and the measured scattering field was matched to the simulated Mie scattering pattern with the same optical parameters. In order to correct any aberration or system misalignment, the measured 2D scattering field is graphically overlaid on top of the simulated scattering data. Discrepancies between the measured angular data and simulated field were minimized by translating, scaling, rotating and shearing the measured data to precisely match the expected distribution. The chi squared value was used to evaluate the goodness of the fit of the measured field and the simulated Mie pattern during the calibration step. However, this process of resizing the measured 2D scattering field to match the simulated data is time consuming, and the scattering phantom composed of polystyrene microspheres in PDMS sample cannot capture long range correlations arising from regular array of scattering features. In order to study long range correlations due to coherent light scattering with a/LCI, simulated cell arrays were fabricated using a micro patterned comb polymer with PDMS. Many other techniques to create scattering standard that mimic tissue scattering properties have been validated using Intralipid [63], Indian ink [64], polystyrene microspheres [65], or some combination of these elements. However, many of these techniques produce liquid

phantoms, which can require long time averaging measurements to reduce the effect of speckle. Recently, there has been much interest to create scattering phantom that have a static matrix with less fluence such as microspheres embedded in polymeric material [66] and Intralipid in gelatin-gel [67]. However, these techniques still do not provide the ability to simulate long range correlation with complex sample structure such as those that are present in epithelial architecture. Therefore, we developed a solid based scattering phantom that can provide complex long range order structure. In this section, the fabrication process and validation of the new phantom are discussed as well as the system calibration with the fabricated phantom.

3.4.1 Correlation Calibration Phantom Fabrication

Several different structures including phantoms with well-defined regular geometry and with irregular arrangements mimicking the cell arrangement in epithelial tissue were fabricated [56]. These scattering phantoms were fabricated using soft lithography technique with PDMS [56] . The scattering phantom was first designed using Computer Aided Design (CAD) using AutoCAD. A chrome glass photomask was custom ordered to enable the designed pattern to be replicated on the master mask. In order to construct the master mask, a 4 inch silicon wafer was spin coated with SU-8 negative photoresist. Then the wafer was soft baked before exposed to UV light through the chrome glass photomask. The wafer was post exposure baked before the SU-8 development. After post exposure baking, the wafer was washed with SU-8 developer

and rinsed with Isopropyl alcohol (IPA) to produce the desired mold features on the wafer. Prior to the application of the PDMS, the mold was spin coated with monolayer of hexamethyldisilazane (HDMS) which acts as release agent for the PDMS. Vacuum degassed PDMS was poured onto the master mold and the PDMS was cured at 70° C for 2 hours. The resulting structures were then gently peeled off from the mold, and brought into contact with the clean cover glass slides to create the light-scattering phantoms.

The regular patterned scattering phantom have hexagonally-packed circular features with two different spacing between the circular features. The type "A" phantom has the center to center spacing twice of the diameter of the circular feature and the type "B" phantom has the center to center spacing one and half times of the diameter of the circular feature as shown in Figure 3.7. Several phantoms with different circular feature size ranging from 8 μm to 20 μm and corresponding spacing between the features were fabricated using both types of spacing geometry. These scattering phantoms have a high degree of radial and self-symmetry that could aid the a/LCI calibration and long range correlation characterization. Samples with irregular pattern will be discussed in the next section.

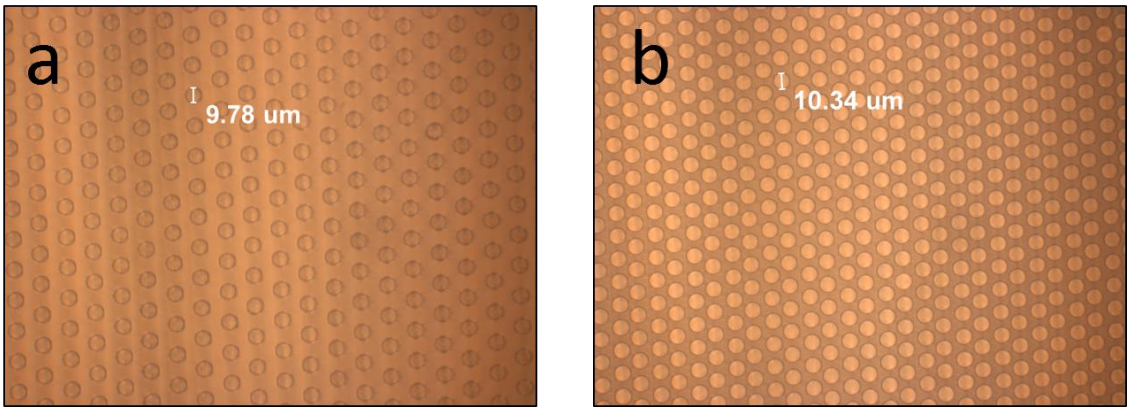

Figure 3.7. Bright field microscope image of the fabricated scattering phantoms. a) Scattering feature have a nominal 10 µm diameter with 20 µm center to center spacing (Type "A"). b) Scattering feature have a nominal 10 µm diameter with 15 µm center to center spacing (Type "B").

3.4.2 Validation of 2D Correlation Measurements

Using the fabricated scattering pattern, the 2D a/LCI system was calibrated via an autocorrelation method. The autocorrelation analysis was implemented using 2D FT analysis and provides accurate information about the spacing and spatial distribution of the individual element within the phantom. The hexagonal packed circular scattering pattern with a 12 µm feature diameter and 24 µm center to center separation between adjacent features (Type "A") was used for initial system calibration. The microscope image of the sample is shown in Figure 3.8a, and the *en face* OCT image of the same sample is shown in Figure 3.8b. Although the OCT system has excellent axial resolution, the system does not have high enough lateral resolution to provide size measurement of the scattering feature. The measured angular scattering profile collected by 2D a/LCI for the phantom is shown in Figure 3.8c. Since a/LCI provides depth resolved information,

only the depth plane corresponding to the phantom feature is presented. The information in the scattering plane is specified by the vertical and horizontal polar angles ($\theta 1$, and $\theta 2$, respectively) which facilitates Fourier analysis. The vertical polar angle ($\theta 1$) corresponds to the galvanometer scanning axis, and therefore has a higher angular range compared to the horizontal axis ($\theta 2$). The range of the horizontal axis is set by the beam spot size at the entrance of the imaging spectrometer slit and the sensor dimension. In order to increase the horizontal polar axis range, a higher demagnification at the collection path is required. However, due to the continuous scanning motion of the galvanometer, the impulse response along the scanning axis ($\theta 2$) is broader than that of stationary axis ($\theta 1$) which accomplishes parallel acquisition using the imaging spectrometer. Additionally, the range of $\theta 2$ is chosen to be symmetric about the origin but the vertical polar angle $\theta 1$ is unidirectional in order to avoid the specular reflection from the sample. The autocorrelation distribution of the phantom can be acquired by simply taking the Fourier transform of the angle dependent scattering measurement (Figure 3.8d). The spatial distribution of the scatterers in the correlation plane not only reveals the spacing between the adjacent features, but also provides directional information of the scattering features. The hexagonal packing of the scattering phantom is clearly captured in the correlation distribution. Additionally, when the correlation distribution is integrated azimuthally across the corresponding radial distance, the center to center spacing between the scattering elements can be easily measured (Figure

3.8e). The light blue ring in Figure 3.8d is translated to the light blue bar region in Figure 3.8e by azimuthal integration, showing the spacing of the closest features. There are additional correlation peaks at higher correlation length, which provide information about the correlation between the scattering features that are located at longer distances.

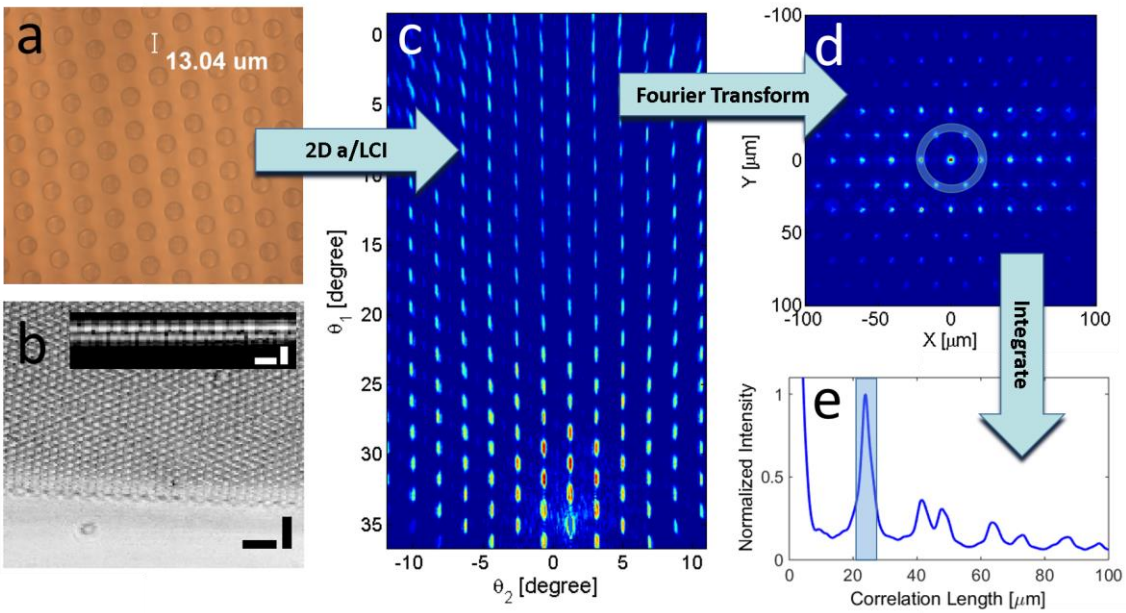

Figure 3.8. Images of scattering calibration phantom constructed via soft lithography in PDMS. The hexagonal packed circular features have a nominal 12 μm diameter with a 24 μm center to center spacing. (a) Bright field microscopy image of the phantom, (b) OCT *en face* image (x-y) with a cross section (x-z) in the inset, (scale bar = 100 μm, inset scale bar = 30 μm), (c) 2D a/LCI measurement (angular plane), (d) Fourier transform of 2D a/LCI measurement (correlation plane), and (e) azimuthal integration of (d) at each radial distance.

As discussed in Section 2.3.3, the Fourier transformation of the angular scattering distribution yields the two-point correlation function of the optical field by the Born approximation [53]. Therefore, the measured angular range of the angular scattering distribution determines the spatial resolution of the correlation function and similarly,

the angular sampling resolution determine the maximum detectable correlation length through the Fourier relationship. With the known nominal size of the features of the scattering phantom, the system can be calibrated by simply taking the Fourier transform of the angular scattering field, and locating the first correlation peak. This calibration process is more accurate and requires less effort than manually resizing the measured scattering distribution to match a simulated scattering field.

With the maximum detectable angular range and the angular sampling resolution of the 2D a/LCI system, the theoretical resolution and range in the correlation domain was determined to be 1.7 μm and 420 μm along the vertical polar angle direction ($\theta 1$), and 2.7 μm and 440 μm along the horizontal polar angle direction ($\theta 2$). However, the system achieves 6 μm and 3 μm FWHM spatial resolution in the correlation plane along the $\theta 1$ direction and $\theta 2$ direction, respectively. The spatial resolution along $\theta 1$ is worse than the horizontal direction due to the galvanometer scanning as mentioned earlier. Also, compared to the stationary axis (sensor parallel detection axis), higher order of aberration including field curvature and spherical aberration is present in the scanning axis due to the galvanometer scanning geometry. Also note that the maximum correlation distance is effectively limited by the size of the illumination beam which is 400 μm. The 2D a/LCI system has a about twice the illumination beam diameter compared to the previous system in order to increase the detectable long range correlation distance.

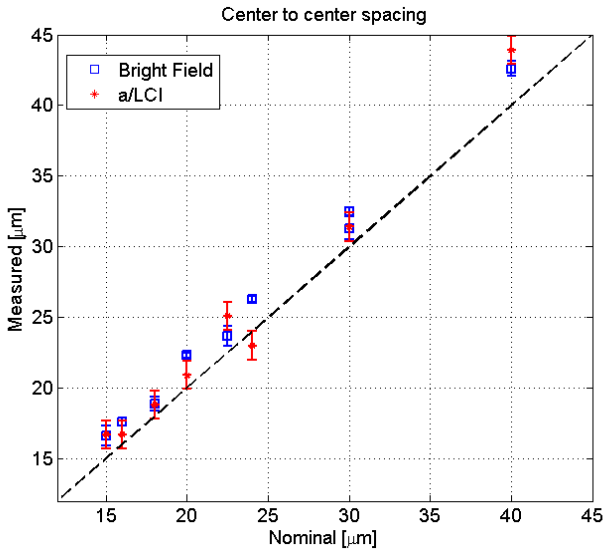

Figure 3.9. Center to center spacing measurement with a/LCI correlation analysis (red) and with bright field microscope image analysis (blue).

Once the 2D a/LCI is calibrated with the standard calibration phantom, the goodness of the calibration and the preciseness of the constructed scattering phantom were investigated using other scattering phantoms with different scattering feature size. The center to center spacing between adjacent features for both type "A" and "B" phantoms have been measured with the calibrated a/LCI system and a bright field microscope. To analyze the microscope images, 20 measurements were made within the image FOV and analyzed using ImageJ. For 2D a/LCI correlation measurement, 3 scans with random sample orientation were captured and the distance from the center of the correlation plane to the closest peak was measured, yielding 18 measurements per sample type. The graph of the center to center spacing measurement using a/LCI and the microscope is plotted in Figure 3.9. The nominal value is set from the theoretical value

requested to create the master photo mask. The center to center spacing measured with a/LCI and the bright field images are in good agreement and the plots showing a linear relationship between the a/LCI and microscope image measurements for the nominal diameter of the phantoms ($r^2 = 0.994$ and $r^2 = 0.996$, respectively). However, the spacing distance measured using 2D a/LCI correlation analysis and microscope image analysis were both slightly larger (approximately 0.85 μm offset) compared to the nominal value. The measured values with the two measurement methods are summarized in the Table 1 below. The percent error is calculated from the difference between the 2D a/LCI correlation measurements and microscope image analysis. The type "B" phantom consistently revealed better agreement between a/LCI and image analysis compared to the type "A" phantom.

Table 3.1. Comparison of center to center spacing measurements using 2D a/LCI correlation analysis and microscope image analysis

	Nominal (Diameter, Spacing)	Microscope (μm, n = 20)	2D a/LCI (μm, n = 18)	Percent error
8A	8 μm, 8 μm	17.6 ± 0.3	16.7 ± 1	5.1%
10A	10 μm, 10 μm	22.3 ± 0.2	20.9 ± 1	6.3%
10B	10 μm, 5 μm	16.6 ± 0.7	16.7 ± 2	0.6%
12A	12 μm, 12 μm	26.3 ± 0.2	23.0 ± 1	12.5%
12B	12 μm, 6 μm	18.9 ± 0.5	18.8 ± 1	0.5%
15A	15 μm, 15 μm	32.5 ± 0.3	31.4 ± 1	3.4%
15B	15 μm, 7.5 μm	23.7 ± 0.7	25.1 ± 1	5.9%
20A	20 μm, 20 μm	42.6 ± 0.5	43.9 ± 2	3.1%
20B	20 μm, 10 μm	31.3 ± 0.8	31.4 ± 1	0.3%

In addition to resolving the spatial distribution of hexagonal packed scatterers, the long range correlation analysis using 2D a/LCI was validated with more complex

structures. Figure 3.10a shows the scattering phantom, created via the same soft lithography process to mimic the intestinal crypts in the intestinal epithelium. The epithelium of the intestine is arranged into a large number of deep invagination called crypt, with finger like projections, villi [68]. The lithographic features have a 20 μm diameter and are arranged in rings that are separated by about 120 μm, in a similar manner to the cellular geometry of intestinal crypts. Using analysis of bright field microscope images, the diameter of the cells was measured to be 18.3 ± 0.3 μm (n=20). The distance between the adjacent crypts was measured to be 120 ± 11.5 μm (n=15) in 3 radial directions and the long distance (second shortest) of the hex packed crypts was measured to be 197.9 ± 15.9 μm (n=5). The 2D autocorrelation analysis of the scattering data in Figure 3.10b reveals clearly identifiable features. The correlation analysis shows a first peak at 20.9 μm which correspond to the size of the cellular feature, and also shows a clear second peak occurring in the 115-120 μm range which corresponds to the spacing of the crypts as shown in the microscope image. The next peak is found in the 200 μm range representing the long distance crypt spacing. We noticed that these features are easier to identify in the 2D correlation plane than the azimuthal integrated plot (Figure 3.10c). In the 1D radial plot, the peak representing the closest adjacent crypt distance is clearly shown, as marked by the light blue box. Other peaks were attenuated by the averaging since the sample structure is anisotropic with the spacing of the ring depending on the direction.

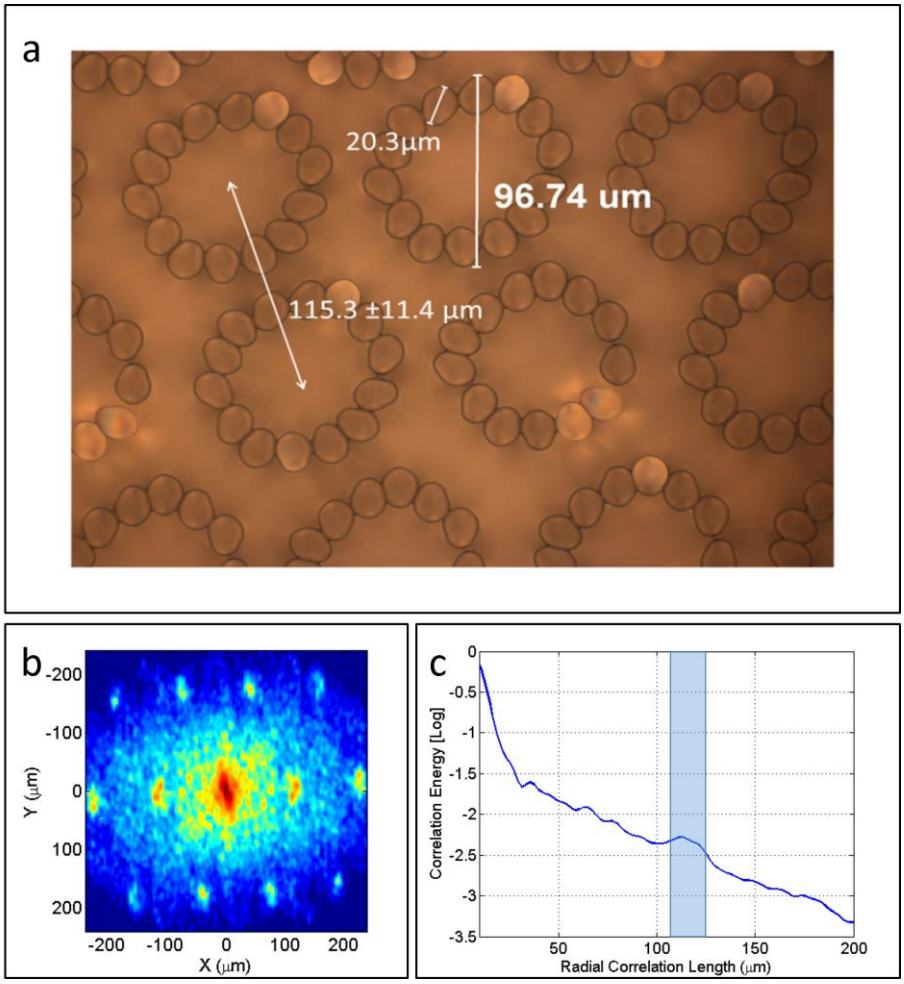

Figure 3.10. a) Bright field microscope image of the crypt resembled phantom. b) Correlation plane of the phantom after Fourier transforming the initial angular scattering distribution measured by 2D a/LCI. c) Azimuthal integration of b) at each radial distance. The light blue box represents 110-120 µm correlation length range.

3.4.3 System Validation with Microsphere Phantom Measurement

After both systems have been calibrated and characterized, the capability of the multimodal system was validated with a conventional scattering phantom composed of spherical polystyrene beads embedded in PDMS. Two polystyrene beads phantoms were fabricated with either 8 or 10 µm diameter beads added to pre-degassed PDMS

which was poured in a chambered coverslip glass. The PDMS sample was cured overnight in a vacuum chamber in order to remove air bubbles from within the sample that will contribute to scattering. Both samples were imaged with OCT (Figure 3.11), and although the OCT can clearly image the beads within the PDMS, the size of the beads cannot be measured accurately due to the limited resolution of the system.

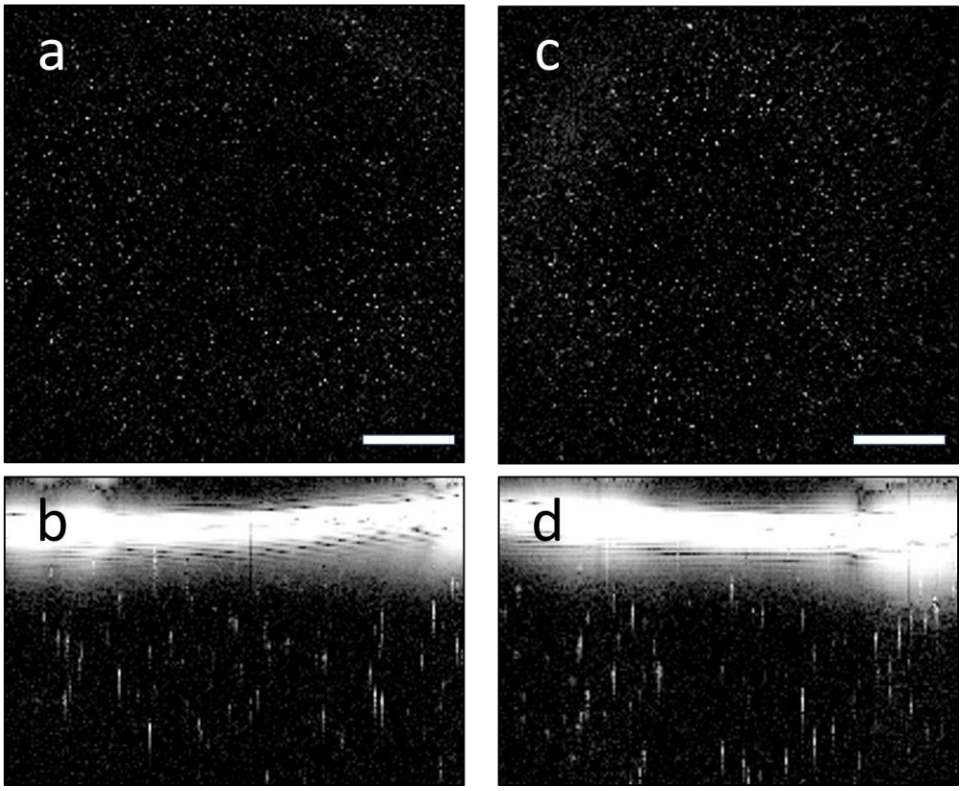

Figure 3.11. a) OCT *en face* image of the 8 µm beads sample with b) a cross section. c) OCT *en face* image of the 10 µm beads sample with d) a cross section.

However, the 2D a/LCI scans of the beads phantom show clear differences in the oscillation frequency in the angular scattering intensity between the two bead phantoms. When the measured a/LCI data was fit to Mie theory by comparing it to the simulated

scattering field shown in Figure 2.4 in section 2.3.2, the exact size of the beads was determined to be 8.00 μm and 10.0 μm demonstrating sub-wavelength accuracy in scatterer diameter prediction.

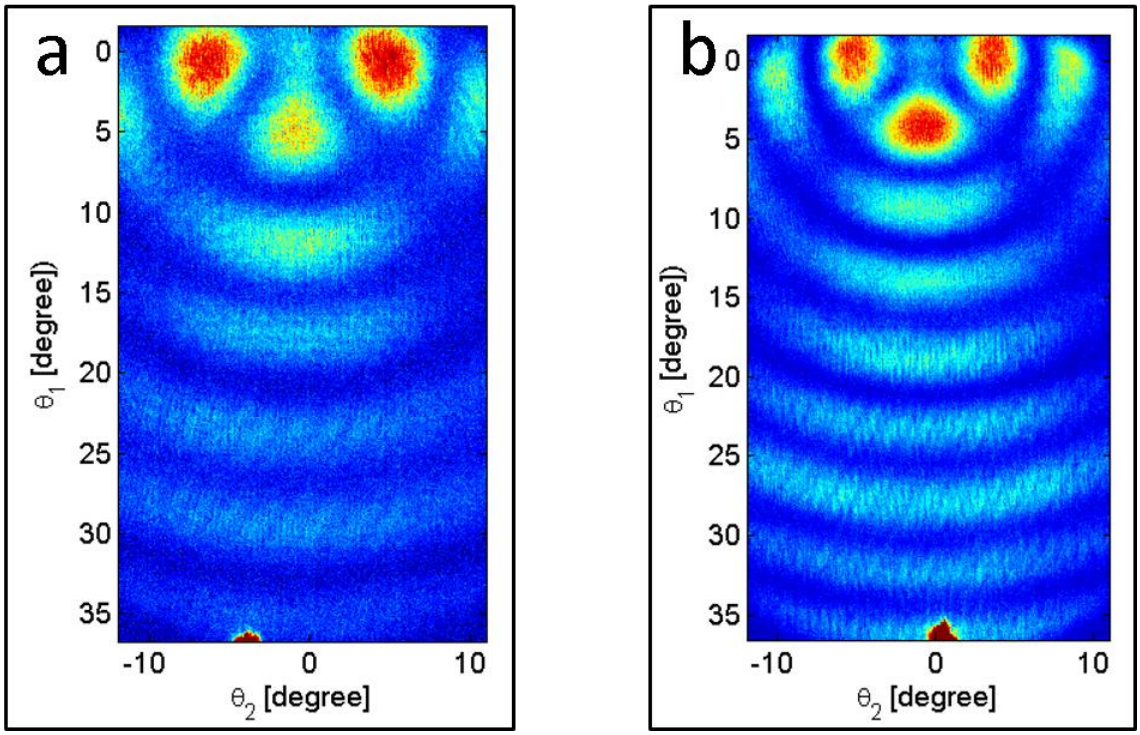

Figure 3.12. 2D a/LCI angular scattering measurement of a) 8 μm and b) 10 μm polystyrene spherical beads embedded in PDMS.

3.5 Summary

We developed a multimodal system that combined 2D a/LCI and OCT in a co-registered FOV to provide a unique analysis of biological sample structure. The OCT system serves as image guidance for the 2D a/LCI depth measurements and the a/LCI provide subwavelength accuracy measurement of sub-cellular features that cannot be measured by OCT due to the limitation in its resolution. With sequential imaging of the

same sample, the combined modality provide a more effective analysis of the depth resolved scattering information that cannot be obtained using a single modality alone. In order to demonstrate the utility of the combined system, a scattering phantom was fabricated via soft lithography. The fabricated scattering phantom not only serves as calibration standard but also shows the capability of the long range correlation analysis using the a/LCI technique. The application of the combined system to *ex vivo* tissue samples will be discussed in the following chapter to show the potential utility of the system for discriminating disease states.

4. Applying the Combined Modality to Develop Quantitative Biomarkers

In this chapter, we apply the combined 2D a/LCI and OCT system to develop quantitative biomarkers to detect early stage disease in animal models. Two types of *ex vivo* tissue were examined with the multimodal system: epithelial tissue from a rat model of esophageal adenocarcinoma and intact mouse eyes from either wild type animals or from a genetically created model of retinal degeneration. All the animal procedures for the animal models were approved by the Duke Institutional Animal Care & Use Committee (IACUC). In the rat model, an esophago-gastroduodenal anastomosis (EGDA) was performed to create chronic reflux of bile salts and stomach acid, mimicking acid reflux which leads to Barrett's Esophagus in humans [19]. For the mice retinal model, rhodopsin knockout causes a progressive retinal degeneration, which makes this mouse a useful model of human disease conditions, such as retinitis pigmentosa [69].

The a/LCI technique can detect micron scale structural characteristics of biological tissue and the technique has been proven in clinical trials to detect dysplasia in Barrett's esophagus patients *in vivo* with 100% sensitivity and 84% specificity [19]. Previously, a/LCI relied on extracting depth-dependent cellular scale information based on the angular scattering field in order to detect changes in cell nuclei in tissue, but the a/LCI technique also has the potential for early detection of degenerative disease using

long range correlation analysis. In addition, the co-registered 2D a/LCI and OCT modalities in the combined system provides unique information to help interpret the structure of a sample based on light scattering data. With the aid of OCT imaging guidance, histological layers of the tissue can be accurately identified and proper sample orientation to the a/LCI beam can be ensured [61]. Since the a/LCI beam has a 400 μm beam diameter, it is crucial for the sample to be oriented such that layered structures are even across the FOV to effectively retrieve and analyze the depth-resolved scattering information for a selected tissue layer. Therefore, OCT images were used to ensure proper sample orientation and to register the 2D a/LCI depth measurements to the histological layers. This chapter presents new quantitative metrics to measure the changes in tissue structure developed using 2D a/LCI and demonstrates the utility of the co-registered 2D a/LCI and OCT modalities in the combined system for imaging biological samples.

4.1 Investigation of Rat Models of Esophageal Adenocarcinoma

4.1.1 Sample / Method

For the rat model, in order to mimic chronic acid reflux which leads to Barrett's Esophagus in humans [19], chronic reflux of bile salts and stomach acid was induced by performing esophago-gastroduodenal anastomosis (EGDA). Sprague Dawley rats of 5-6 weeks of age were purchased from Charles River Laboratories (Wilmington, MA). Rats were randomized to experimental groups after a one-week acclimation period to the

facility. Approximately 16 hours prior to surgery, the rats were fasted overnight. Once the animal was deeply anesthetized, in order to open the abdominal cavity, a 1 inch upper midline incision was made inferior to the sternum. The esophagus, stomach and duodenum were exposed via blunt dissection of fascia followed by retraction with sterile gauze. Two 1.5 cm long incisions were made at the gastroesophageal junction (not reaching the glandular stomach), and on the anti-mesenteric border of the duodenum (approximately 1 cm from the pylorus). A side-to-side duodeno-esophageal anastomosis was performed with accurate mucosal to mucosal opposition. After careful lavage, absorbable sutures were used to close the peritoneal and muscle layers and the dermal layer was closed with Vetbond Tissue Adhesive (3M), followed with 4 to 5 skin staples. After the completion of the surgery, the rat was injected with 5 mL of sterile saline subcutaneously in the skin over the back and anesthesia was turned off. Buprenorphine was utilized to provide pain relief for 72 hours, then the rats became mobile and fully active. Rats were continuously monitored throughout surgery and post-surgery. Throughout the anastomosis procedure, aseptic surgical techniques were used [61].

For 2D a/LCI and OCT imaging, the esophagi of rats in both the control and experimental group (N=20, combined) were removed and the proximal and distal ends of the esophagus were stapled on a thick paper with ruler markings. Both OCT imaging and a/LCI measurements were taken along the esophagus at about 0.5 mm to 1 mm intervals. Unfortunately, the experimental group did not express dysplasia in the

animals examined here, but the experimental data were used to demonstrate the utility of the combined system and to develop a quantitative biomarker that could be used in future animal experiment.

4.1.2 Analysis

In order to show the utility of OCT imaging guidance for ensuring proper sample orientation for a/LCI measurements, two examples of OCT image and depth resolved a/LCI light scattering data from an *ex vivo* tissue sample from the rat model of esophageal carcinogenesis are shown in Figure 4.1: one where the histological layers are flat across the scan and one where tissue folds are present. The sample orientation affects the a/LCI depth resolution such that when the tissue layers are prepared flat respective to the incoming beam, as shown by the OCT image in Figure 4.1a, the corresponding depth-resolved scattering intensity measured by a/LCI at the same ROI reveals sharp transitions between each tissue layer (Figure 4.1b). On the other hand, when the tissue contains undesired folds, as shown in the OCT image in Figure 4.1d, the corresponding a/LCI measurement show blurred tissue layers, making it difficult to register and resolve specific histological layers (Figure 4.1e). This blurring phenomenon is intensified for a/LCI compared to OCT due to the large beam diameter of the a/LCI beam. The a/LCI scan is a function of scattering angle but extends over 400 μm in the lateral direction, a much smaller region than that shown in the OCT image. The a/LCI illumination beam is set to around 400 μm in diameter such that the collected scattering

field emerges from hundreds of scatterers. In addition, the larger beam size is necessary for long range correlation analysis since the size of the illumination beam physically limits the maximum detectable long range correlation that can be observed. The sharpness of the a/LCI scan due to the improper sample orientation is even more noticeable when the scattering distribution depth profile is summed across the collected polar angle as shown in Figures 4.1c and f. The depth measurements in the OCT and a/LCI scans are provided in units of optical path length (OPL) instead of physical distance in air where OPL is defined as physical distance times the refractive index as defined in equation 2.2 in section 2.2.3.

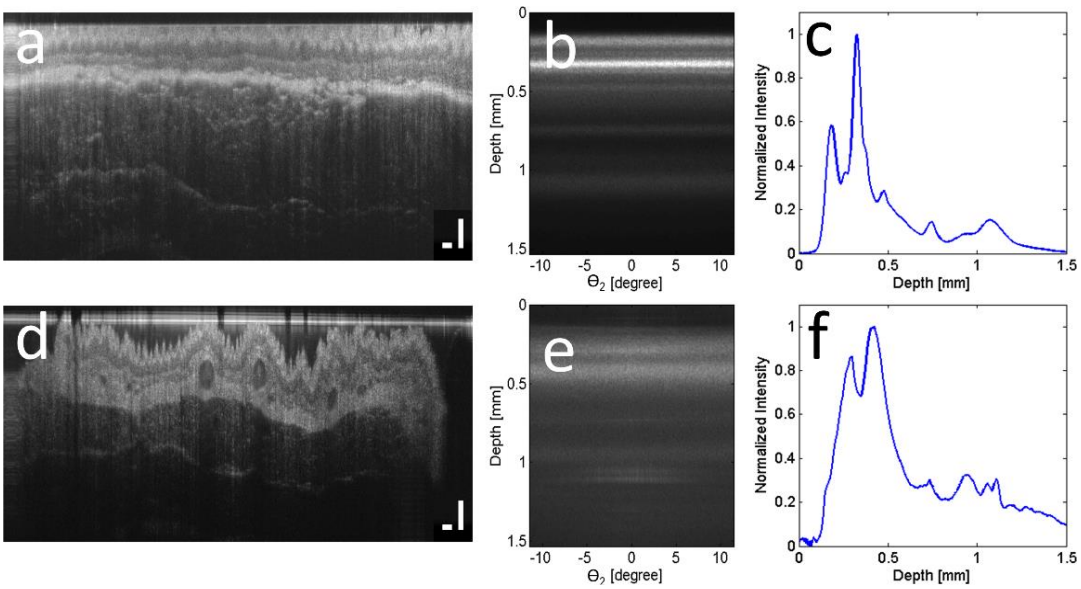

Figure 4.1. OCT and a/LCI scans of EGDA rat esophagus tissue of well-prepared sample and a poorly prepared sample. (a,d) OCT image with the (b,e) corresponding scattering intensity collected via 2D a/LCI presented as depth vs polar angle θ2 and (c,f) the corresponding normalized a/LCI intensity depth profile (A-scan) for a well prepared sample (top) and a poorly prepared sample (bottom). (Scale bars in (a) and (d) = 100μm). Depth measurements are in optical path length. Figure taken from [61].

Although OCT is capable of resolving histological layers due to its high axial resolution, most implementations lack the transverse resolution to provide accurate measurement of sub-cellular features such as nuclear diameter. In addition, the limited spatial dimension of the focused OCT beam restricts long range spatial correlation measurement. However, as discussed in section 3.4.2, both sub-cellular information as well as long range correlations can be extracted from a/LCI measurements. For example, nuclear diameter (sub-cellular feature) and cell to cell spacing (long range spatial correlation) have been accurately measured by Pyhtila et al. using 1D a/LCI measurements of micro patterned cell arrays [70].

The 2D a/LCI measurements provide more information about the tissue sample structure than OCT imaging alone through sample correlation analysis. In order to compare sample correlations across different samples and different depths within a sample, the extracted correlation at each depth is normalized by the corresponding scattering intensity at the same depth. In this way, the correlation measurements are independent of the overall reflectivity of a selected depth or sample. Figure 4.2a shows the total normalized correlation (from 0 to 200 μm correlation) as a function of depth in the esophageal tissue, obtained by Fourier transforming the 2D a/LCI scattering intensity measurement and then integrating across solid angle as shown in Figure 3.8 in section 3.4.2. When the entire range of correlation is binned radially across the 0 to 200 μm range, the resulting correlation vs. depth plot resembles the a/LCI intensity plot

shown in Figure 4.1c. In the correlation plot, certain regions, corresponding to different depths beneath the tissue surface, show increased correlation. By selecting a specific window of correlation range, the correlation energy can be used to highlight the tissue organization such as the presence of cell nuclei. For example, Figure 4.2b shows the correlation energy across the radial lengths from the 10 to 13 μm range which corresponds to the expected size of cell nuclei in this epithelial tissue. The tissue feature marked as ROI in Figure 4.2b shows higher correlation energy at this specific spatial length scale compared to the same depth in the overall correlation function shown in Figure 4.2a. However, examining the correlation energy for a similar sized window of correlation lengths but at larger correlation range (19-22 μm, Figure 4.2c) shows a much lower correlation at the marked ROI.

Many of the correlation peaks in Figure 4.2a-c show consistent magnitudes and shapes in the correlation plots. However, the peak at the 10-13 μm range at the selected depth in Figure 4.2b is consistent with known cell nuclei size and localization at the basal layer of the epithelium in this animal model [17]. In previous a/LCI studies, localization of the basal layer is identified slightly deeper than the brightest intensity in the tissue depth profile. The typical depth in previous studies of rat esophagus was reported to be ranging from 50 to100 μm. However, due to hyperkeratosis, the basal layer have been identified to be laying as deep as 200 μm has been observed [71]. The marked ROI in Figure 4.2 is located at approximately 160 μm deep from the tissue

surface while the highest intensity peak is located at 140 μm deep from the tissue surface. However, the measured depths are given in optical path length difference. Therefore, assuming the index of refraction of mice epithelial tissue to be 1.37, consistent with known values for epithelial tissue [72], the physical depth from the tissue surface is approximately 115 μm for the selected depth, and 102 μm for the basal layer.

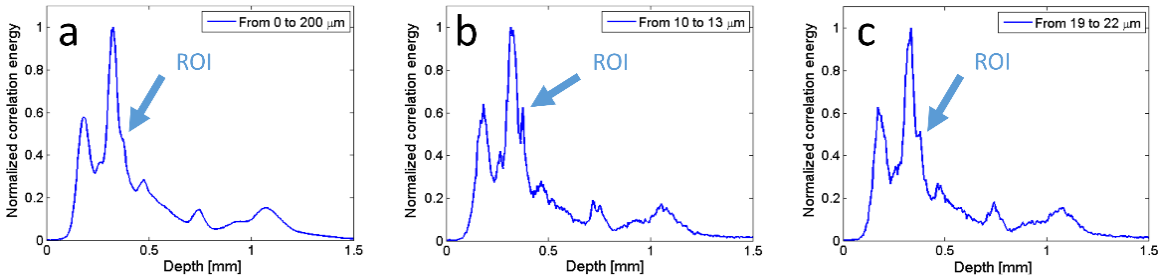

Figure 4.2. Normalized a/LCI correlation energy vs depth for EGDA rat epithelial tissues for (a) 0 to 200 μm correlation length range (b) 10 to 13 μm correlation length range and (c) 19 to 22 μm correlation length range. Depth measurements are in optical path length and arrows mark ROI that show significant correlation changes with different correlation length scale. Figure taken from [61].

In addition to the cell nuclei size measurement, correlation analysis offers further details of the scattering structure. Figures 4.3a shows the 2D angular scattering intensity of the same depth indicated by the ROI in Figure 4.2. Instead of utilizing the 2D scattered data directly to extract sub cellular features through inverse analysis as discussed in section 2.3.2, the data can be converted to the 2D spatial correlation of the selected depth through a Fourier Transform. Although the 2D correlation data also provide directional information about the scattering features, the correlation data can be simplified by radial integration to reveal the notable correlation features in a 1D plot as shown in Figure 4.3c. Note that 1D correlation plot shown in Figure 4.3c differ from the

correlation plots shown in Figure 4.2. The correlation plot in Figure 4.3 is generated for a specific depth, and contains information about a measure of correlation as a function of spatial correlation length scale. On the other hand, the correlation plots in Figure 4.2 are produced at specific correlation length scale representing a measure of correlation as a function of depth. The 1D radial correlation plot from the basal layer in Figure 4.3c shows two distinct peaks at 11.6 μm and 16.7 μm correlation length with a monotonic drops off as correlation length increase. As shown previously, these correlation lengths are roughly consistent with the cell nucleus size and cell to cell spacing [53]. However, Fourier based analysis using the correlation function analysis provides limited resolution to discriminate small changes in nuclear size in early cancer stage [19, 61]. The theoretical spatial resolutions are 1.7 μm and 2.7 μm (6 μm and 3 μm experimental) in the θ1 and θ2 directions, respectively, which are defined by maximum collected angular range in the 2D a/LCI scan, as discussed in section 3.4.2. Therefore, although correlation analysis can provide micro structure information at short correlation length (under 20 μm), the correlation analysis offers the additional advantage of analyzing long range spatial information compared to the conventional inverse model fitting approach.

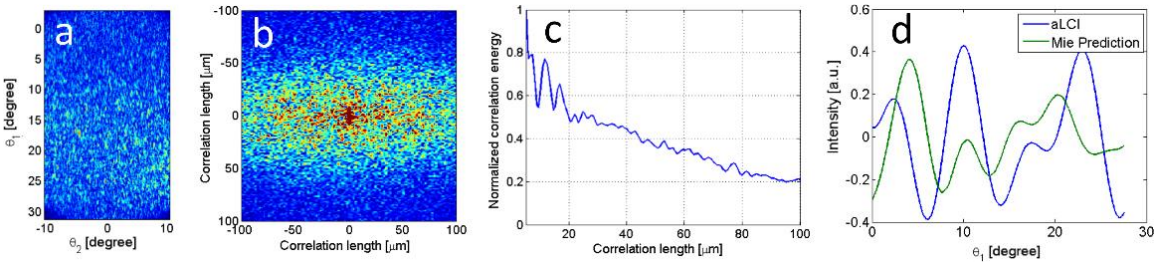

Figure 4.3. a) Scattered intensity collected via 2D a/LCI corresponding to the ROI layer in Figure 4.2. b) Corresponding 2D correlation energy obtained by Fourier transforming a). c) Radial correlation energy vs. correlation length obtained by azimuthal integration of b), and d) Mie fit result at the same plane. The size of the scatterers at the ROI was determined to be 9.7 μm in diameter, with index of the refraction of nuclei to be 1.43 and that of surrounding to be 1.37. Figure taken from [61].

To reveal the structure of the cell nuclei at the selected ROI more precisely, the 2D angular scattering measurements were analyzed using a theoretical model such as Mie theory [18] or T-matrix based analysis as discussed in section 2.3.2 [58]. While T-matrix based analysis utilizes the entire collected 2D scattering field to determine accurate size, shape, and orientation of scatterers by modeling the scatterers as spheroids instead of spheres as in Mie theory, it requires significant computation time. Instead, simple Mie theory simulations can be performed by extracting a 1D scattering profile from the 2D angular scattering map as shown in Figure 4.3d. A single 1D scattering profile ranging from θ1 = 0° to 30° at θ2 = 0° was selected from the 2D a/LCI angular measurement for the Mie fitting. The diameter of the scatterers is determined finding the profile in a library of simulated scattering solutions that has the minimal difference to the low pass filtered experimental data. For the Mie theory based fitting at the selected ROI, the scatterer diameter was determined to be 9.7 μm, with an index of

the refraction of 1.43 for the nuclei and 1.37 for the cytoplasm. This result is in good agreement with a previous measurement from normal rat esophageal epithelium [17]. However, when the same basal layer from the folded tissue was fitted with Mie theory, the goodness of the fit was much worse than that calculated from the properly oriented tissue sample such that no unique scatterer measurements were obtained. Failing of the uniqueness criteria of the predicted Mie fit at the fold tissue site highlights the importance of the sample preparation for a/LCI to produce effective and accurate measurement, and also emphasizes the effectiveness of OCT imaging guidance as an aid for a/LCI to acquire such measurement. In order to investigate the long range correlation (larger than 20 μm) properties of the scattering sample, the monotonically decreasing correlation trend was further examined. Instead of segmenting the data into multiple correlation lengths to analyze the long correlation characteristics, a simple quantitative metric that covers a larger range of correlation lengths was pursed. A number of metrics were considered including the ratio of two correlation energies from two specific depths, and the correlation distance at which a certain fraction of the total correlation is distributed. However, the most effective metric to convey the long range correlation information and describe the monotonic decrease in correlation energy was finding the slope of the correlation plot in a log-log scale. The linear slope in a log-log scale represents a power law relationship: $I = A\ c^{-\alpha}$ where I is the intensity, A is the scaling variable and α is the power law exponent. This power law approach has been used

previously to formulate a fractal dimension measurement of rat esophageal tissues [17, 70]. While the fractal dimension and the power law exponent can be simply related, the results are presented as a simple fitted parameter, the absolute value of the power law exponent (α). The data over the 20-90 μm range and 100-200 μm of correlation lengths in Figure 4.3c were fitted by the two variables in the power-law relationship as shown in Figure 4.4. The correlation at the selected depth was first normalized by the correlation energy at 0 μm correlation length (DC value) so that the calculated power-law exponent is independent of the sample reflectivity. Then the data were fitted using a least squared regression model, and the absolute values of the power law exponent were calculated to be 0.57 and 1.33 for the 20-90 μm correlation range and 100-200 μm range, respectively. A number of correlation length ranges were considered to fit the slope in log-log plot, however, 20-90 μm and 100-200 μm range consistently resulted in higher R-squared value above 0.95 across various samples. In addition, the 100-200 μm range correlation data produced a similar power-law exponent across different samples and depth compared to 20-90 μm range. This is likely due to the finite size of the a/LCI illumination beam (~400 μm) which reduce the correlation values at longer ranges. Therefore 20-90 μm correlation range was used to compare long range correlation of various samples.

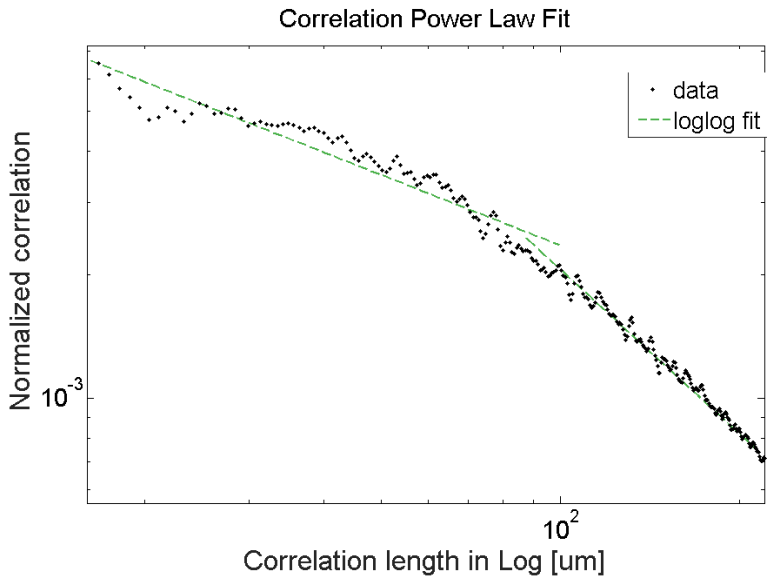

Figure 4.4. Radial correlation energy vs correlation length at the marked ROI in Figure 4.2 in log-log scale. The data over the 20-90 μm range, and 100-200 μm of correlation lengths were fitted using least squared method.

To determine the validity and consistency of the power-law fitting technique as a metric to discriminate abnormalities across different sample types, additional technical samples were imaged and the long range correlations were analyzed at different imaging condition. First, a solution containing 0.225% 260 nm diameter polystyrene beads (Duke Scientific Corporation) was imaged at multiple depth to investigate the power-law exponent calculation variability depending on the depth of the sample and its relative positon to the focal plane. The sample was moved first placed at the focal plane and translated of focus by increment of 200 μm. Figure 4.5 shows the normalized a/LCI intensity for the beads solution at multiple depths and the corresponding power-law exponent calculation over the entire depth. As can be seen, the power law exponent

calculation yields similar values regardless of the sample position except for the air to sample interface where there is a large change in the index of refraction.

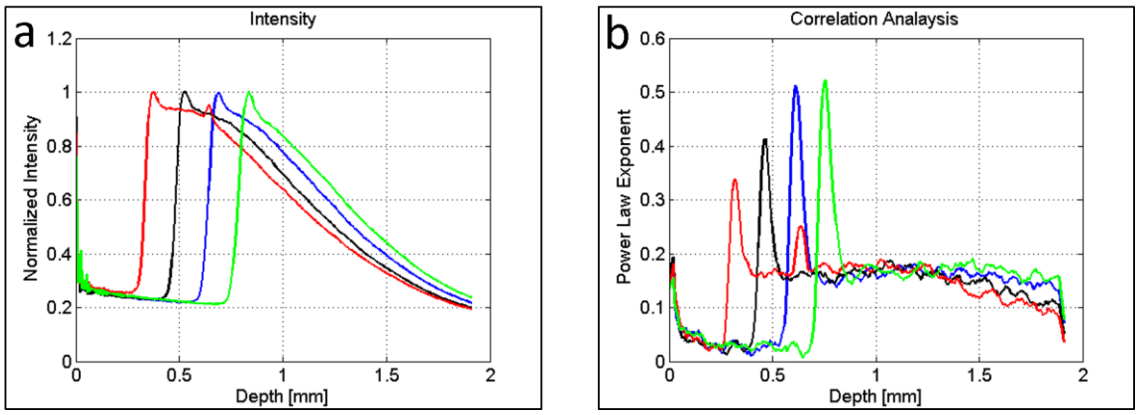

Figure 4.5. a) Normalized a/LCI intensity for the 0.225% 260 nm polystyrene beads solution imaged at multiple depths. b) Amplitude of fitted power law exponent over 20-90 µm correlation length across entire imaging depth for each sample. Depths are reported in optical path length.

The effect of averaging multiple scans on the power-law exponent calculation was also studied with the same beads solution. The 2D a/LCI scattering field of the beads solution was collected for 10 acquisitions and fitted for different averaging schemes, including a single scan, five incoherent averages, ten incoherent averages, and five coherent averages, as shown in Figure 4.6. Coherent averaging is performed prior to taking the absolute value after Fourier transform such that phase information is conserved while incoherent averaging is performed after taking the absolute value such that phase information is not conserved. Typically, an incoherent average using five 2D a/LCI measurements was performed to improve the SNR for Mie fitting and T-matrix fitting. The normalized a/LCI intensity across all the scans reveals the same trend when

averaged except for coherent averaging which shows some oscillation in intensity at depths above the sample surface where the signal is low. This is expected due to the lack of a real signal when coherent averaging is executed in the area where scattering is not present. However, there is a significant difference in the fitted power-law exponent across the samples with different averaging schemes. The power-law exponent from coherent averaging remains close to that from a single scan except at the air/sample interface. However, the incoherent averaging showed an increase in the exponent throughout the entire imaging depth as function of number of averages. Therefore, for the long range correlation analysis using the power-law exponent, the a/LCI scans were incoherently averaged for consistency.

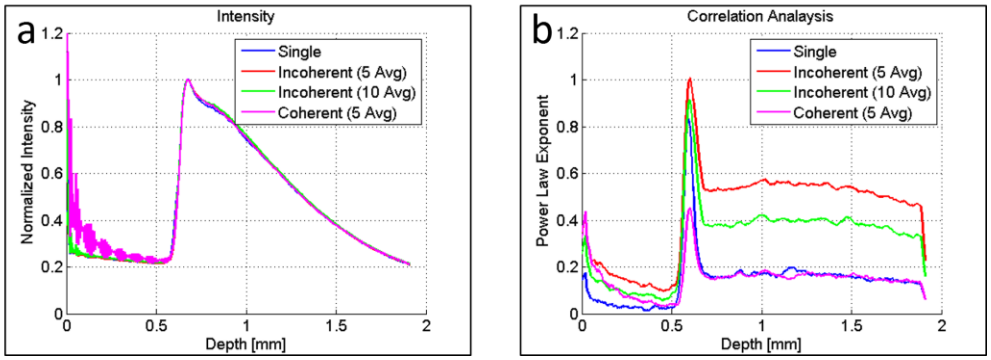

Figure 4.6. a) Normalized a/LCI intensity for the 0.225% 260 nm polystyrene beads solution with different number and types of averaging scheme. b) Amplitude of fitted power law exponent over 20-90 μm correlation length across entire imaging depth for each sample. Depths are reported in optical path length.

Next, the contribution of different exposure times was investigated. Typically, exposure time is set to a specific value (usually 400 μs) with the 2D a/LCI system for consistency when imaging a set of samples. However, due to small fluctuations of the

Ti:Sapphire laser power and coupling efficiency, exposure time is often altered to make sure the reference field close to 80% of the camera well depth. A white card stock (thick paper) was imaged with different exposure time from 0.4 ms to 0.7 ms at 0.1 ms step size (Figure 4.7). Unlike the polystyrene beads solution which showed a constant power law exponent across all depths except a sudden increase at the air/water interface, the magnitude of the power-law exponent from the white card stock showed monotonic decrease. The change in exposure time did not impact either the normalized a/LCI intensity or the power-law exponent aside from a subtle increase in the exponent at depths where no sample was present.

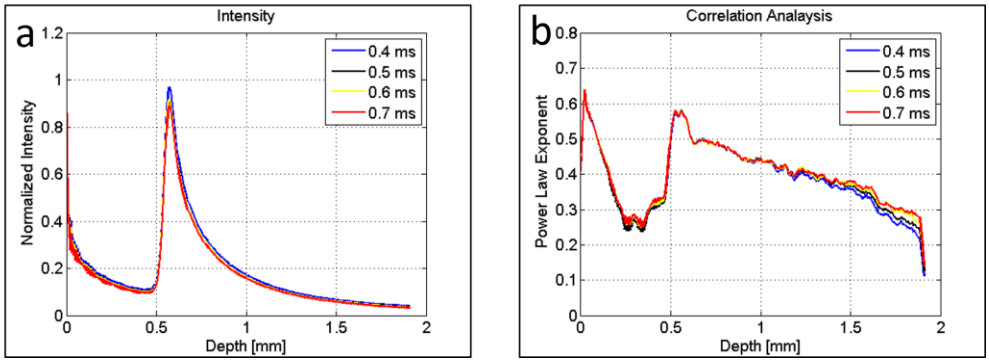

Figure 4.7. a) Normalized a/LCI intensity for the white card stock for different exposure time. b) Amplitude of fitted power law exponent over 20-90 μm correlation length across entire imaging depth for each sample. Depths are reported in optical path length.

Finally, the power-law fitting technique was compared across different types of samples. Figure 4.8a shows the normalized a/LCI intensity as a function of depth for three samples: a solution containing 0.225% 260 nm diameter polystyrene beads, the rat esophageal tissue, and white card stock. All of the three samples were aligned such that

air/sample interface appears at a depth of 0.4 mm in the a/LCI measurement. The radial correlation energy for all three samples is shown on a log-log scale in Figure 4.8b, alongside an equivalent measurement where no sample was present as an indication of system noise. The correlation energy measurement for the tissue was obtained from the same depth as the ROI indicated in Figure 4.2a-c and the same depth from the surface was chosen for the other samples. Several differences in the correlation for each sample were noted including a more rapid fall off in the correlation measured from white card stock and esophageal tissue at long correlation lengths compared to that from the polystyrene beads solution. The blue box in Figure 4.8b indicates the correlation range (20-90 μm) used for regression analysis for determining the power-law exponent. The magnitude of the fitted power-law exponent for each sample over depth is plotted in Figure 4.8c. For each sample, depth ranges of 30 μm intervals were binned for correlation analysis. The noise plot shows low and uniform correlation across all depths as expected, while the polystyrene bead solution has a constant power law exponent across all depths except a sudden increase at the air/water interface as shown earlier. The magnitude of the power law exponents measured for the white paper and esophageal tissue also show a decreasing trend over depth, but much higher values than that of beads. This trend indicates that the correlation falls off more quickly for these two samples compared to the correlation of the bead sample. Finally, the fitted power law

exponent for the white card stock decreases monotonically over the imaging depth, in contrast to the esophageal tissue which shows overlying structure at certain depths.

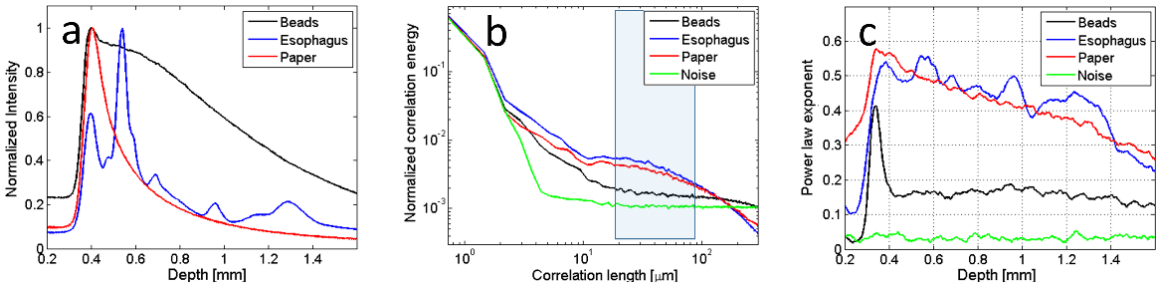

Figure 4.8. a) Normalized a/LCI intensity for the 0.225% 260 nm polystyrene beads solution, the esophageal tissue, and white paper, and b) radial correlation energy vs correlation length by azimuthal integration of 2D a/LCI correlation plane at the same depth for each sample in log-log scale. The blue box indicates the region where data were analyzed using the power-law fitting. c) Amplitude of fitted power law exponent across entire imaging depth for each sample. Depths in a) and c) are in optical path length. Figure taken from [61].

4.1.3 Discussion

When imaging rat esophageal tissue, the OCT image was utilized to confirm flat tissue orientation with regard to the illumination beam allowing each layer in the a/LCI image to be co-registered with the histological layers observed in the OCT image. The OCT image not only provided real-time image guidance to locate specific ROIs, the OCT image enhanced the effectiveness of the a/LCI measurement by rejecting improper sample orientation before a/LCI scanning and processing. When 2D a/LCI measurements were taken on the folded sample, the histological layers were blurred and failed to determine the nucleus size with Mie fitting. Thus, by using OCT imaging for real-time imaging guidance, a/LCI measurements can be targeted to ROIs which are more likely to yield convergent Mie fits. As described in section 2.3.2, in order to ensure

the uniqueness of the Mie fitting, the chi-squared value of the best fit is compared to that of the fit obtained with the null solution. If the two solutions converge, the fit is deemed a non-unique solution and discarded. After comparison to the null solution, the chi-squared value of the best fit is compared that of the next best fit. The best fit chi-squared value must be smaller than the second best fit value by more than 10%. Otherwise, the fit is treated to be a non-unique solution and rejected [18]. Both the properly oriented and folded samples passed the first test criterion in the comparison with the fit obtained with null solution, indicating that there was useful information in the fit. However, the chi-squared fit for the folded sample failed to pass the second criterion and was thus discarded as a non-unique solution.

Analyzing the correlations across varying spatial length scales at each depth can reveal structural features of the sample that are not detected in conventional OCT images. Figure 4.2a-c shows that certain tissue layers have higher correlations at specific length scales. The azimuthally averaged radial correlation function in Figure 4.3c shows a trend of decreasing correlation energy with increasing length scale and two distinct peaks are observed. The peak in the correlation provides a size that matches between the Mie theory and Fourier analysis and both results were in good agreement with previous studies with this animal model [17, 70].

In the study, other technical samples including beads solution and white paper were used to validate the optimal correlation range for fitting the power law exponent.

Different imaging conditions such as varying exposure time, and averaging methods were tested to formulate a quantitative biomarker that can be used across different types of samples. The use of a power law function to fit the angular scattering data was introduced with the original a/LCI technique [53] and then used for analysis of rat esophageal tissue data [17]. The inverse power law behavior relates to a fractal dimension (FD) which is a measure of the self-similar nature of the tissue [73]. The power law exponent, α, can be simply related to the fractal dimension by $D = 3 - \alpha$ [53]. In a previous study of squamous cell carcinoma in the rat esophagus, the calculated FD ranged from 2.06 to 2.42 using a 2 to 20 μm correlation range compared to 2.44 to 2.72 in this study using 20 to 90 μm correlation range. This range of values agrees with those shown by Yi et al., who measured fractal dimension in biological tissue to be between 2 and 3 by recovering the refractive index correlation function using inverse spectroscopic OCT (ISOCT). In this analysis, the tissue is treated as a continuous medium with refractive index fluctuations [74], instead of modeling the scattering in tissue as a collection of spheres within the medium as is done in Mie theory. As discussed in section 2.1, light scattering in tissue can be modeled as a continuous random medium [40] or can be described as discrete particles using an inverse scattering model [75]. Similarly, the power law fitting method shown here does not treat the tissue scattering as discrete scatterers but rather analyzes the medium as continuous. Although the rat model did not express the anticipated dysplasia, the model was analyzed thoroughly

and a quantitative metric was developed which was utilized in a subsequent animal model study.

4.2 Early Detection of Retinal Degeneration in a Mouse Model

4.2.1 Preliminary Experiments

A pilot study was performed with 2D a/LCI on 2 wild types (WT) and 2 rhodopsin knockout (RhoKO) mice at 8 weeks of age. As described in section 2.3.1, this iteration of 2D a/LCI system did not have co-registered OCT imaging, and had a bottom illumination sample geometry. Therefore, the retina from each animal was extracted and flattened on a chambered coverslip glass for examination. The sclera was detached from the retina to create flatter contact. 2D a/LCI scans were taken at multiple random points of the sample, and the acquired scans were averaged. In order to compare the a/LCI scan with OCT images, the samples were transported to a separate OCT system for imaging. The OCT system was a custom built fiber based OCT (SD-OCT) system with a superluminescent diode (SLD, λ = 830 nm, 50 nm bandwidth; Superlum, Russia) that achieved 6 μm axial resolution and 25 μm lateral resolution on the sample. The OCT images of a WT mice retina and RhoKO mice retina are shown in Figure 4.9.

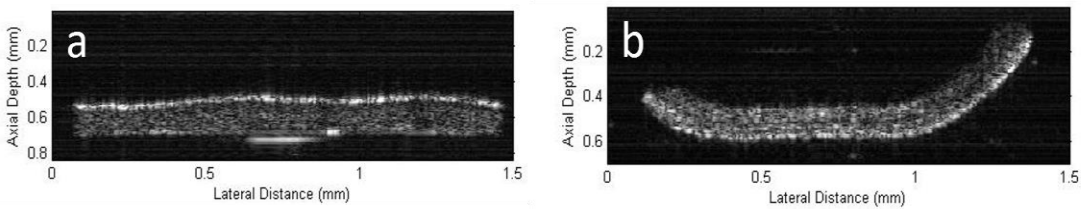

Figure 4.9. a) OCT image of WT mice retina and b) OCT image of RhoKO mice retina taken after 2D a/LCI scan. The axial depth is given in terms of optical path length.

Although the OCT images could not resolve the majority of the mouse retinal layers, we realized that there was a significant amount of tissue bending and non-uniform tissue preparation across the sample. As discussed in section 4.1.2, it is crucial for a/LCI to have flat and well aligned sample layers respective to the illumination beam for successful measurements.

Another set of samples of WT (N=1) and RhoKO (N=2) mice were prepared for a/LCI imaging with the quality of the sample verified using a higher resolution OCT system in the Ophthalmology department. The commercially available high resolution OCT system (Bioptigen Inc. Envisu R2200) has an 840 nm center wavelength with 180 nm bandwidth, achieving a 2 μm axial resolution. The OCT images of the WT and RhoKO mice retina are shown in Figure 4.10. Some tissue folding as well as uneven tissue layers were clearly visible despite careful sample preparation. Therefore, although some interesting correlation features were observed with the a/LCI correlation analysis, the repeatability and consistency of sample preparation was still not met. Instead of making sequential a/LCI measurement and OCT imaging on separate instruments for

side by side comparison, a multimodal system was pursued for real time a/LCI imaging guidance with OCT as described in detail in section 3.3.

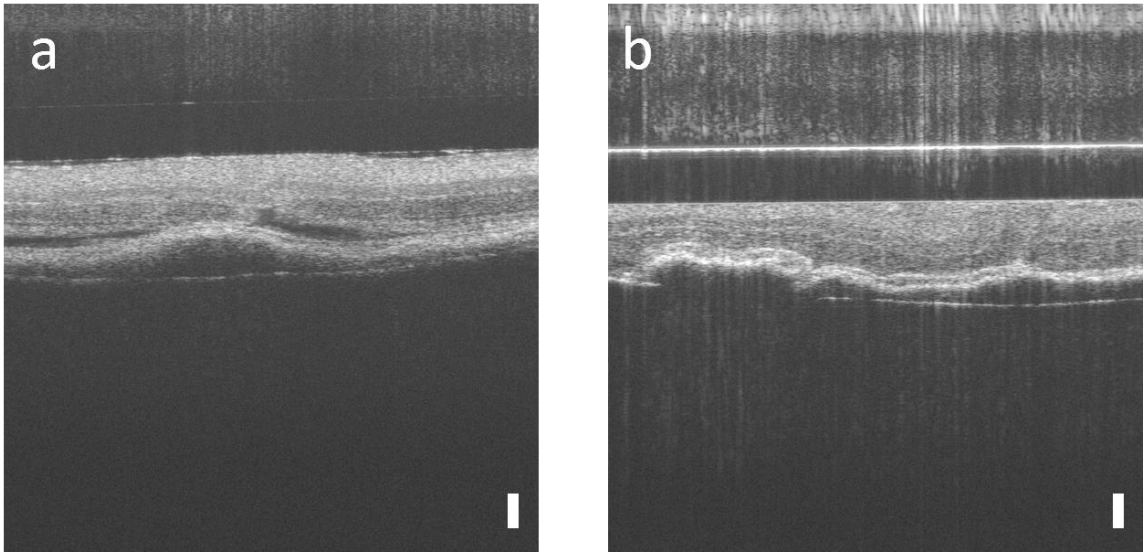

Figure 4.10. a) OCT image of WT mice retina and b) OCT image of RhoKO mice retina taken with a high resolution OCT system. The scale bar indicates 100 µm axial imaging depth in optical path length.

4.2.2 Methods for Imaging Retina in Intact Eyes

After development and registration of the combined 2D a/LCI and OCT system (section 3.3), one additional modification was made in the multimodal system. A custom designed objective lens was inserted in front of lens L3 as shown in Figure 4.11. This objective and the lens of the eye are in a 4f configuration that images the mouse retina onto the sample plane of the combined system. In addition, the objective lens was designed to correct for aberrations from the lens of the mouse eye. The intact eyeball is placed in a sample chamber with a 5 mm diameter hemisphere to match the eye curvature and to maintain alignment of the eyeball relative to the objective lens during

image acquisition and translation to different ROIs. The sample chamber is then placed on an adjustable x, y and z translational stage. The front lens surface of the intact eyeball makes a contact with the objective lens as shown by the dotted lines in Figure 4.11.

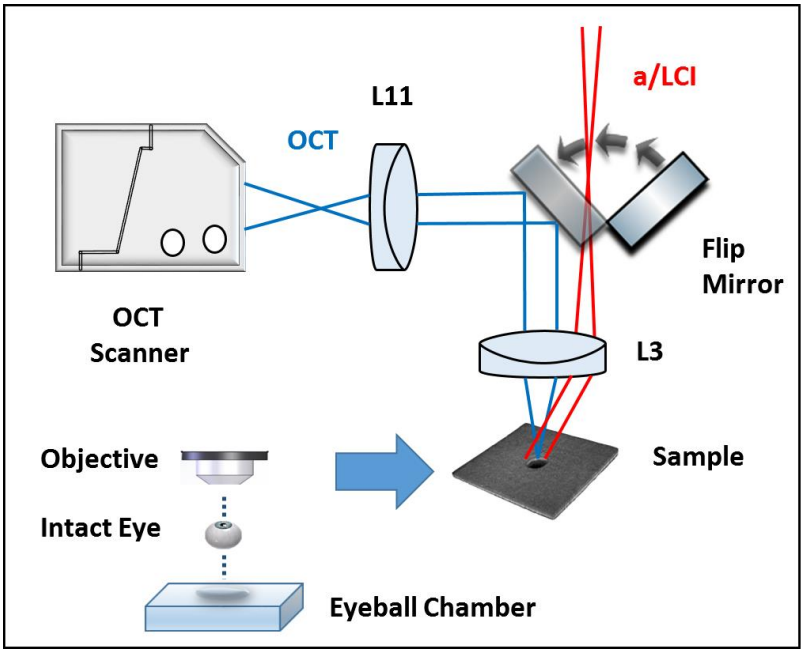

Figure 4.11. System geometry near the sample plane showing sequential imaging with 2D a/LCI and OCT. For mouse retinal imaging, a custom designed objective was inserted in front of L3 to create a 4f configuration with the crystalline lens of the eye. The front surface of the intact mouse eyeball is placed in contact with the objective, and the back surface is held by the sample chamber which matches its curvature as shown by the dotted line. Figure taken from [61].

Imaging of the mouse retina was performed using intact eyeballs from WT and RhoKO mice of different ages (4, 8, and 12 weeks old). The eyes were dilated with a solution containing 1% cyclopentolate and 2.5% phenylephrine for 6 minutes. Mice were then euthanized with CO2 asphyxiation, followed by decapitation. The superior part of each eye was marked, and the eyes were removed from the skull and stored in cold

mouse Ringer's solution consisting of 130 mM sodium chloride, 2.5 mM potassium chloride, 1 mM magnesium chloride, 28 mM glucose, 10 mM HEPES and 2 mM calcium chloride (pH 7.4). The eyes were cleaned of connective tissue and muscle, the optic nerve was severed, and the eyes were placed into a greased divot in the custom-designed tissue chamber described above. The eyes were positioned so that the superior-inferior quadrants were oriented top-bottom and the ONH was oriented in the center of the dilated pupil. The eye was immersed in the Ringer's solution during imaging.

OCT imaging is first utilized prior to acquiring the 2D a/LCI measurements to align the optic nerve head (ONH) at the center of the OCT FOV which has already been aligned to the a/LCI beam as described in section 3.3. The centered ONH is marked by an arrow in Figure 4.12 and serves as the reference point that designates the locations of the ROIs imaged with the multimodal system.

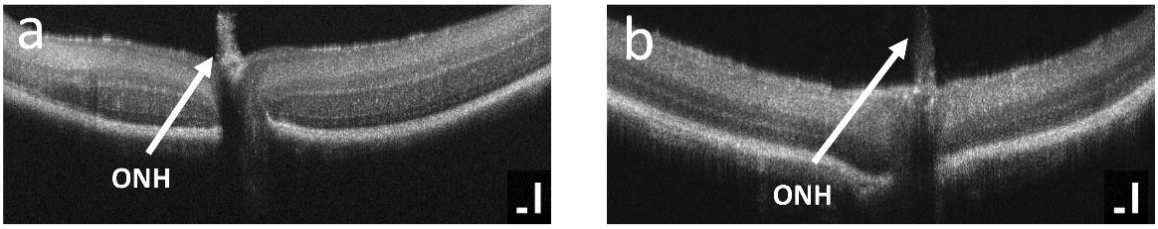

Figure 4.12. OCT imaging of retinas for (a) WT, and (b) RhoKO mice. The location of the ONH is indicated with the white arrow, and functions as the reference point to designate the locations of the ROIs. The scale bar indicates 100 μm. Figure taken from [61].

Once, the ONH of the mouse retina was centered in the middle of OCT FOV, the 2D a/LCI measurements of mouse retina were collected at 8 locations ranging radially from 500 μm to 1.5 mm from the ONH. During repositioning of the sample, OCT

imaging was utilized to ensure a flat sample and monitor for any abnormalities within the sample while adjusting the translational stage and objective lens. For repositioning, the stage was first translated, and then the custom objective lens was repositioned to have flat retinal layers respective to the incoming beam determined by real time OCT imaging. An example of an OCT *en face* image showing the repositioning of the mouse retina along the vertical direction with the translational stage in Figure 4.13 demonstrates the stability of the sample during sample relocation.

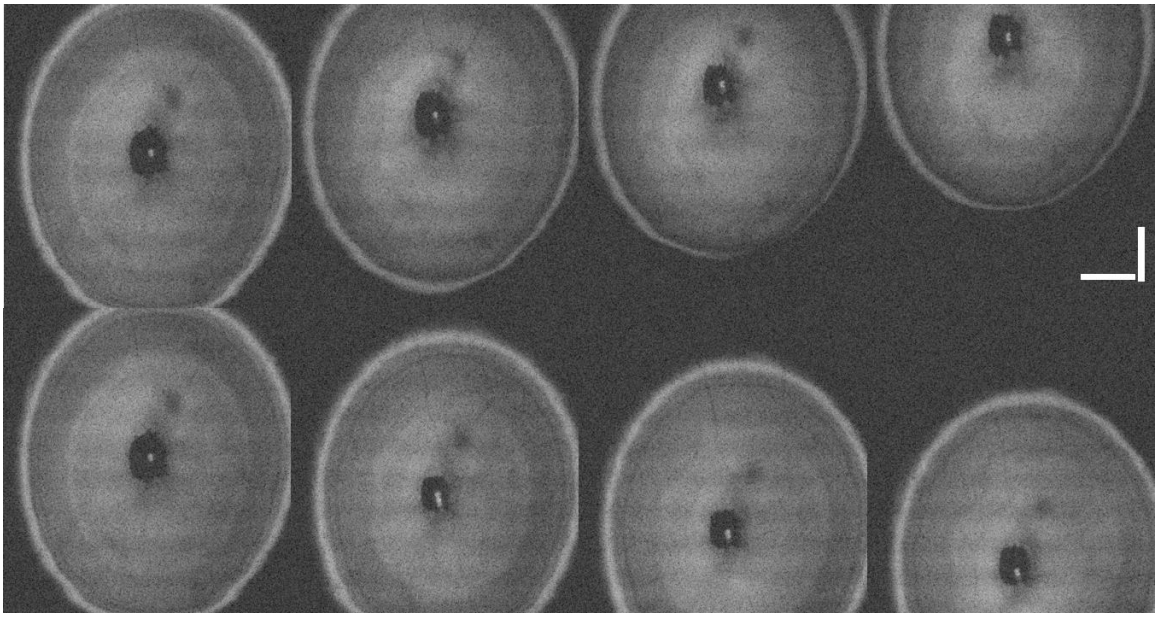

Figure 4.13. *En face* OCT images of mice retina during repositioning the eye along the vertical direction. The scale bar indicates 1 mm.

With an intact mice eyeball, the most time consuming step was the initial positioning of the eye. Often an air bubble would get stuck in between the front surface of the mouse lens and the custom objective. In such an event, the eyeball was moved away from the objective lens and the air bubble was wiped away with a cotton swab.

However, repetitive action of contact and separation of the eyeball from the objective lens surface would result in rotation of the eyeball in the chamber. Thus, high vacuum grease was utilized (Dow Corning) to adhere the eyeball to the chamber. Due to the long length of time required for initial positioning of the eye, degradation of retinal tissue was noticeable as acquisition lengthened. An OCT image of a fresh WT mouse retina and that of the same sample after an hour of experimental imaging are shown in Figure 4.14, with noticeable degradation of the retinal layers in Figure 4.14b. In order to speed up the positioning and acquisition process, at the start of each experiment extra WT mice were sacrificed first before taking any measurements. These extra eyeballs were used to optimize the alignment of the system, and about 15 minutes was required per eye to acquire both OCT and a/LCI measurement at the designated 8 locations. After scanning with the both modalities, the eye was fixed in formalin for subsequent histological analysis.

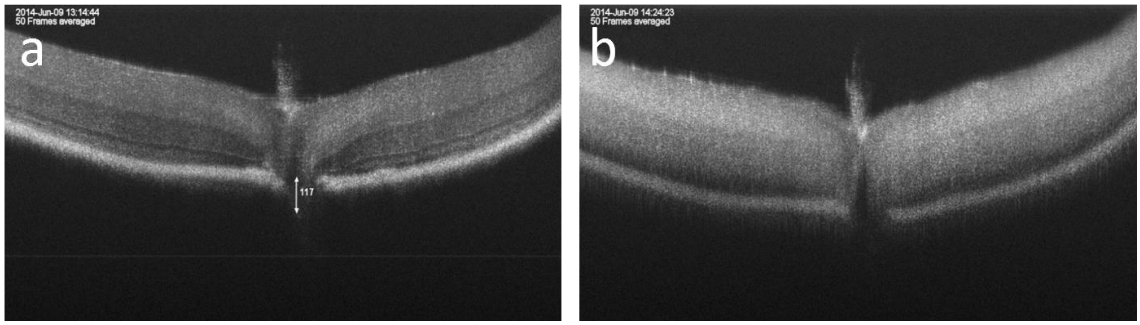

Figure 4.14. OCT image of a) a fresh WT retina, and b) the same sample after an hour of experiment showing the degradation of the retinal layers over time.

4.2.3 Analysis

For each 2D a/LCI measurement, an OCT image of the same ROI was collected. Representative data from a WT mouse retina, consisting of an OCT image and an a/LCI scan of scattered light intensity as a function of depth and polar angle, are shown in Figure 4.15a and b. In order to enable correlation of the light scattering data with specific histological layers, the OCT scans of both WT mice and RhoKO mice are segmented manually by following the OCT segmentation methodology for murine retinal images given by Srinivasan et al. [76]. For this experiment, the angular scattering information was analyzed for the nerve fiber layer (NFL), outer plexiform layer (OPL), and the layer containing both outer segment photoreceptors and retinal pigmented epithelium (OS/RPE). The three layers have strong scattered light intensity, and histological changes at the OPL layer are expected in this model due to rapid photoreceptor degeneration. The OS/RPE layer is the highest scattering layer below the OPL layer so that light scattering at the layer is not only the strongest among the layers but also will contain information about scattering structure in OPL. A previous study by Wang et al. showed the angular dependence of scattering at the NFL layer in human subjects by separating low and high angle scattering via path-length-multiplexed scattering-angle-diverse OCT (PMOCT) [77]. Thus, the NFL layer may be of interest for diagnosing early retinal disease.

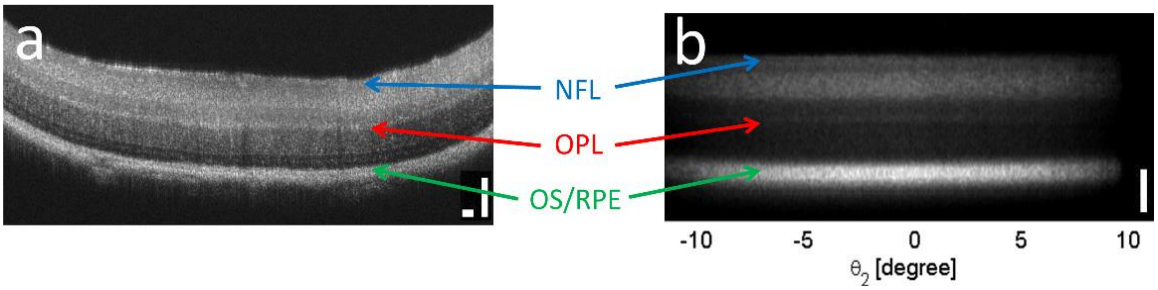

Figure 4.15. a) OCT image of wild type mouse retina (scale bar = 100 μm). b) Scattering intensity collected via 2D a/LCI as function of depth vs polar angle θ2. Arrows indicate corresponding layers. Figure taken from [61].

Typical illustrative data of the 2D a/LCI scattering distribution and the corresponding correlation function for the OS/RPE layer of a WT mouse retina are shown in Figure 4.16a and b, respectively. Note that the collected angular range in the intact mouse eye was smaller compared to that of beads and scattering calibration samples in Figure 3.8 and 3.12 in section 3.4.2 and 3.4.3 respectively due to the physical aperture of the mouse pupil.

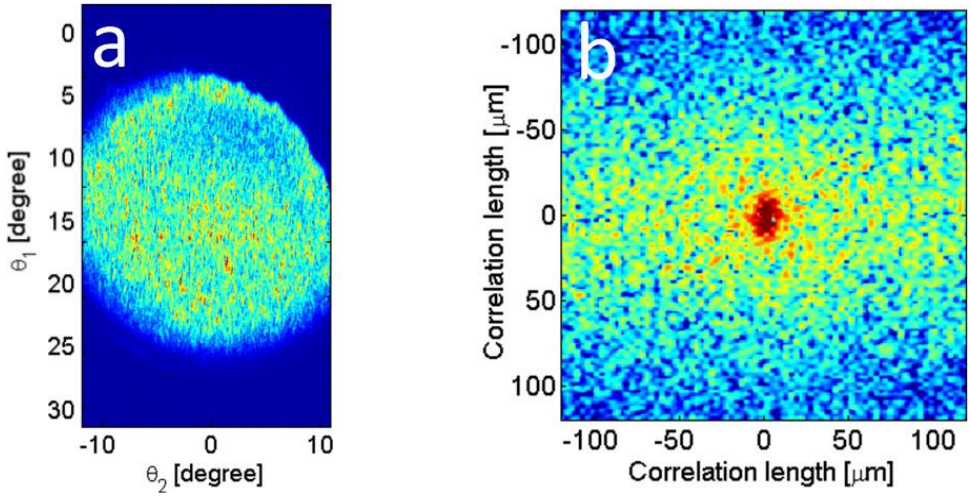

Figure 4.16. a) Angular scattering plane measured with 2D a/LCI from the same sample at the depth corresponding to OS/RPE, and (b) correlation plane of the OS/RPE. Figure taken from [61].

Figure 4.17a shows the azimuthally integrated 2D correlation energy of the scattering data from the OS/RPE layer in Figure 4.16b above. In contrast to the radial correlation energy of the esophageal tissue, which had distinct peaks for correlation length scales less than 20 μm followed by a monotonic decrease in energy, the radial correlation energy of retinal tissue only showed a monotonic decrease in correlation energy throughout without noticeable short correlation peaks. To facilitate power law fit analysis, the correlation data were plotted as normalized radial correlation energy versus correlation length in a log-log scale for the three selected layers: NFL, OPL, and OS/RPE layers in Figure 4.17b.

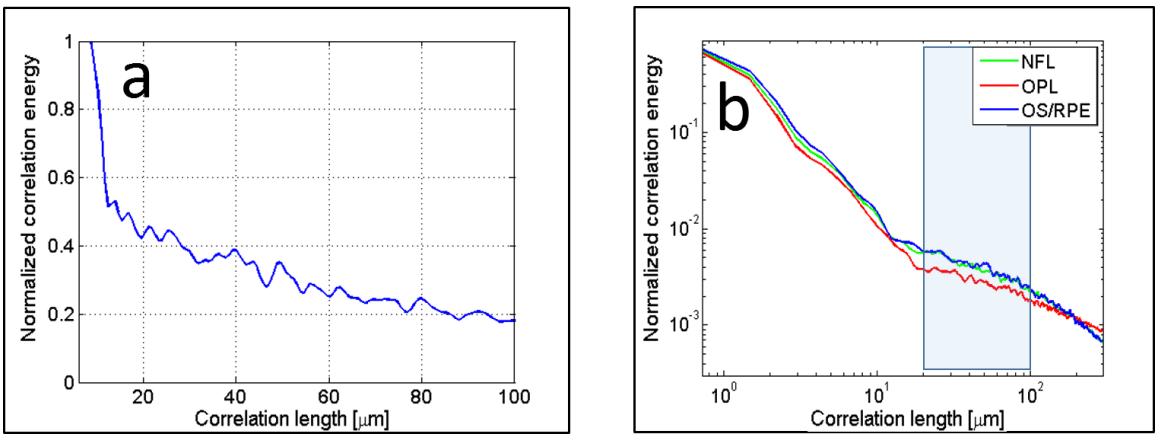

Figure 4.17. a) Normalized radial correlation energy vs. correlation length obtained by azimuthal integration of correlation of OS/RPE layer shown in Figure 4.16b. b) Normalized radial correlation energy vs. correlation length for NFL, OPL, and OS/RPE in log-log scale. Figure taken from [61].

For the long range correlation analysis using the power law relationship, the a/LCI measurements in the three layers were binned into 30 μm depth intervals. The typical depth selected for the NFL layer was 50-70 μm in optical path length from the

tissue surface for both WT mice and RhoKO mice. However, the typical depths selected for the OPL layer and OS/RPE layer varied across the model, especially for different ages of the RhoKO mice. The typical depths selected for the OPL layer of all WT mice across all age groups were 220-260 μm, and 310-370 μm for OS/RPE layers. However, the depths selected for the OPL layer for RhoKO mice were 175-205 μm for the 4 week old RhoKO, 155-195 μm for the 8 week old RhoKO and 120-160 μm for the 12 week old RhoKO, all relative to the tissue surface. Similarly, the typical depths selected for the OS/RPE layer for RhoKO mice were, 260-300 μm for 4 week old RhoKO, 240-280 μm for 8 week old RhoKO, and 190-250 μm for 12 week RhoKO. The thinning of the retinal layers for RhoKO mice as they age was also observed in the histology slides. Histology images of the WT and RhoKO mice at different aging stage are shown in Figure 4.18 below. Changes in the depth selection for different stages of the model are to be expected due to the progressive degeneration of photoreceptors in the RhoKO model. The decay of the correlation energy with length is similar for the OS/RPE and NFL layers but different for the OPL layer.

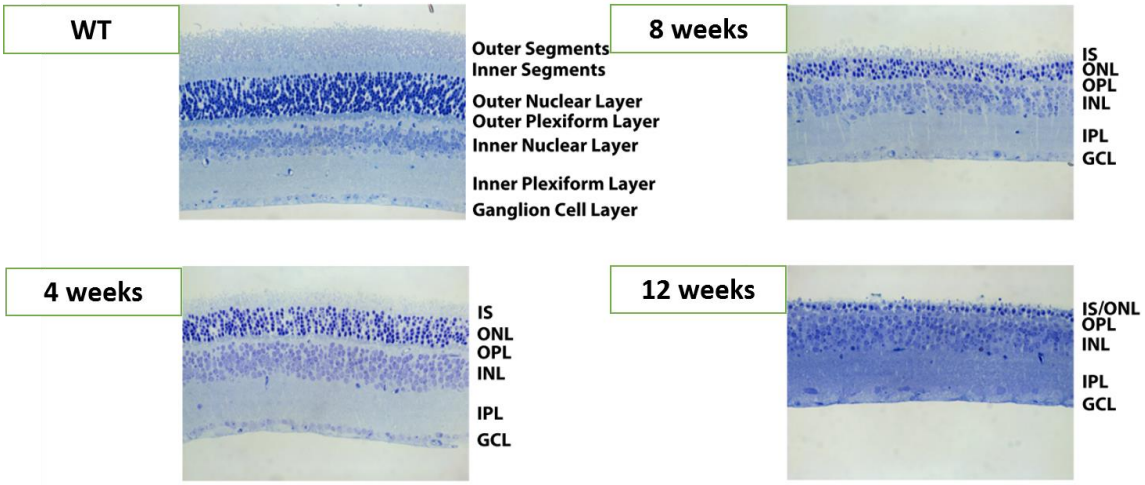

Figure 4.18. Histology images for 8 weeks old WT mice and 4, 8 and 12 weeks old RhoKO mice demonstrating the thinning of the retinal layers in RhoKO mice as they age.

To quantitatively compare the correlation energy in the three layers for the WT and RhoKO mice, the power law exponent was evaluated across the 20-90 μm range at each corresponding depth as indicated by the blue box in Figure 4.17b. The power law exponent was determined for WT and RhoKO mice ranging from four to twelve weeks of age (Figure 4.19), which is the time window during which retinal degeneration progress occur in these animals as shown in the histology images in Figure 4.18.

The power law fit analysis determined a significant difference in power law exponent across the same layers between the WT and RhoKO animals. The greatest difference in power law exponent was found between the OPL and OS/RPE layer. For the OS/RPE layer, a two sample t-test between the WT and RhoKO mice resulted in a p-value less than 5.8E-10 for all time points. For the OPL layer, a significant difference (p-

value of 3.1E-5) was observed only for the 12 week old mice, the age at which retinal regeneration is mostly completed. No statistically significant changes were observed for the NFL layer which is consistent with the disease model where degeneration does not affect the NFL. Due to the limited angular range collected through the mouse pupil and the imperfection of optical properties in the mouse lens, nuclear size determination with Mie theory analysis was unsuccessful across different layers and animal types yielding different sizes of scatterers with non-converging and often non-unique solutions.

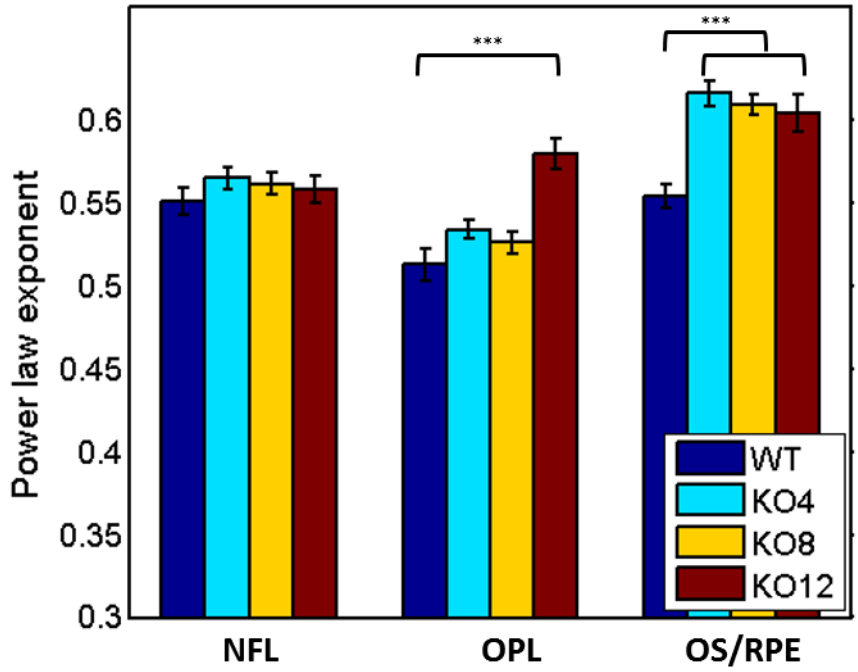

Figure 4.19. Calculated power law exponent across 20-90 μm correlation length range for NFL, OPL and OS/RPE layers for each type of mouse. The error bar indicates standard error of the mean. Figure taken from [61].

4.2.4 Discussion

Similar to the rat esophageal tissue experiment in the previous section, the combination of OCT and a/LCI allows for better localization of structural features when analyzing the mouse retina model. In this case, the OCT image helps to navigate across the sample and to locate identical ROIs for a number of different samples. The ONH was located first using OCT to position the 2D a/LCI beam at the center of the sample, serving as a reference point to designate the locations of the imaged ROIs. Also, the OCT image was utilized to identify histological layers of the mice retina, which then was registered side by side with the a/LCI depth measurement. Compared to the preliminary experiment where separate a/LCI and OCT systems were used to image the sample, the real time imaging guidance greatly improved the effectiveness of a/LCI measurements.

The power law fitting technique developed from the esophageal experiment was shown to be capable of discriminating healthy from abnormal mice tissue. The power law exponent measured for RhoKO mice at the OS/RPE layer was significantly higher than that of wild type mice across all ages of the mice as early as 4 weeks old. In addition, a significant difference was determined in the power law exponent at the OPL layer in 12 week old RhoKO mice compared to the WT mice. These results demonstrate that a/LCI is not only capable of extracting depth-dependent cellular scale information based on the inverse scattering theory but also has the potential for early detection of degenerative retinal disease using long range correlation analysis.

4.4 Summary

In this chapter, the utility of a combined OCT and 2D a/LCI system in imaging *ex vivo* tissue samples was demonstrated. The multimodal system shares a co-registered FOV that provides a unique characterization of the sample structure which cannot be obtained using a single modality. The OCT system serves as real time image guidance for the 2D a/LCI depth measurements and ensures proper sample orientation and registration of light scattering measurements to specific histological layers identified by the OCT image, providing a more effective analysis of the depth resolved scattering information.

The OCT guided, 2D a/LCI angular dependent scattering field measurement reveals nuclear and cellular morphology information and long range correlation measurements that are typically inaccessible by OCT imaging alone. With the real time imaging guidance of OCT, the rejection of improperly oriented tissue sites can reduce a/LCI post processing time for the samples that are more prone to non-unique nuclear size fits, as demonstrated with comparison of the folded and flat esophageal tissue. In addition to nuclear size determination, power law analysis was developed to investigate the long range correlation within the esophageal and retinal tissue. The power law exponent can be simply related to the fractal dimension which describes the self-similar nature within the tissue. The power law exponent analysis revealed significant difference in retinal layer structure across healthy and diseased mouse retinal models

which could be used in future studies. The application of the combined system to *ex vivo* tissue samples demonstrates the potential utility of the system for discriminating disease states.

5. Development of Low-Cost OCT System

In this chapter, we describe the design and implementation of a portable, low-cost OCT system that has comparable imaging performance to commercially available systems for point-of-care applications. Theory and technological information of OCT and SD-OCT systems are discussed in section 2.2. The cost reduction strategy and corresponding design for each component are discussed in detail, and the performance of the low-cost system has been carefully characterized and compared to commercially available OCT systems. *In vivo* and *ex vivo* imaging of animal tissue was performed to demonstrate the feasibility of the system for point-of care-clinical imagining.

5.1 Motivation

Despite the fact that OCT is the benchmark imaging technology for retinal imaging in ophthalmology [12], access to OCT retinal imaging has been limited to mostly large eye centers and laboratories due to its high system cost [27]. Thus, there is a significant opportunity to open up the use of OCT in a wide range of application especially for low resource setting if a low-cost device were available. Cost reduction and system portability have been a growing interest for the OCT community and multiple research groups have developed various portable small-scale OCT systems. The efforts in miniaturization of the OCT system include development of a handheld SD-OCT system for primary care diagnostics [32] and reduction in scanner form factor by using a MEMS mirror instead of galvanometer mirror [31]. Recently, a miniaturized,

low-cost, fully packaged silicon photonic integrated swept-source OCT has been developed [33] and a low-cost handheld linear OCT that could be built using only standard off-the-shelf inexpensive components has been demonstrated [34]. However, the OCT systems of these engines are either still bulky or expensive or suffer significant sacrifice of imaging performance.

5.2 Hardware Development

Among the SD-OCT hardware components (Section 2.2.2), the broadband light source, spectrometer and scanning optics are traditionally the most expensive and bulky elements [78]. In designing the system and its subunits, we aimed to use as many commercial off-the-shelf components to minimize the overhead from margin stacking which is commonly found in commercial systems. In addition, rather than focusing on optimizing individual parts, we took a system level approach to cost reduction and miniaturization in the total construction of the system that meets the desired performance. Multiple iterations and tradeoffs were made in component design and performance to reduce the price, but the targeted system performance was ensured through each iteration of the system through the design process.

For the light source, we used a non-temperature controlled, single mode fiber coupled superluminescent diode (SLD) instead of a temperature controlled SLD. For the spectrometer, a custom, robust spectrometer was designed using a tall pixel CMOS line array and off-the-shelf optics in a 3D printed housing. In order to design a novel and

inexpensive scanning system, we considered using a liquid lens scanning system which was characterized thoroughly. However, the liquid lens technology did not meet the targeted system specification, and an alternative approach using a scanning mirror has been adopted. Finally, the entire system is packaged in a sheet metal enclosure, approximately the size of a shoe box with an integrated computer inside.

5.2.1 Spectrometer

In our spectrometer design, the manufacturing cost was reduced by using a less expensive diffraction grating, a CMOS line senor, and 3D printed housing. A tall pixel array CMOS sensor provides greater tolerance to optical misalignment and system perturbations and enabled the use of the 3D printed housing. Two different tall pixel line array detectors were investigated in depth for optimization.

5.2.1.1 Design and Implementation

Multiple iterations of the spectrometer were designed using OpticStudio (Zemax) to optimize its performance. Instead of using custom cut lenses which are typically used in commercial spectrometers use to optimize the system performance, we used off-the-shelf optical elements in the design. The spectrometer utilizes a transmission grating in a mirror-grating-lens, loop configuration as shown in Figure 5.1. A transmission grating was chosen over a reflective grating in order to maintain a compact form factor for the system. Lenses were chosen over mirrors for the focusing

element to eliminate off-axis aberration. Since the wavelength range of the spectrometer is relatively small, the system had relatively low chromatic aberration.

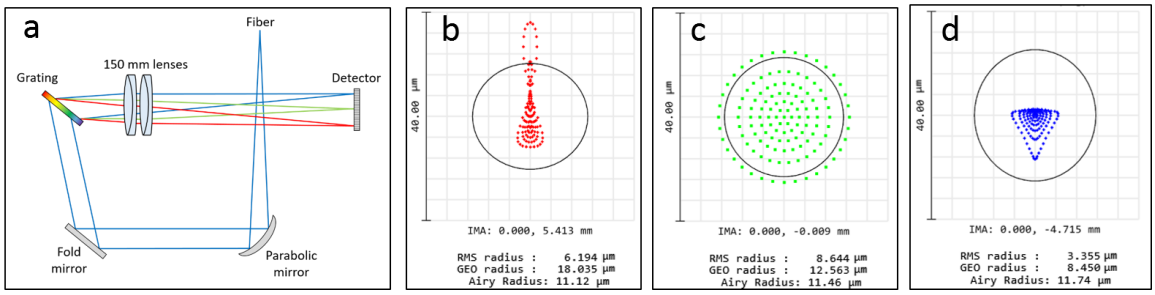

Figure 5.1. a) Schematic of loop spectrometer. Zemax spot diagram of the loop spectrometer design b) at 815 nm, c) 840 nm, and d) at 860 nm. Figure taken from [79].

Light was fiber-coupled into the spectrometer where the fiber core acts as a pinhole, serving as the entrance aperture. The incoming light is collimated using a parabolic mirror. The parabolic mirror greatly reduces the spherical aberration compared to a spherical mirror. A fold mirror is used to reduce the form factor of the system, and reflects the collimated beam into the diffraction grating (1852 lines/mm, LightSmyth, T-1850-800s). After the diffraction grating, a pair of 150 mm focal length achromatic doublets (Throlabs, AC254-150B) focuses the diffracted light onto the detector. The stacked 150 mm doublet lenses were used instead of a single 75 mm achromatic double to reduce spherical aberration. Even with chromatic corrected lenses, the chromatic aberration was the dominant aberration in the system, followed by spherical aberration. The two 150 mm focusing lenses were separated by a 3 mm air gap to avoid ghosting artifacts caused by reflections off of the lens surfaces entering the detector (Figure 5.1a). Ghosting artifacts are problematic in interferometric applications

like OCT and occur when unwanted reflections interfere and creates a shifted "ghost" image on top of the original OCT image. However, by separating the two lenses further apart than the maximum detectable depth range of the OCT system, the ghosting effect on the final processed OCT image can be avoided.

For the detector, two tall pixel array sensors were considered. Both sensors have a 200 μm tall pixel geometry which is more tolerant to aberrations along the vertical axis of the pixel (perpendicular to the horizontal spectral dimension). When optimizing the spectrometer design, aberration along the tall pixel axis can be tolerated in order to improve the beam performance along the spectral dimension as shown in Figure 5.1b-d. The simulated spot size along the spectral dimension using this method was less than 10 μm RMS radius across the entire wavelength range, which is smaller than the pixel size of the two detector arrays (10 μm and 14 μm respectively). Also, the tall pixel geometry enables greater throughput stability in the system against temperature fluctuation and mechanical stress. This geometry also allowed the use of a 3D printed housing (Butadiene styrene, MakerBot Replicator 2X) to assemble the optical components and the detector. The pieces were printed using a 20% solid in-fill in a honeycomb structure. However, this created a temperature issue caused by air trapped within the honeycomb structure of the housing, causing deformation within the parts and misalignment when ambient temperature changed. To alleviate this problem, we simply drilled holes through the bottom wall of the spectrometer to allow ventilation to stabilize the

temperature inside. Lastly, in order to minimize any mechanical stress, rubber vibration isolators were placed under the spectrometer housing to prevent misalignment of the spectrometer.

5.2.1.2 Sensor and Triggering

The first sensor we tested (Awaiba, Orion 2k) contained 2048 pixels (10 μm x 200 μm), and had a line rate of 40 kHz with a 12 bit well depth. Although the sensor offered a faster line rate and smaller pixel geometry, there was an intrinsic problem with triggering and synchronizing the sensor. First, the development kit for the sensor read out raw data with even and odd pixels flipped, creating jigsaw shaped scans in the raw data, and side lobes in the frequency domain after Fourier transform of the spectra (Figure 5.2). In addition, the acquired data had to be flipped prior to processing, introducing another processing step which can further limit the speed of the system.

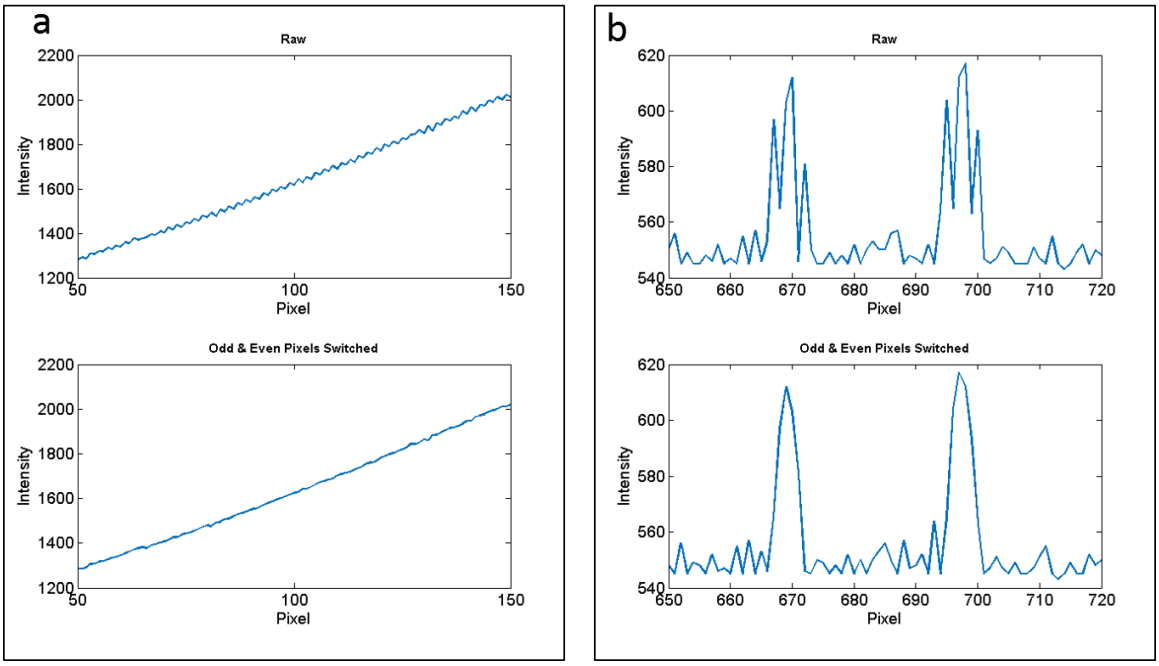

Figure 5.2. a) Partial raw spectrum of the light source acquired with Awaiba sensor before correcting the flipped pixel and after correction. b) Fourier transform of a mirror before pixel correction and after.

The sensor development kit offered both a hardware line trigger and frame trigger, with a minimum 1 ms gap between consecutive triggers. However, there was an inherent inconsistency with the frame grabber of the development kit. Although the sensor could potentially acquire at 40 kHz, the development kit could only support up to a 10 kHz line rate, and a new custom circuit board was needed to utilize the full speed of the sensor. In addition to the suboptimal line rate, missing lines were randomly dropped within the frame. To investigate this malfunction, a function generator was used to generate sinewave at fixed frequency. The detected beam pattern by the Awaiba sensor clearly show inconsistent line drops (Figure 5.3). This phenomenon is detrimental

to generating stable OCT images. The OCT image of a tape phantom using this sensor shows the discontinuity. The only way to ensure no dropped frames was to trigger each single line, resulting in less than 2 fps OCT B-Scans.

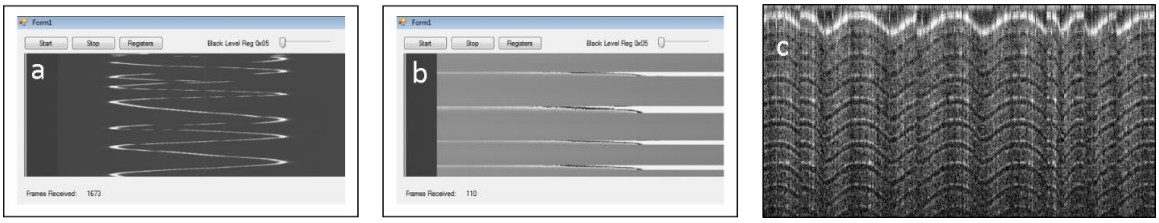

Figure 5.3. a) Sinewave and b) pulse train at fixed frequency captured by free running Awaiba sensor, showing the random frame drops across the acquisition. c) OCT tape image acquired with Awaiba sensor.

The second sensor (Hamamatsu) also contained 2048 pixels (14 μm by 200 μm) with 16 bit well depth. The sensor had a 10 MHz clock rate, capable of acquiring at a 5 kHz line rate with the full array and a 10 kHz line rate with half of the array. Although the 10 kHz line rate is about 4 times slower than the theoretical maximum of the Awaiba sensor, B-scan frame rates close to a true video frame rate (30 Hz) could be achieved with the new sensor. Importantly, the new sensor did not have missing lines within a frame, and a smooth OCT image could be captured. The sensor had a synchronization problem which was fixed by using an external master device which is discussed in detail in synchronization section (5.3.1).

5.2.1.3 Performance Characterization

With the current spectrometer configuration, half of the detector array covers a wavelength range from 801.2 nm to 864.7 nm (Figure 5.4a). The 63 nm bandwidth

captures the entire light source spectrum, but if a larger bandwidth source is adopted, in an effort to improve axial resolution, the second half of the detector can be used. The FWHM spot size measured on the sensor was 19.6 μm, and 6 dB falloff of the spectrometer was beyond 1.5 mm, as indicated in Figure 5.4b. Finally, an A-scan line rate of 8.8 kHz was achieved.

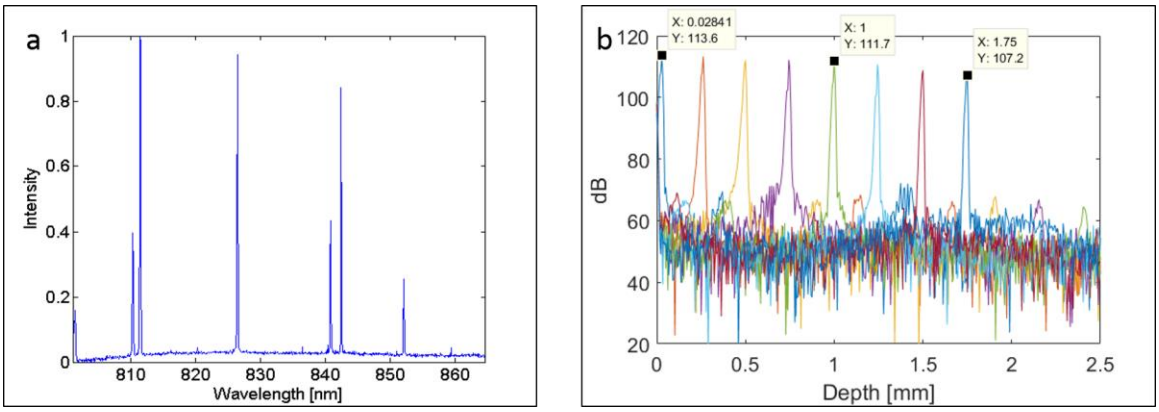

Figure 5.4. a) Argon calibration source spectrum measurement for wavelength calibration and FWHM measurement. b) The spectrometer falloff measurement.

5.2.2 Light Source

The broadband light source is another expensive element in traditional SD-OCT system. Our approach to reduce the price for the light source was adopting a non-temperature controlled, fiber coupled superluminescent diode (SLD). These types of light sources are typically avoided in designing interferometric system like OCT, because the temporal fluctuations of a non-temperature controlled source result in the fluctuation of the output power and spectral properties. In the final processed OCT B-scan image, these fluctuations create a common path artifact which can be avoided when

a temperature controlled light source is used. The unstable output from the light source also reduces the SNR of the system by adding a DC component to the final processed image. However, if the temporal fluctuation occurs at a slow rate compared to the acquisition rate, regular acquisition and update of the background spectrum can minimize these artifacts. Even traditional OCT systems require regular updating of the background spectrum in order to optimize the image contrast. Thus, these imaging artifacts and degradations can be reduced without slowing down the overall acquisition time.

Two SLD candidates that meet the performance criteria were considered: the Superlum Minibut SLD and the Exolas butterfly SLD. The desired specifications for the light source were a center wavelength near 830 nm, a bandwidth greater than 40 nm, and an output power greater than 2 mW. A larger bandwidth provides higher axial resolution, and a higher output power is desired for improved SNR. The power stability measurement over time for the two selected SLDs are shown in the Figure 5.5 below. The Butterfly not only had a higher output power, but also showed less power drift over time. In addition, the Superlum SLD suffered higher power fluctuation when there was back reflection present. Thus, based on the higher output power stability, the Exalos Butterfly was selected as the broadband light source for the system. The SLD has an 840 nm center wavelength with a 45 nm FWHM bandwidth over 7 mW output power, and

most of the bandwidth of the source spectrum is captured with the final spectrometer design using only half of the detector array.

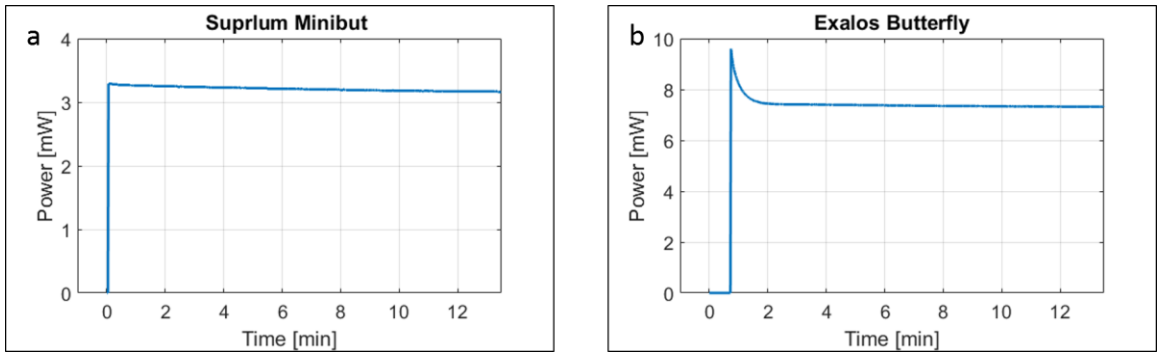

Figure 5.5. Power stability measurement for a) Superlum Minibut, and b) Exalos Butterfly.

5.2.3 Scanning Optics

For the scanning optics, a liquid lens and MEMS scanning mirror designs were considered. A liquid lens scanning scheme is attractive because liquid lenses are much cheaper than MEMS mirrors. However, the liquid lens technology for scanning is fairly new, and there is no OCT system that has utilized the liquid lenses for scanning. Therefore, we performed a series of performance characterization with liquid lenses to test its viability for the OCT scanning optics.

5.2.3.1 Liquid lens Scanning Implementation

A liquid lens is a tunable lens that can change its focusing power without any mechanical moving parts by controlling the shape of the liquid surface within the lens. The shape of the liquid can be precisely controlled by electrostatic pressure or mechanical stress to change its focal length from a few centimeters to infinity. In

addition, beam steering is enabled by the addition of more control electrodes to create an asymmetric shape change. A single lens (Varioptic, Baltic 617) can steer the beam at a maximum angle of ±0.6° with step resolution of 0.01° on top of the focus length variation. Two of these liquid lenses, when combined back to back, can achieve ±1.2° angular range or a scanning field of view (FOV) of 3 mm by 3 mm when combined with a 75 mm focal length lens. The feasibility of the liquid lens scanning set up was first examined by characterizing the liquid lens performance.

First, a single liquid lens was placed in between a 75 mm focusing lens and a collimated light source to investigate which orientation is suited to design an infinity corrected optical system. The infinity corrected system minimizes spherical aberration and provides a tighter spot across the FOV, especially near the edge of the scan. The collimated light had a 2.3 mm FWHM spot size before entering the liquid lens, which is limited by the size of liquid lens aperture (2.4 mm), and a camera was placed at the focal plane of the focusing lens to image the spot. When the collimated light was focused into the camera without any liquid lens, the FWHM of the beam was measured to be 38.6 μm. The spot size was measured at different distances from the center when controlling only the tilt of the liquid lens without changing its focus. Two sets of measurements were performed in order to determine which liquid lens orientation achieves a smaller spot size as shown in Figure 5.6.

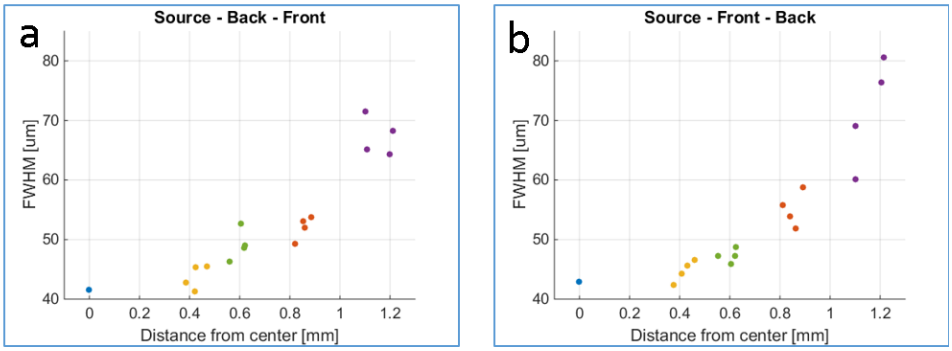

Figure 5.6. FWHM spot size measurement at different distance from the center a) when the back of the liquid lens was facing toward the light source, and b) when the front of the liquid lens was facing toward the light source.

In an OCT system, the lateral resolution is set by the focused spot size given by equation 2.4 in section 2.2.4, and a spot size under 30 μm is desirable for biological OCT imaging. For both orientations, the spot size at the center in which the liquid lens was not used to deflect the beam was larger compared to the spot size measured without a liquid lens. The spot size near the edge of ±1.2 diagonal scan when the back of the liquid lens was facing the source was smaller (~70 μm) compared to the spot size with the flipped lens orientation (~80 μm).

Next, two liquid lenses were inserted with four different combinations: Back-front, back-back, front-back, and front-front. The spot size measurements for both single lens and double lenses are summarized in Figure 5.7**.** Four spots were measured at varying distances along a single direction from the center for four directions, and the average of the FWHM spot size is reported for these measurements. Having the back side of the liquid lens toward infinity space resulted in the smallest spot size across the

scan for both the single lens and double lenses configuration. Also, with the double liquid lenses configuration, a 4.6 mm diagonal scanning range and 3 mm x 3 mm (x-y) FOV was achieved.

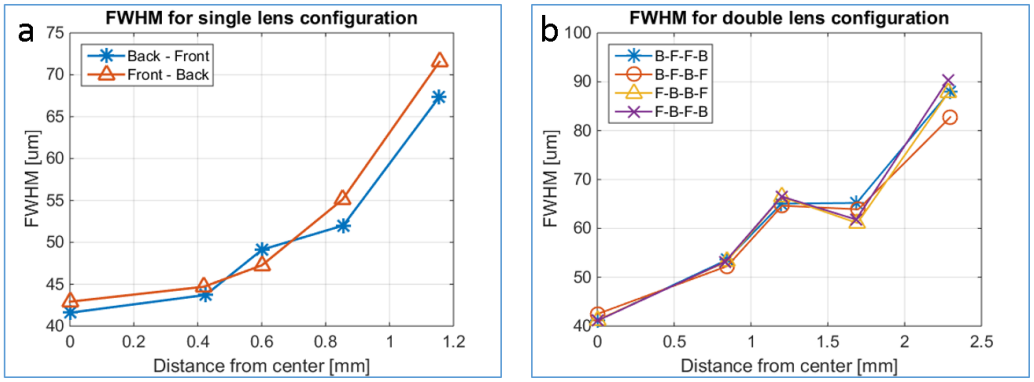

Figure 5.7. FWHM spot size measurement at different distance from the center with multiple lens orientations for a) single lens, and b) double lenses.

Although the combination of the two liquid lenses for beam steering provided sufficient scanning range, the spot size was enlarged along the scan, reaching over 80 μm near the edge. The spot size can be improved with a shorter focal length focusing lens. However, there is tradeoff between the spot size and the maximum FOV. Instead of adopting a shorter focal length lens, the focusing power of the liquid lens was tuned to minimize the spot size on the sample plane. The measured intensity of the beam scan at the focal plane using two consecutive lenses set up is shown in Figure 5.8a. The 89.3 μm spot at the edge marked by a red circle was then refocused using two methods. For the first row of the image in Figure 5.8b, the focal length of the first lens was shortened (higher voltage), while the focal length of the second lens was lengthened (lower voltage). For the second row, the focal length variation was reversed. The first method

reduced spot size down to 60.4 μm while the second method only reduced the spot size to 72.9 μm. Note that there is a spot shift when the focus is readjusted (98.5 μm shift away from the center for the first method, 80.8 μm shift toward the center for the second method). The focus adjustment values were determined by optimizing the intensity of the spot at each location manually.

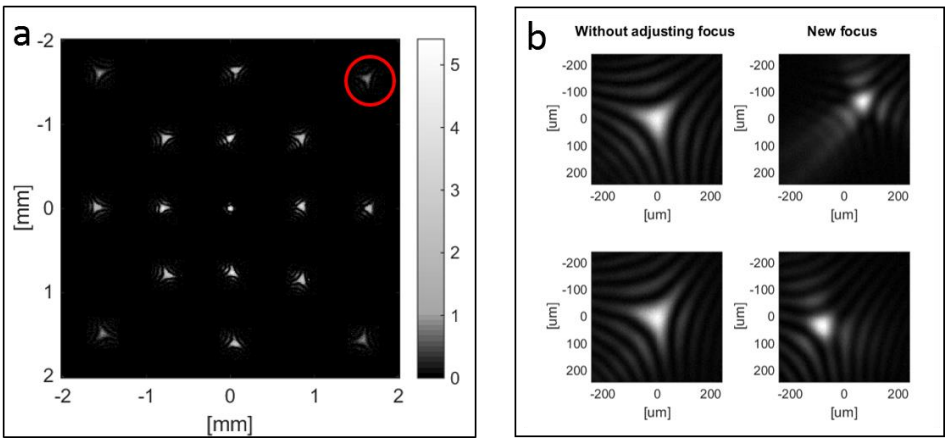

Figure 5.8. a) The measured intensity of the beam scan at the focal plane using the two liquid lenses. b) The spot profile with and without adjusting focus at the edge of the scan marked by the red circle in a). For the first row of the image, the focal length of the first lens closer to the collimated beam was shortened, while the focal length of the second lens was lengthened. For the second row, the focal length variation was reversed. Figure taken from [79].

The same refocusing method was applied to each spot along the entire diagonal scanning range at the step size of 0.1° to investigate the reduction in spot size. Each step increment was made by a 0.05° shift for both liquid lenses (total of 12 steps), and an improvement in the spot size is noticeable when the beam is more than one millimeter away from the optical axis (Figure 5.9).

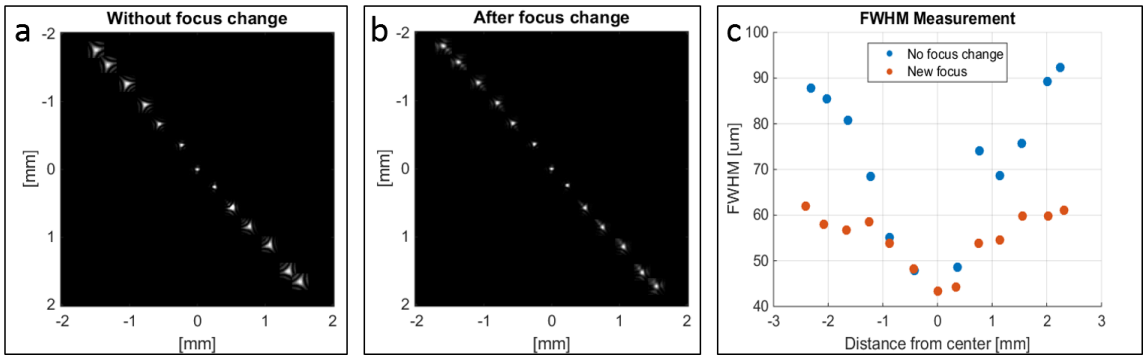

Figure 5.9. The measured intensity of the diagonal beam scan using two liquid lenses a) without adjusting the focus and b) after adjusting the focus. c) FWHM spot size measurements at different distances from the center with and without changing the focus.

From the scatter plots of FWHM spot size vs. the distance from the center (Figure 5.6), there are some inconsistency of the measured FWHM spot size measurements and distance from the center although the same voltage values were applied in 4 different directions. In addition to the inconsistency, the distance between the consecutive spots are not equally distant apart in Figure 5.9, even though the step size for each measurement was identical. These observations may affect the linearity and repeatability of liquid lens scanning which would need to be considered when designing a reliable scanning scheme. When the distance between each adjacent step was calculated, the uneven spacing between spots is more evident, especially at the edge of the scan (Figure 5.10a).

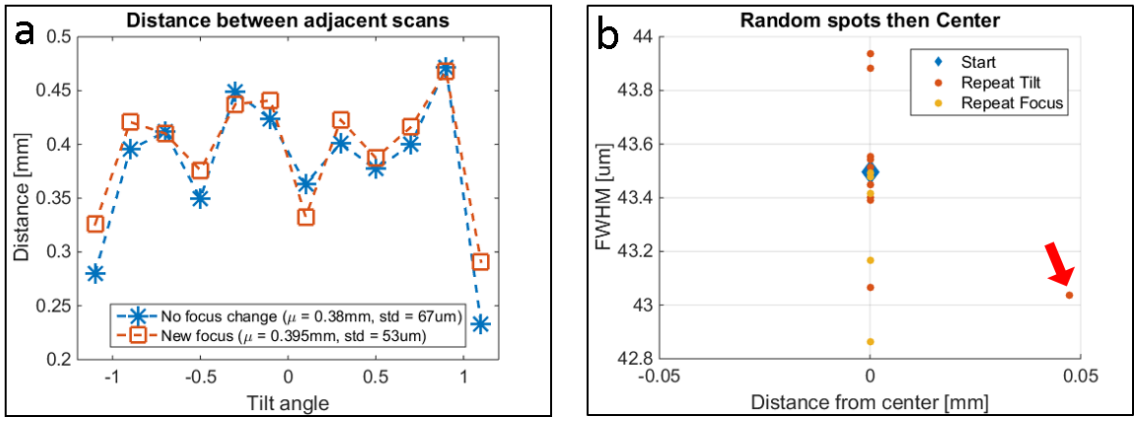

Figure 5.10. a) The mean distance between spots when 0.1° step jumps are made across the scan. b) FWHM spot size and deviation from the center when either focus or tilt was changed to an arbitrary value and changed back to the original value.

The mean distance between each spot was 380 μm with standard deviation of 67 μm without adjusting the focus while the mean distance between each spot with refocusing was 395 μm with standard deviation of 53 μm. This measurement highlights the nonlinear response of the liquid lens tilt, such that more deliberate mapping of the input voltage values must be determined to achieve the linear scanning. In order to investigate the repeatability of the liquid lens, the beam tilt and focus was randomly adjusted to arbitrary values, and then moved back to the original tilt and focus. The center of the beams in all trials except one case came back to the original spot when only the tilt was adjusted, although there was variance in the beam shape with both tilt and focus variation, resulting in an inconsistent FWHM at the center (Figure 5.10b). The one trial that failed to position the beam to the original spot showed about a 50 μm shift in position. One last experiment was performed to investigate the repeatability issue,

which might arise from the hysteresis of the liquid lens. On a single liquid lens, the spot was moved from the center to the left edge by a step resolution of 0.1°. Then the beam was moved back to the center with the identical step size, and two round trips were made (Figure 5.11a). The FWHM and the position of the beam at each spot was measured. Again, a 50 μm shift was observed at the center as marked by a red circle, and 5 μm shift was observed at 0.52 mm away from the center (Figure 5.11b).

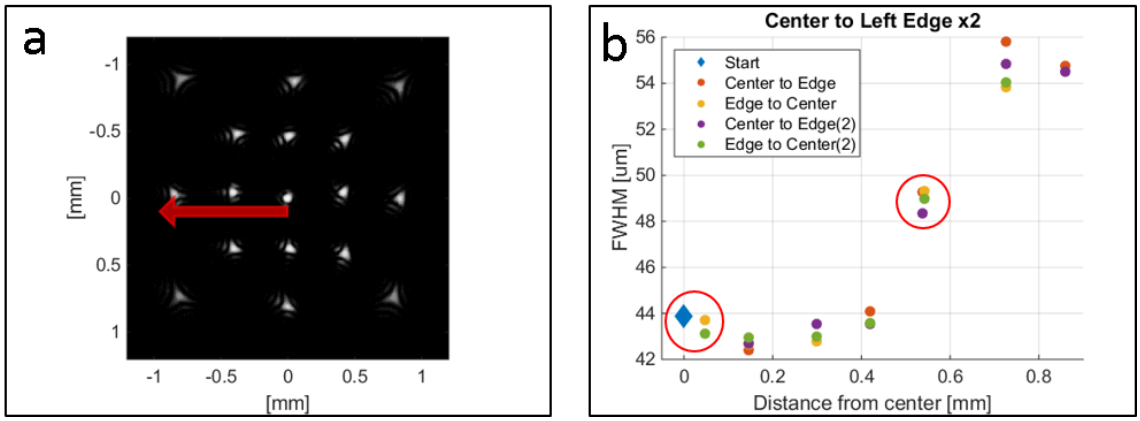

Figure 5.11. a) The measured intensity of the beam scan at the focal plane with one liquid lens indicating the direction of the scan for hysteresis study. b) FWHM and position measurement for two repeated scan toward the left edge of the FOV.

Another limitation for the liquid lens scanning scheme was its response time. The liquid lens has typical response time of 20 ms to refocus and 50 ms to change the tilt. Although 20 Hz scanning was possible, only 10 Hz scanning rate could be reliably achieved without suffering the flickering. At higher scanning speed, the lens response became more nonlinear.

Even with a number of limitations for the liquid lens designs, the double liquid lenses scanning system was integrated into the low-cost OCT engine to evaluate its feasibility. The scanning speed was set to 10 Hz for stability, and dynamic focusing was not implemented in real-time scanning so that spot sizes ranged from 40 to 60 μm within a 2 mm FOV. An example OCT image of a tape phantom on a business card is shown in Figure 5.12a. In spite of the poor lateral resolution and small FOV, the lateral and axial structures are easily distinguishable throughout the full imaging depth. The additional advantage of implementing two liquid lenses in the scanning optics, besides cost reduction, was the capability to extend the focal plane within the imaging and even through an extra optics element. This could be used, for example, to image between the retina and the cornea of an eye without any additional optical elements by simply changing the focal power of the liquid. This technique is demonstrated by extending the focal length to 30 mm beyond the original imaging plane (Figure 5.12b.2), and refocusing the beam by changing the focal power of the two liquid lenses (Figure 5.12b.3). The two liquid lenses combined had sufficient optical power to focus the beam into a tight spot, and OCT image at the new focal plane can be captured by just changing the reference path without changing the scanning optics. (Figure 5.12c).

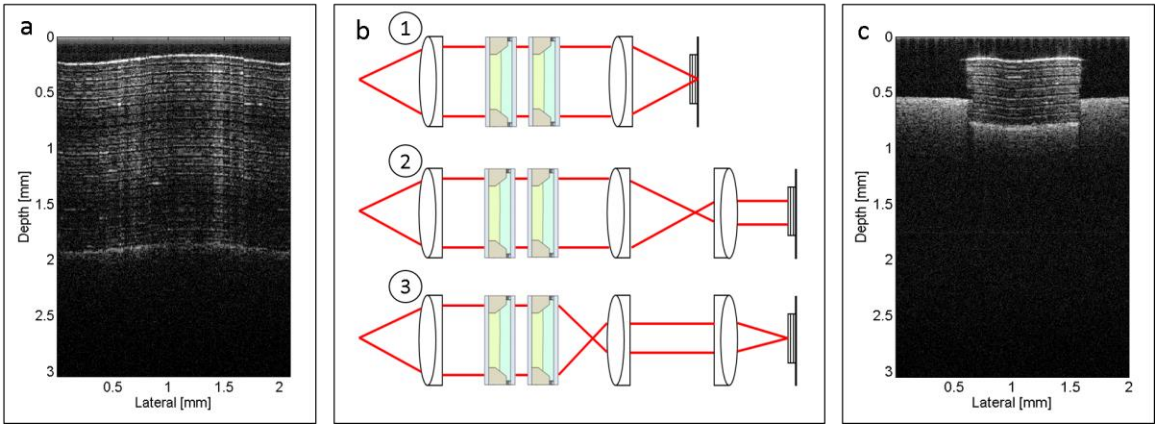

Figure 5.12. a) OCT scan of a tape phantom on a business card with set up in b) Liquid lenses schematics showing dynamic focusing capability. The top set up (1) is a default set up of the scanning optics. The middle set up (2) is when an extra focusing optics is inserted at the end without changing focal power of liquid lens. The bottom set up (3) is when liquid lens focusing power was changed in order to cancel the effect of the inserted lens in (2). Even with introduction of an additional optics in setup (2) compared to the setup (1), the liquid lens can be tuned to adjust focal plane without any moving parts as in setup (3). c) OCT scan of the same sample with set up in b (3).

Overall, the liquid lens technology has a high potential to be used as cheap alternative scanning optics, but the current state of the technology has its limit as a reliable scanning scheme in biological and clinical applications mainly due to its limited response time unstable repeatability. Also, a spot size under 20 μm is desirable for high lateral resolution imaging, and at least a video frame rate is required for real-time feedback for clinicians. For liquid lenses to be viable to replace scanning mirrors in OCT systems, it must have a larger aperture to realize a smaller spot size, stable repeatability with less hysteresis, a higher tilt range to implement a larger FOV, and a faster response time to enable video rate scans. Once the future generation of the liquid lens technology

meet these criteria, the liquid lenses will be a great alternative for scanning mirrors in optical imaging systems.

5.2.3.2 MEMS Mirror Incorporation to Scanning Implementation

An alternative approach for a scanning scheme was developed using microelectromechanical mirrors (MEMS). The MEMS mirror based scanning is widely adopted in various OCT applications [31]. The MEMS mirror (Mirrocle) used for the design has a 3.6 mm diameter, and ± 6° x-y tilt range. Due to the larger aperture and higher tilt range of the MEMS mirror compared to the liquid lens, a shorter focal length lens could be adopted to achieve a significantly tighter spot size without compromising the FOV (Figure 5.13a). Based on a 30 mm focal length focusing lens, a 17.6 μm spot size was obtained at the center of a 7 mm by 7 mm FOV. In addition, the spot size near the edge of the scan, 3.5 mm away from the center, remained under 24 μm (Figure 5.13b) while the spot size of the liquid lens scheme was about 90 μm, measured 2.4 mm away from the center. Although the MEMS mirror approach is more expensive than the liquid lens design, the MEMS mirror provides a much smaller spot size and larger FOV. In addition to the MEMS mirror, we incorporated a focus tunable liquid lens for dynamic focusing, assigning the scanning and dynamic focusing control to two independent optical elements. The liquid lens has 10 mm diameter (Optotune) and with the liquid lens and MEMS mirror combination scheme, the scanning is no longer a rate limiting

step. Integrating a focusing liquid lens allows adjustment of the focal plane to anywhere within the imaging depth FOV without sample position readjustment.

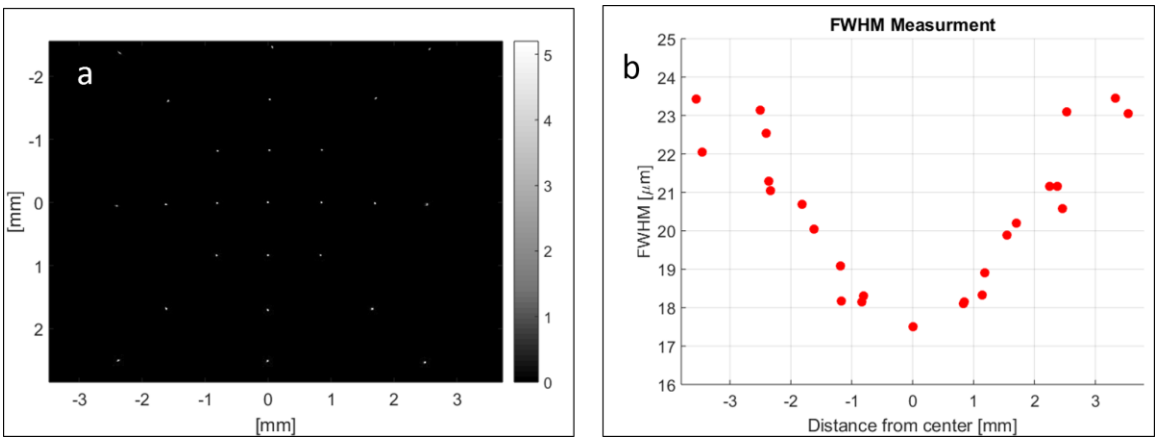

Figure 5.13. a) The measured intensity of the beam scan at the focal plane using a MEMS mirror and a liquid lens scheme. b) FWHM spot size measurement at various distance from the center without adjusting focus of the liquid lens. Figure taken from [79].

5.2.3.3 Reference Arm

In order to match path length of the scanning optics in a cost effective fashion, a simple reference arm was designed with an adjustable lens tube instead of a conventional linear translation stage. The reference arm optics, including the mirror and lenses, were mounted in threaded adjustable length lens tubes such that the position of the optical elements can be precisely adjusted along the optical axis of the system while conserving space and cost. Intensity can be controlled by defocusing the beam on the mirror mounted at the end of the reference by manually adjusting the threading of the lens tubes. This changes the intensity of the reference beam coupled back into the optical fiber to the spectrometer. An extra adjustable lens tube allowed manual adjustment of

the path length and decouples the path length and intensity control. The reference tube was placed within the OCT housing, since the focal plane change within the imaging depth for various samples with different index of refraction can still be tuned by refocusing the liquid lens.

5.2.4 3D Printed Housing and Optical Assemblies

In addition to the 3D printed housing for the spectrometer (Figure 5.14a) as discussed in section 5.2.1.1, the majority of the optical assembly components were fabricated using 3D printing (MakerBot, Replicator 2X and Formlabs, Form2) including the scanner housing, SLD mount, fiber polarization paddles, and fiber management spools (Figure 5.14b). The 3D printing technology allowed greater freedom in designing the optical assemblies, reduced the manufacturing cost, and increased the portability of the system. The 3D printed parts were designed to be more compact and lighter weight than those found in most commercially available parts by printing using acrylonitrile butadiene styrene (MakerBot) and Tough FLT0T04 (Formlabs) materials. As discussed earlier, holes were drilled in the 3D printer parts to dissipate heat within the honeycomb structure of the parts. In addition, the 3D printed enclosure was designed to hold a mini PC on top of the OCT housing in such a way that the cooling fan of the mini PC ventilates the heat out of the OCT system while allowing easy access to the PC power switch and USB ports (Figure 5.14c).

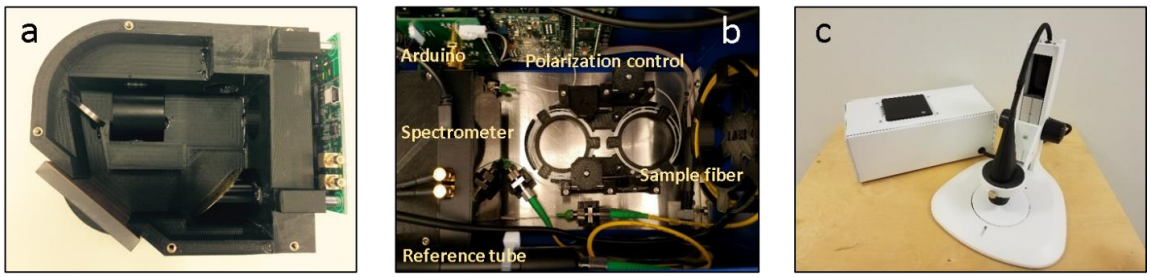

Figure 5.14. a) 3D printed spectrometer housing with mounted optics. b) Interior view of the low cost system engine and c) exterior view. Figure taken from [79].

5.3 Software Development

In the prototyping stage, individual subsystems were controlled by both LabVIEW and Matlab within an integrated LabVIEW interface. Data acquisition and OCT processing were executed in the LabVIEW interface while the voltage driven MEMS mirror was controlled in a custom Matlab program. In order to synchronize the MEMS mirror scanning with the sensor data acquisition, an Arduino was used as a master timing device bridging the subunits.

5.3.1 Synchronization

In order to produce stable OCT B-Scan images without timing jitters, the scanning and data capture must be in phase. Both the Hamamatsu sensor and MEMS mirror have multiple triggering options. The MEMS mirror offers both trigger in and trigger out capabilities, and according to the manufacturer's manual for the development kit, the sensor was capable of generating a line trigger out, and taking line and frame trigger in. However, the frame trigger on the sensor was not implemented in

the development kit although it was mentioned in the manual, so line triggering was used to synchronize the sensor and MEMS mirror. Among the two devices, the MEMS mirror had a faster response time to the trigger in while the sensor had a short delay prior to acquiring when triggered. Therefore, final triggering scheme was implemented with the detector outputting the line trigger to the MEMS mirror.

Although the Hamamatsu sensor did not drop lines within a frame randomly like the Awaiba sensor and generated a consistent number of lines per frame, the triggering out pulse was inconsistent. The development kit did not output one pulse per line, nor the same number of output pulses per frame. For example, when the number of pulses within a pulse train were counted with an Oscilloscope for 100 lines per frame, the number of pulses measured could vary from 243 to 248 instead of expected number of lines near 100 counts. The MEMS mirror was programmed in MATLAB to start scanning at a fixed pattern and rate when the start trigger was received.

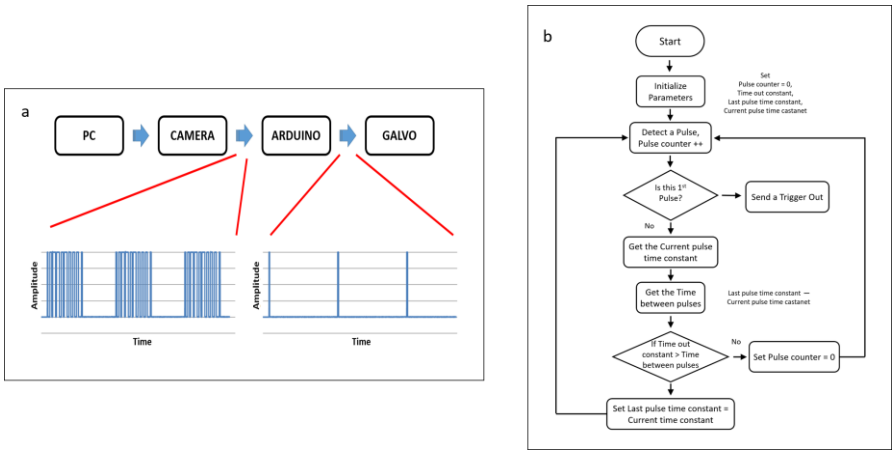

Figure 5.15. a) Pulse train conversion into frame trigger using Arduino. b) The control flow diagram using the Arduino for synchronization

In order to ensure a consistent triggering pulse is delivered to the MEMS mirror from the detector, a microcontroller (Arduino, UNO Board Rev3) was implemented (Figure 5.15a). Since there is a delay between the pulse train due to the data transferring and processing time in between B-scans, the Arduino was programmed in Python to recognize the first pulse from the senor output train and the time gap between the pulse trains (B-scans). The control flow diagram of the Arduino is shown in Figure 5.15b. The Arduino sends out a trigger to the MEMS mirror when it recognizes the very first pulse of the pulse train, and the time gap detection again cues the Arduino to reset the scan and wait the start of the subsequent pulse train. The final system schematics with control flow using the Arduino for synchronization is summarized in Figure 5.16.

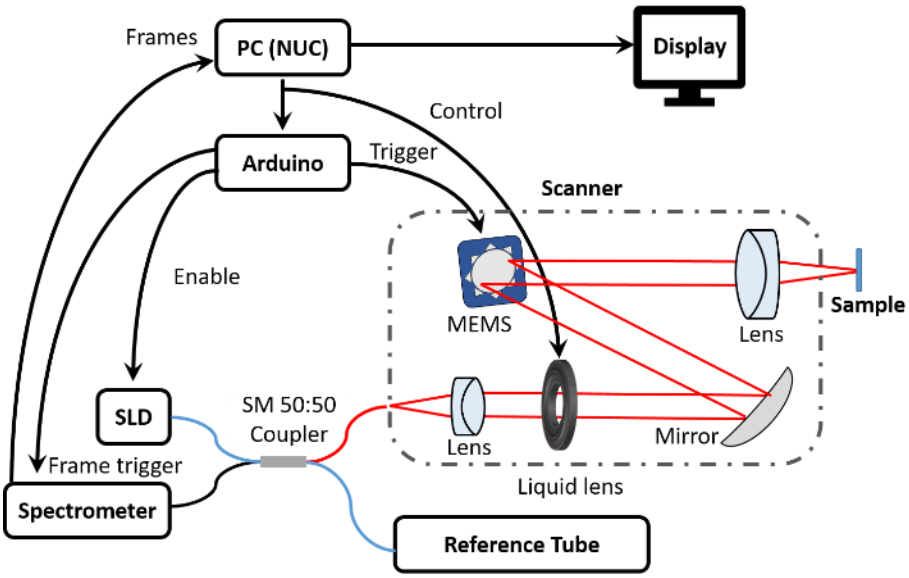

Figure 5.16. The system schematic using the Arduino for synchronization. Figure taken from [79].

5.3.2 Data Acquisition and OCT Processing

The camera capture sequence and real time image processing were written in LabVIEW. The camera first initializes the imaging parameters such as the trigger mode, line time, number of pixels, and number of lines per frame. As the camera starts capturing lines, its line trigger out mode is enabled. The trigger out pulse train is detected by the Arduino, and immediately triggers the pre-determined MEMS scanning. The camera waits until the specified frame is filled, then stops capturing and trigger mode is turned off. Another reason why the detector outputs an inconsistent number of pulses per frame is that although the frame is full and the camera is no longer acquiring, the trigger pulses are still generated until the trigger mode is turned off. The program then identifies if the captured frame is the sample spectrum or background spectrum determined by the "Update Background" button in LabVIEW UI. Once the background spectrum is captured, it is subtracted from every subsequent frame captured. Since the detected spectrum is linear in wavelength instead of wavenumber, the data are interpolated into evenly spaced wavenumber data. Numerical dispersion is digitally compensated [51] to correct the dispersion mismatch between the sample and the reference path (see section 2.2.3). The dispersion values can be changed in real time so that the user can adjust the dispersion while imaging. Finally, the data are Fourier transformed and only the real component is displayed in the LabVIEW UI.

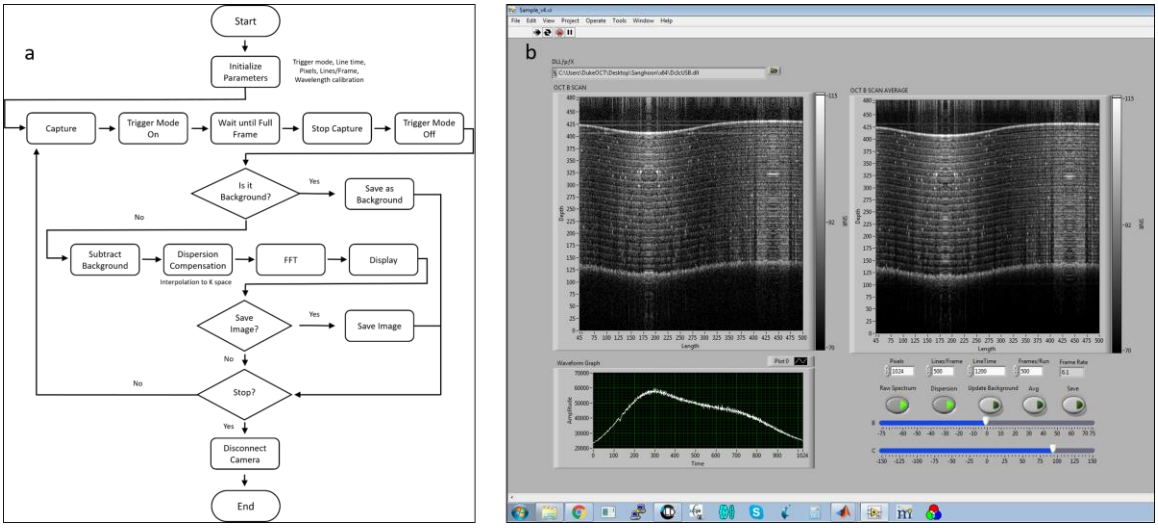

Figure 5.17. The control flow diagram using LabVIEW. b) LabVIEW interface acquiring OCT B-SCAN of a tape phantom.

The user interface also supports saving the final OCT B-scan images, as well as an averaged B-scan image. The number of averages can be specified, and the program holds the specific number of frames in its memory to enable real time B-scan averaging. The rate limiting step in the program was the interpolation step from wavelength to wavenumber space. The detector can acquire a B-scan consisting of 500 A-scans at 14 frames per seconds. However, the final image is displayed at 8 fps with spline interpolation and at 11 fps with linear interpolation. The drop in frame rate using linear interpolation was smaller than when used higher order interpolation, however, the image quality using linear interpolation had a lower contrast compared to that of using spline interpolation. The control flow diagram of the data acquisition and processing is summarized and the LabVIEW UI is displayed in the Figure 5.17.

5.4 System Characterization

In order to investigate the feasibility of the system, the performance of the current low-cost engine was characterized thoroughly and the total manufacturing cost was determined. Then we compared the device performance to a commercial SD-OCT system (Wasatch Photonics, Spark DRC), which costs more than five times as much with a side by side comparison of images of an identical phantom. In addition, the specifications of the low-cost system and other commercially available systems are summarized for comparison.

5.4.1 System Specification Measurements

The final system provides an axial resolution of 7 μm in air, and lateral resolution of 17.6 μm with 7 mm by 7 mm x-y FOV. The system has a maximum imaging depth of 2.8 mm with the variable focus capability, and the output power at the sample was measured to be 700 μW which is less than maximum permissible exposure for direct ocular exposure for long exposure greater than 1,000 seconds (International Electrotechnical Commission Standard). The B-Scan consisting of 512 by 512 pixels are displayed at 12 fps, and the software supports real time dispersion compensation, B-scan averaging and saving the images. The system is housed in a 14 inch x 7.5 inch x 5 inch case, approximately the size of shoe box, and the total weight of the system, including the integrated mini PC and the scanner head, is 6 lbs. The total manufacturing cost of the

system was under $7,200 and individual component cost break down is summarized in Table 1 below.

Table 5.1. Component Cost of Low-Cost OCT systems.

Component	Price
Spectrometer	
Detector	$1,200
Lenses	$420
Grating	$245
Grating Mount	$275
Folding Mirrors	$110
Subtotal	**$2,250**
Scanner	
MEMS mirror and driver	$2,000
Liquid lens and driver	$696
Lenses and mirrors	$180
Subtotal	**$2,876**
Optical Components	
SLD and driver	$536
Optical fiber	$179
Fiber splitter	$225
Reference arm optics	$316
Subtotal	**$1,256**
Electronics	
PC and accessories (USB hub, USB and HDMI cables)	$750
Arduino and Arduino shield	$32
Subtotal	**$782**
Total	**$7,164**

5.4.2 Comparison with Commercial Systems

The performance of the low-cost OCT system and a commercially available system were compared by imaging the identical sample with both systems, and comparing the low-cost system specifications to those provided by the commercial system manufacturer. To compare the B-scan images, a phantom consisting of multiple layers of Scotch Giftwrap tape was imaged with both the low-cost system and with a Wasatch commercial OCT system purchased in 2013 (Figure 5.18). The B-Scan images are 10 frames averaged images for both systems. The Wasatch system has a better axial resolution, using a larger bandwidth light source, and a better lateral resolution using a shorter focal length lens. The low-cost OCT system has a larger FOV, and depth of focus compared to the Wasatch system with a trade off in lower lateral resolution. However, the low-cost OCT system is capable of resolving individual tape layers through its entire 2.8 mm imaging depth. Normalization was performed based on the intensity of the superficial layer for both images for equal comparison of the depth of focus and the identical 5 mm by 5 mm images were captured with the both systems.

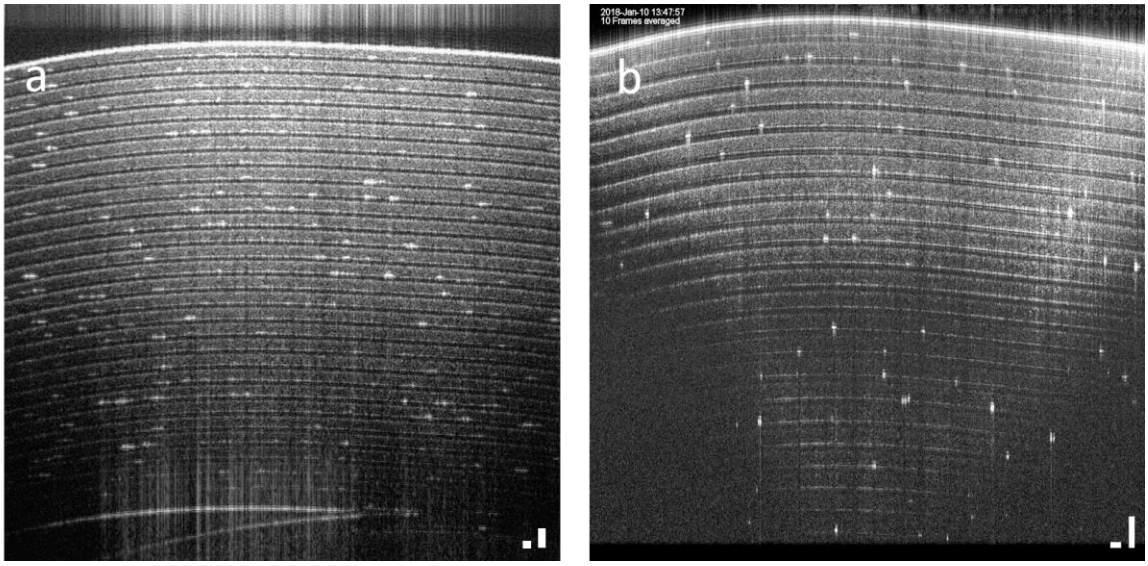

Figure 5.18. The OCT B-scan of a scotch tape phantom imaged by a) low-cost OCT system (scale bar, 100 µm) and b) Wasatch commercial system (scale bar, 100 µm). Figure taken from [79].

In addition to the image quality comparison, the system specification of the low-cost system has been compared with other entry level commercially available system (Thorlabs, Callisto CAL110C1) along with the Wasatch system. The system parameters including the price are outlined in Table 2. The system specifications of the commercial systems were specified by the corresponding vendors, and the form factors were measured experimentally. The low-cost OCT design achieved approximately a 5-fold cost reduction and more than 2-fold reduction in volume compared to the commercial OCT systems while maintaining competitive imaging performance.

Table 5.2. Specs of the low-cost OCT engine and commercial OCT systems

	Low-cost OCT	Wasatch	Callisto
Price	$7,164	$45,000[a]	$35,000
System Specifications			
Center Wavelength	830 nm	830 nm	930 nm
Number of pixels per A-Scan	512	1024	512
SLD Bandwidth (3db FWHM)	45 nm	155 nm	
Maximum output power	700 μW	750 μW	
Imaging Performance			
Imaging Depth (in air)	2.8 mm	1.9 mm	1.7 mm
Axial resolution (in air)	7.0 μm	2.0 μm	7.0 μm
Lateral resolution	17.6 μm	10 μm	8 μm
A-scan rate	8.8 kHz	40 kHz	1.2 kHz
Sensitivity	99.4 dB	100 dB	107 dB
Scan range (X and Y)	7 mm	5 mm	10 mm
Form Factor			
Weight (with PC)	6 lbs	44 lbs	
(without PC)		19 lbs	27.6 lbs
Volume	524 in^3 (with PC)	1,153 in^3 (without PC)	1,230 in^3 (without PC)

[a] Price from 2013 purchase.

5.5 System Validation on Biological Samples

The capability of the low-cost system to image relevant biological tissue was validated on *ex vivo* porcine cornea, murine skin, and *in vivo* murine retina.

5.5.1 Ex-vivo Measurements on Porcine Cornea

For the *ex vivo* experiments, no changes in the system optics were needed. A freshly excised porcine eye was prepared and 10 frame averaged OCT B-scans were taken. The tear film, epithelium, Bowman's layer, stroma and posterior endothelium of the porcine eye were well resolved with the low-cost system (Figure 5.19a). The

horizontal line in the image is a common path artifact due to inaccurate background subtraction. This artifact was removed in the subsequent images of the lens and iris (Figure 5.19b) and iridocorneal angle (Figure 5.19c) of the porcine eye. The images taken from porcine tissue demonstrates the capability of the low-cost system to resolve tissue layers and structures in biological samples.

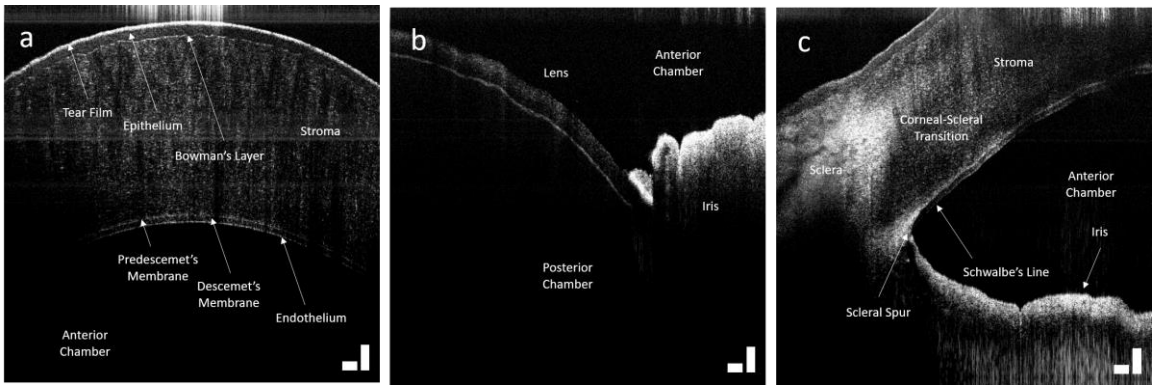

Figure 5.19. a) The OCT image of a porcine cornea, b) lens and iris and c) iridocorneal angle. The images are 10 frames averaged, and the scale bar represents 200 µm. Figure taken from [79].

For *ex vivo* murine skin imaging, the mice were first euthanized with CO_2 asphyxiation, followed by decapitation under an IACUC approved protocol. Various portions of murine skin were imaged including the ear, tail, and back. The OCT images of the skin from the murine ear showed well-defined layers including the epidermis, dermis, and underlying auricular cartilage (Figure 5.20a). In the OCT images of the tail, the hair and hair bulb could be clearly identified (Figure 5.20b), while in the images of the back skin, the hypodermis layer could be observed under the epidermis and dermis (Figure 5.20c).

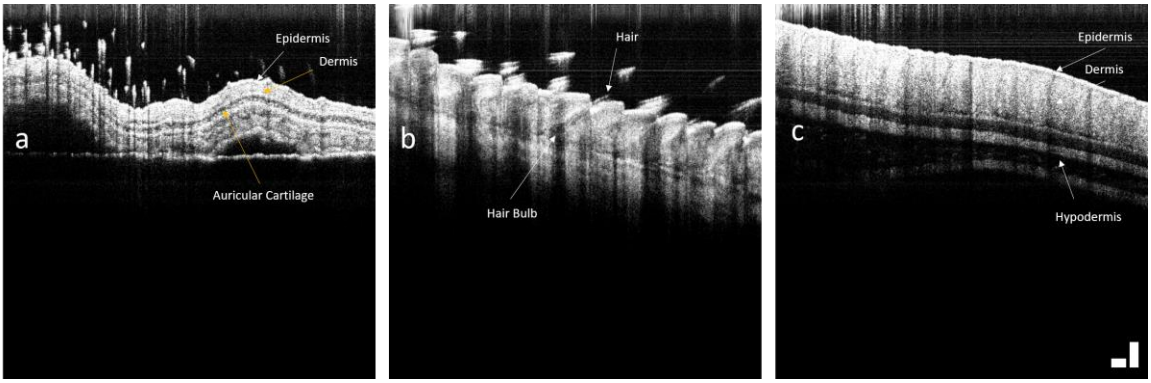

Figure 5.20. a) The OCT image of a murine ear, b) tail and c) back skin. The images are 10 frames averaged, and the scale bar represents 200 μm. Figure taken from [79].

5.5.2 In-vivo Measurement on Mice Retina Systems

For *in vivo* mice retinal imaging, a mouse retina was first modeled in Zemax prior to experimental imaging to determine the optimal collimating and focusing elements in the OCT scanner to compensate for the lens in the mouse eye. The 30 mm focusing lens in the OCT scanner was replaced with a pair of 50 mm focal length achromatic lenses, and a 6.4 μm diffraction limited spot size was achieved on the simulated mouse retina in Zemax. The scanner design allows easy exchange of the distal optic that does not require opening the scanner.

Prior to imaging the mice were anesthetized and placed beneath the OCT scanner without any direct contact. Motion artifact from breathing prevented B-scan averaging, so individual B-scans were taken for the *in vivo* retinal images. However, even without averaging, the captured B-scan image (Figure 5.21) clearly resolves the retinal layers including the retinal nerve fiber layer (RNFL), ganglion cell layer (GCL),

inner plexiform layer (IPL), inner nuclear layer (INL) outer plexiform layer (OPL), outer nuclear layer (ONL), external limiting membrane (ELM), inner segment/outer segment junction (IS-OS), retinal pigment epithelium (RPE) and optical nerve head (ONH) [80]. Because the mouse eyes were held open during experimentation and an eye drop solution was not administered for hydration, the lenses of the mouse eyes became opaque during the imaging sessions, and degradation in contrast became noticeable, as shown in the right image (Figure 5.21b).

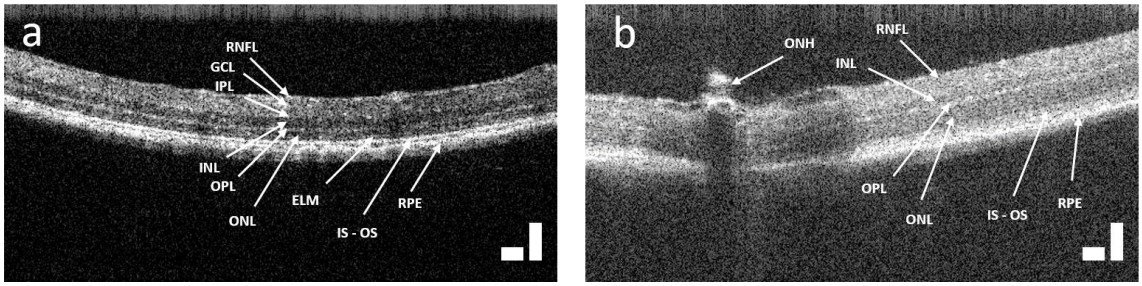

Figure 5.21. a) OCT image of a live mice retina. b) OCT image of the same mice showing the optical neve head. The image on the right has lower contrast and SNR due to the dehydration of the lens during imaging. The scale bar represents 200 μm in air. Figure taken from [79].

5.5.3 Discussion

The OCT images taken from biological samples demonstrate that the system performance is sufficient for detecting tissue layers and features that are frequently used for pathological diagnosis in ophthalmology and dermatology. Imaging the mouse retina is more difficult compared to imaging the human retina due to aberration from the lens of the mouse eye which contributes to worse imaging performance.

For clinical application, OCT has been used for monitoring the progression of age related macular degeneration (AMD) by evaluating choroidal thickness [11]. From a clinical study, the average thickness of the choroid in healthy eyes was reported to be between 272-287 μm depending on the OCT system used, while that of wet AMD and dry AMD was reported to be 194.6 μm and 213.4 μm respectively [81]. Although the mouse retinal OCT B-scan in Figure 5.21 did not detect choroidal layers, we note that retinal imaging is more difficult in mice than in humans, and thus, it is possible to image deeper in the human eye. With the 7 μm axial resolution, the low-cost OCT system could measure the difference between the choroidal thickness of healthy and AMD patients accurately, if sufficient imaging depth is achieved. Future imaging on human subjects will be performed to determine the diagnostic performance of the system.

5.6 Future Plan

The greatest limiting factor of the current low-cost system compared to other commercially available systems is the acquisition speed. After implementing the MEMS mirror scanning scheme, the final B-scan rate is limited by the acquisition speed of the line scan camera. Although the sensor is inexpensive and robust due to its tall pixel geometry, the slow line rate limits the system for certain applications. For *in vivo* retinal imaging, the motion artifacts from breathing prevented B-scan averaging. Thus, although the imaging performance of a single frame is comparable to commercially available systems due to its high bit depth, the system fails to take advantage of the

potential SNR improvement through averaging for non-stationary samples. Alternative sensors are currently under consideration to improve the B-scan frame rate. However, further reduction in price and improvement in portability are the primary goals for the next generation of the system.

There has been growing interest in miniaturizing the OCT system targeted for primary care medicine. However, most commercial OCT engines remain too bulky to be used for point-of-care diagnostics. The current low-cost OCT engine including the mini PC and the scanner weighs less than 6 lbs, but further reduction of the form factor can be achieved by developing a customized control electronic board and powering the system with an external battery. The development circuit board for the MEMS mirror, liquid lens and the camera sensor can be custom designed using a much simpler circuit board, integrating only the relevant functions for controlling the OCT system. This will contribute to both cost and size reduction, as the control boards used in the current system iteration are sold from vendors which are pricey and include extra features that are not needed for our application. In addition, the power consumption of the current system is fairly low, requiring only 14 Watts when fully operating. It would be possible to integrate a system on module (SOM) to replace the mini PC and convert the system to be fully battery powered and greatly increase the portability.

5.7 Summary

Through multiple tradeoffs, we sought to design a low-cost OCT system with a combination of components that yielded the lowest cost, yet maintained the targeted clinical level performance. The final low-cost OCT system cost under $7,200 and achieved a 5-fold cost reduction and more than 2-fold reduction in volume compared to entry level commercial OCT system. The performance of the low-cost system was carefully characterized and compared favorably to the specification of commercially available OCT systems. An axial resolution of 7 μm, and lateral resolution of 17.6 μm was achieved over a 2.8 mm imaging depth and 7 mm by 7 mm FOV. The final B-scan (512 by 512) frame rate was 12 fps which is limited by the line rate of the sensor. Most of the optical assemblies including spectrometer housing were 3D printed for an inexpensive and compact design which is optimal for point-of-care applications. Finally, imaging on biological samples demonstrates the potential of the system for future clinical application.

6. Development of Multimodal OCT and a/LCI Endoscopic Probe

In the chapter, we discuss the design and implementation of a custom imaging spectrometer that will be incorporated into a new a/LCI system that will be combined with OCT for esophageal tissue studies. The potential of OCT imaging guidance to improve a/LCI measurements has been well discussed in an earlier section 4.1 and 4.2, and combining OCT and a/LCI into a multimodal system can provide more effective tissue targeting in endoscopic applications. In addition, to further design of the combined system, a number of commercial and custom fiber bundles that could be used for light delivery and collection in a/LCI have been carefully characterized for potential inclusion in the endoscopic probe. This characterization will not only help with developing the probe design, but also provide valuable insights into the potential application of coherent bundles for general coherent imaging.

6.1 Motivation

Esophageal adenocarcinoma (EAC) is a fatal disease affecting approximately 2-3 million Americans with a mortality rate above 80% [82]. EAC is often diagnosed at an advanced stage due to the lack of early detectable symptoms of the disease. Moreover, the incidence of the EAC has been rapidly increasing due to the lack of effective screening techniques [83]. Patients with Barrett's esophagus (BE) are at higher risk of developing EAC and require periodic endoscopic examinations of the esophagus to

diagnose the presence of EAC. However, these examinations are often laborious and adherence to surveillance guidelines are relatively poor [84].

We propose to develop a more effective diagnostic tool for screening for EAC by combining a/LCI and OCT. In previous clinical studies, a/LCI successfully detected dysplasia in BE patients *in vivo* [19], but the limited of coverage area and lack of visual guidance using the a/LCI probe has limited further clinical application. On the other hand, OCT affords real time image guidance, and larger tissue area coverage [85]. Thus, we now seek to combine these two complementary modalities to provide a more comprehensive diagnostic tool for cancer screening.

6.2 Imaging Spectrometer

For the a/LCI portion of the multimodal instrument, an imaging spectrometer was designed to detect scattered light at multiple angles simultaneously. The imaging spectrometer need to image light from the new a/LCI endoscopic probe which is composed of an array of 30 single mode fibers stack across the imaging slit. The individual fiber has a diameter of 80 μm so that the stacked fiber array is about 2.4 m wide. Also, the imaging spectrometer needs to cover entire bandwidth of the a/LCI spectrum, which is typically around 50 nm wavelength [61]. In addition to the meeting the required geometrical constraints, minimization of the off-axis aberration was the primary goal in this design instead of cost reduction as with the earlier low-cost spectrometer design. The image distortion from off-axis aberration includes coma, field

curvature, and astigmatism which becomes progressively worse towards the edge of the sensor. For the line scan spectrometer in the low-cost OCT system, sagittal focus was sacrificed in order to gain more tangential focus using the tall pixel sensor. However, in the imaging spectrometer, a balance between the sagittal focus and tangential focus is necessary in order to maintain decent spectral and spatial resolution (Figure 6.1).

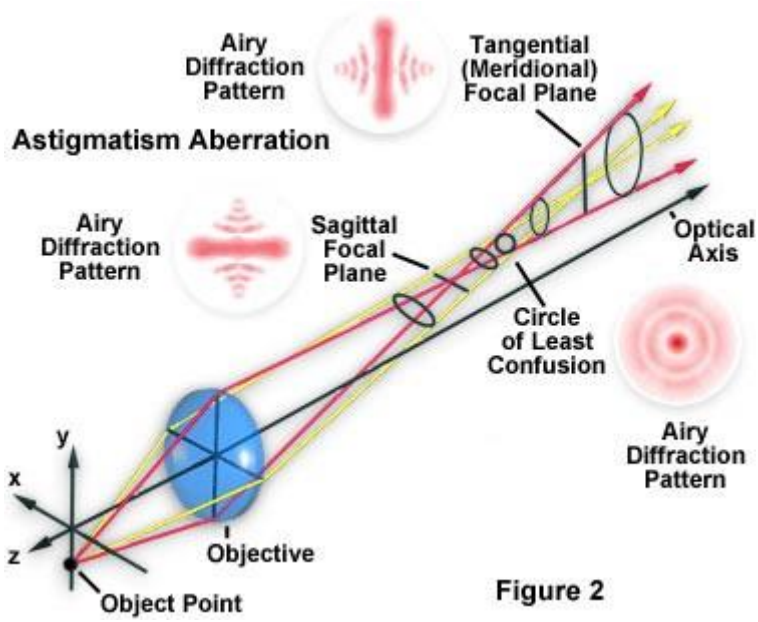

Figure 6.1. Ray diagram illustration showing tangential focus and sagittal focus. In between the tangential focal plane and sagittal focal plane, circle of least confusion exist where the image approach circular symmetry. Figure taken from [86]

6.2.1 Design and Implementation

The Czerny-Tuner spectrometer is a well-used, common spectrometer configuration due to the flexible wavelength range and compact design, and it was used in previous a/LCI systems. Czerny-Tuner spectrometers utilize two concave mirrors for collimating and focusing the light and a reflection grating in between them as shown in

Figure 6.2. The advantage of using the concave mirrors in Czerny-Tuner spectrometers is the minimization of chromatic aberration that could arise from using lenses. Therefore Czerny-Tuner spectrometer can cover large range of wavelength and wavelength range can be simply tuned by rotating the grating angle to the incident beam without changing any other optics. The problem with most manufactured Czerny-Turner spectrometers is the off-axis aberration caused by the concave mirrors and off-axis geometry. Although many types of aberrations contribute to the final imaging performance of the spectrometer, the individual contribution of each type of aberration cannot be precisely quantified without detailed specifications of the optical elements within the spectrometer. However, a simple measurement can be obtained to identify the dominant source of aberrations in the system.

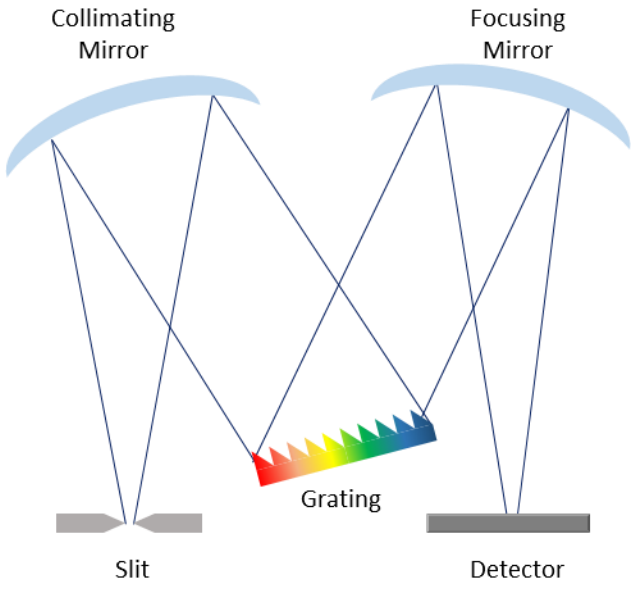

Figure 6.2. Czerny-Turner spectrometer design

Figure 6.3 shows the measured spectrum from Argon calibration lamp (Newport, 6030) using a commercial Czerny-Turner spectrometer (Princeton Instruments, SP2150) in the 2D a/LCI system. The information about the spectrometer and sensor are previously described in section 3.2.2. Briefly, the imaging spectrometer has 150 mm focal length and have 600 lines/mm reflective grating. With a 640 by 480 pixel CCD array (Pike F-032, AVT) with 7.4 μm square pixel the imaging spectrometer covers 41 nm across the 640 pixel axis and has 3.5 mm of imaging height across the short dimension.

A vertical yellow reference line (along the spatial dimension) at 794 nm was added for visual comparison in Figure 6.3. From the spectra, a curvature was observed in the spectral peaks along the spatial dimension with blur along the spectral dimension. The curvature of the lines is likely due to barrel distortion, while the blurring in the spectral lines at the edge of the image is likely due to coma aberration (Figure 6.3b).

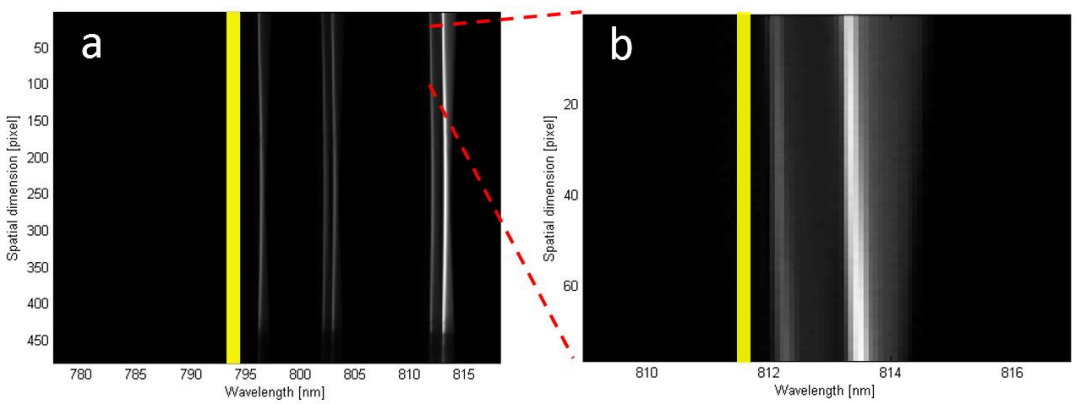

Figure 6.3. a) Argon calibration source measurement with false colored yellow line at 794 nm. b) Zoomed in image showing the aberration with false colored yellow line near 812 nm.

When light from a broadband source was filtered through a pinhole and measured with an imaging spectrometer, a horizontal line along the spectral dimension is expected in the image. However, blurring in the spatial (vertical) dimension at the edge of the image creates a bow tie effect as shown in Figure 6.4.

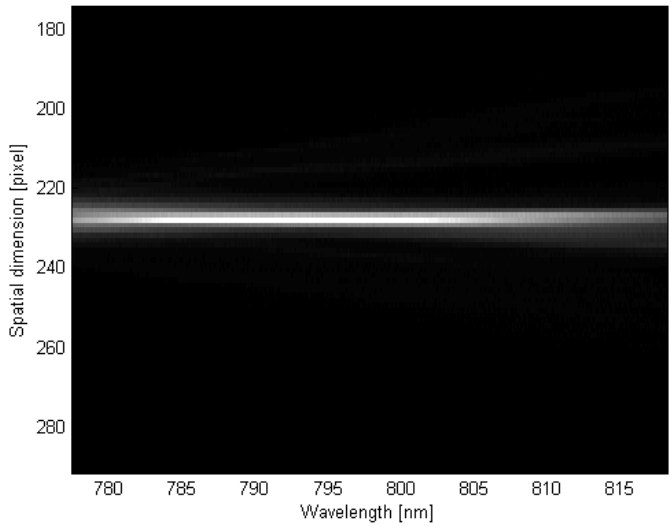

Figure 6.4. Measured spectrum of broadband light emerging from a pinhole.

Although the size of the detector (4.7 mm wide by 3.6 mm high) is much smaller than the focal plane size defined by the manufacturer (25 mm wide by 10 mm high), from these images, it is readily seen that off-axis aberrations are the dominant aberrations degrading both the spatial and spectral resolution of the imaging spectrometer. These aberrations largely arise because the spectrometers are designed to cover a large wavelength range with a tunable center wavelength. The center wavelength of the spectrometer is easily tuned by rotating the diffraction grating in the system, and the wavelength range can also be easily changed by changing the grating

pitch (lines/mm) with some minor alignment. In order to support a large wavelength range, the spectrometer uses mirrors for the collimating and focusing optics (See Figure 6.2) to avoid chromatic aberration. This design is made more compact using fold mirrors to create an off-axis optical setup; however, this also results in the undesired off-axis aberrations.

For the new a/LCI spectrometer, I wanted to trade off the simplicity of the spectrometer system and sacrifice the tunable wavelength range to reduce the aberrations and improve imaging performance. A typical a/LCI system uses a relatively narrow bandwidth light source (~50 nm) with a set center wavelength. For such a limited wavelength range, the concave mirrors in the spectrograph contribute most of the off-axis aberrations as well as spherical aberration. By replacing these elements with lenses designed for the chosen wavelength range, these aberrations can be reduced. There is some expense of added chromatic aberration and ghosting artifacts from unwanted reflections from the surface of the lenses. Also, the spectrometer system cannot be designed to be as compact as the Czerny–Turner design.

For the diffraction grating, a volume holographic transmission grating was chosen since it provides more diffraction efficiency than a reflective grating at high spatial groove frequency. The main advantage of using a transmission grating over reflective grating is a higher throughput in the system. However, this comes at a higher

cost, because reflective gratings are mass produced and therefore traditionally cheaper than transmission gratings.

A simulation was performed to determine the optimal optical elements for the new spectrometer design. The input parameters are the wavelength range, the center wavelength, the detector size and the number of detector pixels. The center wavelength (λ_c) is 830 nm and wavelength range $\Delta\lambda$ is 60 nm. A number of detector candidate were considered to meet the design goal. First, the dimension of a detector must be larger than the dimension of the a/LCI probe to capture light across 30 fiber, assuming unit magnification. Also, preferred size of pixel was under 10 μm so that performance of the spectrometer is limited by optical resolution rather than the size of the camera pixel. The selected detector (FLIR, GS3-U3-23S6M-C) which has 1920 by 1200 pixels with a 5.86 μm pixel size offered additional advantage in high quantum ratio near 830 nm (~20%) and higher frame rate (163 fps) and dynamic range (72 dB) among the considered sensors. The longer detector dimension (11.136 mm) corresponds to the spectral dimension while the shorter dimension (6.96 mm) corresponds to the spatial dimension. The ideal optical resolution for a 60 nm wavelength range spreading out equally over 1920 pixels would be 0.031 nm per pixel. For the grating, the only available gratings at the targeted wavelength were 1200 and 1500 line pairs per millimeter (lp/mm) gratings which offered a sufficiently large physical dimension to receive light from a 1 inch collimated beam.

The 1 inch collimated beam would offer smaller diffraction limited spot compared to half inch collimated beam. The diffraction limited spot size can be calculated by [87]

$$\rho = 1.22\lambda\frac{f}{D} \tag{6.1}$$

Where ρ is radius of focused spot, λ is wavelength, f is focal length and D is diameter of lens aperture. For given wavelength, shorter focal length and larger aperture would be desirable in order to achieve a smaller spot size. Also, a large grating would offer higher throughput without cutting the beam and would also more freedom on focal length selection for collimating lens. The greater the groove density, the larger the diffraction angle separation exists between wavelengths, resulting in higher optical resolution at the cost of lower detectable spectral range. With a set detector size and target wavelength range, a greater groove density grating would require a shorter focal length due to larger angular separation. A 1500 lp/mm grating was selected over 1200 lp/mm grating for the system design to utilize a shorter focal length focusing lenses in an effort to reduce the size of the spectrometer and produce a tighter spot size at the detector.

Once the initial inputs were set, the geometry of the system was determined. First, the angle of incidence was calculated. In transmission mode, the Littrow configuration with -1 order is most often used to optimize diffraction efficiency. In this configuration, the incidence angle on the grating is equal to the diffraction angle in magnitude but opposite in sign. The incidence angle can be determined by the following equation [88],

$$\alpha = sin^{-1}\left(\frac{\lambda_c G}{2cos(\Phi/2)}\right) - \frac{\Phi}{2} \tag{6.2}$$

where α is the incidence angle, φ is the sum of incidence angle and diffracted angle (0 in the Littrow configuration), λ_c is the center wavelength, and G is grating groove density. With 830 nm center wavelength, and a 1500 lp/mm groove density, the optimal incidence angle is calculated to be 38.5°. Next, the focal length of the focusing lens can be determined by

$$L_F = \frac{L_D cos(\beta)}{G\Delta\lambda} \quad . \tag{6.3}$$

Given the detector width (L_D) of 11.136 mm, the focal length (L_F) of the focusing lens is calculated to be 96.8 mm.

Upon determining the transmission grating and detector, the only elements left for optimization were the collimating and focusing lenses. Multiple off-the-shelf lens combinations were considered to find the pair that achieves optimal performance that provides minimum spot size across the entire focal plane with minimal off axis aberration. Since the focal length of the focusing lens is supposed to be around 97 mm as calculated using equation 6.3 to cover desired wavelength range with given detector and grating combination, the collimating lens also needs to have a similar focal length range in order for the system to have unity magnification. However, the beam size is limited by the projected area of the grating determined by the dimension of the grating and the

incidence angle. With a 24 mm by 24 mm grating, and a 38.5° incidence angle, width of the projected area is calculated to be 18.8 mm by simply multiplying the width of grating by cosine of the incidence angle (Figure 6.5). The collimated beam from a single mode fiber (NA = 0.13) at the entrance slit must remain under 19 mm in diameter to prevent clipping of the beam. However, considering the height of the fiber array at the entrance slit (~2.4 mm), the beam waist must remain under 16 mm. In addition, if height of the object at the entrance slit is as tall as the height of the sensor at the detector plane (6.96 mm), 12 mm beam size would be the limit for lossless light throughput for the beam entering the slit near the edge of the slit. The diameter of the collimated beam after a collimating lens was simulated to be 13.4 mm and 18.2 mm for a collimating lens with 75 mm focal length and 100 mm focal length respectively. Therefore, a 75 mm focal length achromatic lens was used as the collimating lens instead of 100 mm focal length lens to reduce the beam diameter.

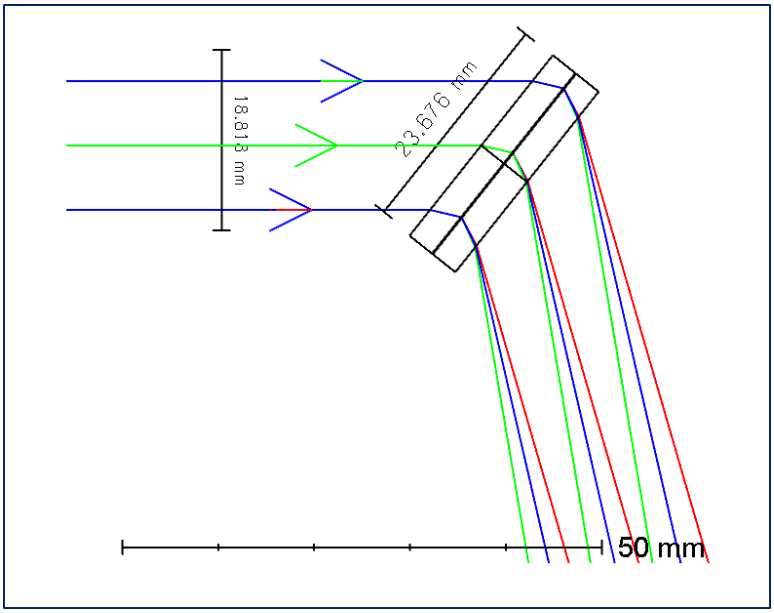

Figure 6.5. Diagram showing the collimated beam diameter and projected area of the grating in the spectrometer.

For the focusing lens, a three lens system with an effective focal length of approximately 100 mm was designed. By using a three lens design, spherical aberration can be reduced by splitting the refracting power among multiple surfaces. Multiple combinations of the lenses from off the shelf vendors were tested in optical design software (Zemax, OpticStudio 16) simulation. The general approach to assemble the lens design was to place two identical achromatic lenses back to back in a symmetric configuration. The symmetric lens configuration eliminates odd-order aberrations such as coma, transverse color, or distortion. Finally, a plano-convex lens was used as the final element to reduce the spherical aberration from the other lenses in the system.

The spot size at the detector plane and Seidal coefficients were the main considerations when optimizing the spectrometer design. The final system design in

Zemax, Seidal diagram for third-order aberrations, and Seidal coefficients summary are shown in Figure 6.6. Astigmatism and coma are no longer the dominant aberrations, and with this design spherical aberration is the largest contributor to the wavefront error.

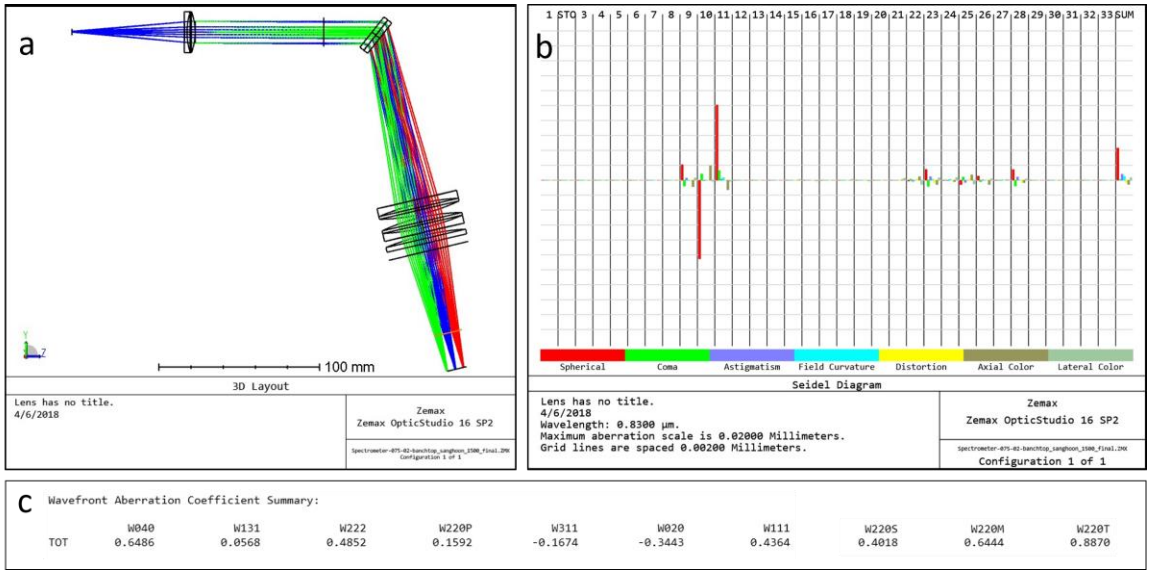

Figure 6.6. a) Zemax schematic of the imaging spectrometer, b) Seidal diagram and c) Seidal coefficient summary.

In addition, to minimize the wave front error, the mean spot size across the entire detector area was optimized instead of optimizing only for the on-axis center spot size. The input of the spectrometer for endoscopic a/LCI applications will be a linear stack of single mode fibers with approximately 80 µm separation between individual fibers. This allows greater tolerance along the spatial dimension in the design since the light from each fiber is spatially separated at the entrance plane, and at the detector plane as well. This gap between the light from individual fiber would act as a bumper to prevent overlap of the light from adjacent fiber. Thus, aberration along the spatial dimension at

the detector was preferred over degradation of spectral resolution. Simulated spot diagrams at 800 nm, 830 nm, and 860 nm are shown in Figure 6.7. The spot size remains under 2 camera pixels wide for ranges up to 0.5 mm from the center of the slit height, and remains under 3 pixels wide up to the full 1 mm slit height. At 2 mm away from the center of the slit, the enlargement of the spot size is noticeable; however, the beam is elongated along the spatial dimension as intended.

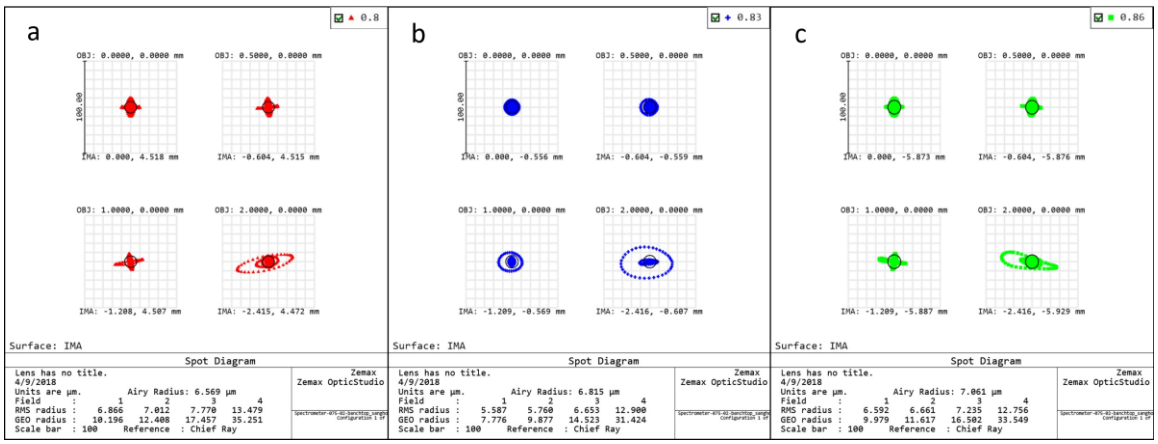

Figure 6.7. Zemax spot diagram of the imaging spectrometer (a) at 800 nm, (b) at 830 nm and (c) at 860 nm for different object height.

6.2.2 Performance Characterization

The spectrometer was assembled on a benchtop following the simulated design to be characterized before finalizing the housing. The spectrometer covers a wavelength range from 797.8 nm to 861.2 nm, reaching the targeted wavelength range of 60 nm. When light from a broadband source was passed through a single mode fiber and imaged by the spectrometer, the measured spectral line no longer shows barrel distortion or the “bow-tie” effect on the edge of the spectrum (Figure 6.8a). The reduced

aberration is noticeable compared to the same measurement with the manufactured spectrometer (Figure 6.4), and the FWHM spot size across the spectrum was measured to be 9.2 μm which corresponds to about 1.5 pixel. (Figure 6.8b).

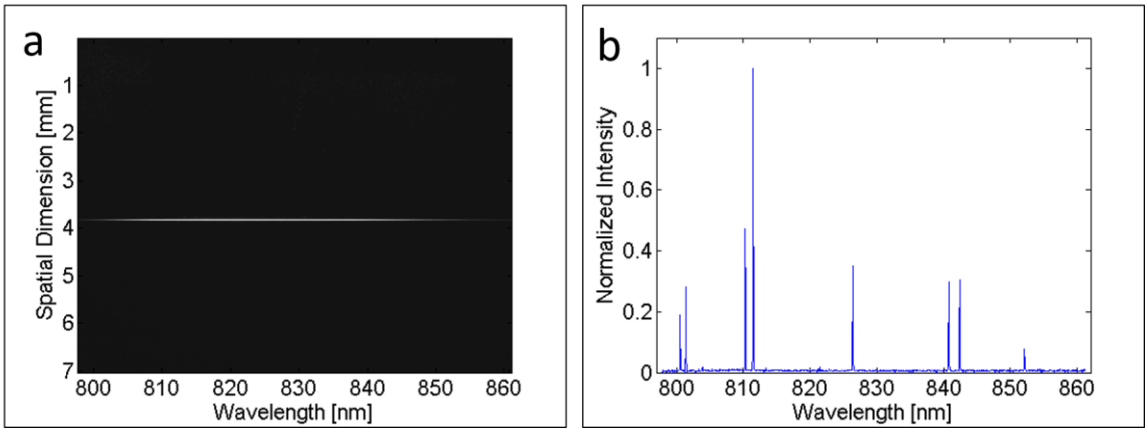

Figure 6.8. a) Image of broadband light emerging from a single mode fiber and b) argon calibration source measurement.

In order to mimic the single mode fiber array that will be used for the a/LCI probe, a single mode fiber was mounted on a XY translational control stage to characterize the spectrometer performance at multiple positions in the entrance slit plane. Light from single mode fiber at the entrance slit was moved in a couple hundred micron increments with the translational stage to test the performance of the spectrometer across entire detector plane. The magnification of the system was measured to be 1.18. Next, an argon calibration source was coupled into the fiber, and the translation stage was incrementally shifted to measure the corresponding FWHM spot size across the detector (Table 6.1). Although the camera sensor seems to be tilted away from the focal plane so that spot sizes are skewed at one end of the spectrum, the

FWHM spot size remained under 20 μm over the 2 mm imaging FOV. With proper alignment, the spectrometer should be able to achieve under 15 μm spot sizes within a ±2 mm FOV. The a/LCI fiber probe, comprised of a single mode fiber array, and the 3D printed housing of the spectrometer are under development.

Table 6.1. FWHM spot size measurement (in μm) for different locations of the beam entrance height at the entrance slit.

Wavelength / Location [mm]	800.60 nm	810.4 nm	826.5 nm	842.5 nm
Center	9.16	10.4	15.4	19.1
100	9.6	9.4	13.1	18.4
200	12.9	9.5	14.7	19.6
300	10.2	11.6	14.6	21.5
500	9.7	10.2	12.1	19.2
1,000	12.1	9.8	13.0	17.6
1,500	10.0	9.7	14.0	15.3
2,000	14.2	14.0	12.8	13.3

6.3 Fiber Bundles for a/LCI endoscopic probe

The previous clinical a/LCI instrument collected the angularly scattered light from the tissue using a coherent leached fiber image bundle (Schott). The fibers in this bundle were multimode at the wavelength used (840 nm +/- 20 nm). The fiber would be multimode if the wavelength of the light source is shorter than the cutoff frequency of the fiber [89]. With a multimode fiber, higher order modes can propagate into the fiber, and higher modes will also interfere with other modes as well as the fundamental mode. This will create unwanted ghost image on top of fundamental mode interference. In order to separate the ghost images generated by the higher modes, a sufficiently long

probe design was adopted. Xie et al. performed OCT imaging through a similar fiber bundle and used a sufficiently long fiber bundle in order to separate the fundamental mode image and the ghost images produced by additional modes [90].

However, this design is relatively inefficient due to the high cost of the leached fiber bundle and the reduction in the dynamic range of the detector and the SNR of the system from the collection of light propagating in the unused higher order modes. In addition, there was a slight mismatch between the lengths of each fiber within the fiber bundle so that a post processing step for registering each individual OCT A-scan was required (Figure 6.9).

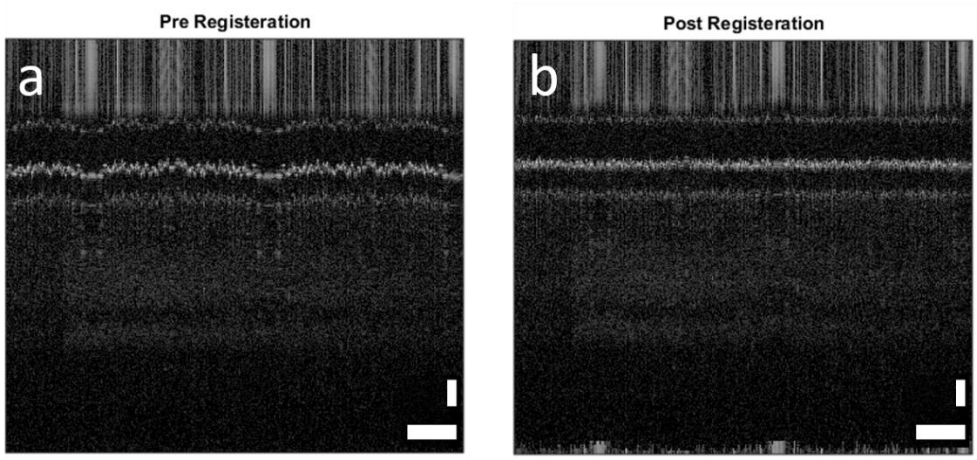

Figure 6.9. a) OCT image of a coverslip glass on a mirror prior to registration. b) Registered image of a). The fiber had core size of 7.4 μm with about 3,500 elements, but the fiber is multimode (V number ~4) near 830 nm wavelength. The bar indicates 100μm.

For the new a/LCI endoscopic probe, alternatives to the leached fiber bundle have been investigated. Imaging bundles consist of thousands of cylindrical waveguides within a small form factor and have 1:1 mapping from distal to proximal end for each

element. These imaging bundles have potential to improve the current coherence imaging technology by simplifying scanning optics. With the fiber geometry, the scanning optics can be placed near proximal end instead of distal end for endoscopic application and no moving parts as well as no driving current would be required within the endoscope [90]. This includes OCT and 2D a/LCI which rely on bulky scanning optics to cover large FOV. Toward this goal, various imagining fiber bundles from different vendors have been characterized and this study will provide useful insight on the feasibility and limitation of imaging fiber bundles for general coherence imaging.

6.3.1 Fiber Bundle Characterization

For this study, various types of fiber bundle were considered. A single mode fiber bundle would be ideal to prevent modal overlap. However, a single mode fiber bundle is not typically available without customization. In total, three types of commercially available imaging fiber bundles were characterized along with three customized imaging fiber bundles. The commercial bundles selected were FIGH-10-500N and FIGH-10-350S from Fujikura, and IGN-05/10 from Sumitomo. Wurster et al. recently demonstrated potential use of similar fiber bundles from Fujikura (FIGH-40-920G and FIGR-10) for endoscopic OCT application [91]. Although Fujikura FIGR series offer smaller numerical aperture, the fibers were no longer commercially available. The selected fiber bundles are composed of 10,000 elements with germanium-doped silica cores with a fluorine-doped cladding. The outer diameter was 450 μm for the Sumitomo

bundle, 460 μm for the Fujikura FIGH-10-500N, and 360 μm for the Fujikura FIGH-10-350S. Both of the Fujikura bundles had the NA of 0.39, and the NA of the Sumitomo bundle was 0.35 [92]. The commercial fibers are cheap (~$25/ft) and available at any length.

Three semi-custom rigid fiber bundles from Collimated Holes were considered. The available off-the-shelf fiber bundle from the vendor had an 8.6 μm core size, with 11 μm center to center spacing and 250 mm length. The bundle inherently has less flexibility and greater fragility with a V number around 21, which results in too many ghost images. V number is a fiber parameter that is directly proportional to size of a core and numerical aperture of a fiber, but inversely proportional to the wavelength of propagating light [87]. V number governs number of possible modes propagating within a fiber. For example, in order to be a single mode fiber, V number must be less than 2.405. However, since the fiber bundle can be custom ordered, a single mode fiber bundle can be designed which will only support the fundamental mode with any length of fiber. The custom bundles were drawn with K5 core and N16B cladding borosilicate glasses and an extramural absorbing glass was inserted between elements to reduce the cross talk between the adjacent fibers. Extramural absorbing glass is an opaque glass that is inserted into fiber matrix in order to eliminate stray light [93]. The three fiber bundles were drawn with the same material and geometry but different core sizes of 4.5 μm, 4.7 μm and 5.0 μm.

To characterize the selected fibers, first, the geometrical parameters were measured using an inverted microscope (Zeiss, Axiovert 200) with a 40x objective. The back end of each fiber was illuminated and images of the front face were captured with a camera with a 4.8 μm pixel size (Flea3, PointGrey). The imaged fiber bundle faces are shown in Figure 6.10.

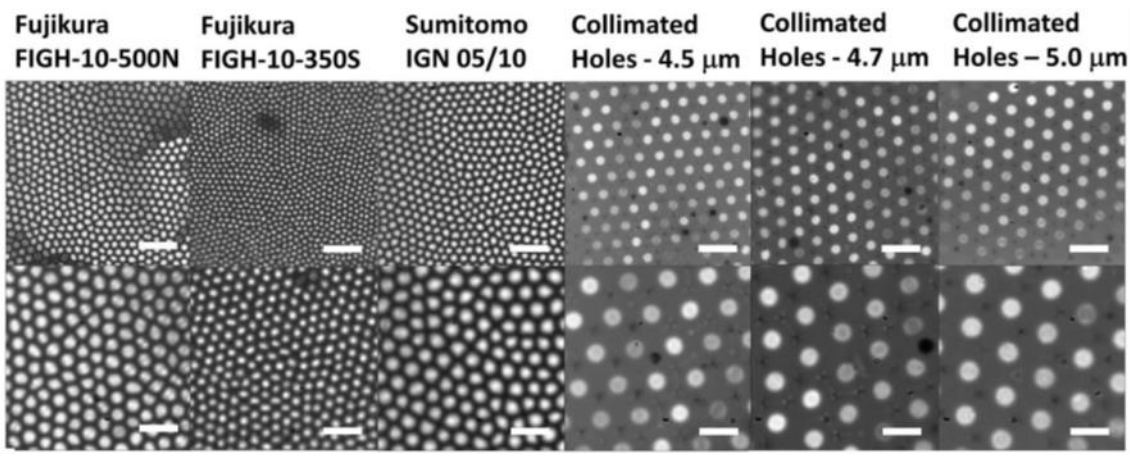

Figure 6.10. The microscope image of the fiber bundle face for the three commercial bundles and the custom fiber bundles. Figure taken from [94].

With the microscope images, the effective core diameter (ECD), core to core spacing (CCS) and open area ratio (OAR) were measured for N = 20 cores each. The measured ECDs were 2.46 ± 0.17 μm for FIGH-10-500N, 1.70 ± 0.11 μm for FIGH-10-350S, and 2.66 ± 0.19 μm for IGN-05/10. For the fiber bundles from Collimated Holes (Campbell, California), the measured diameters closely matched the nominal diameters with an average measurement of 4.51 ± 0.13 μm, 4.67 ± 0.13 μm and 5.09 ± 0.11 μm. The commercially available bundles have a higher variation in core size compared to the custom bundles. The CCS were measured to be 4.63 ± 0.36 μm for FIGH-10-500N, 3.37 ±

0.30 μm for FIGH-10-350S, and 4.60 ± 0.26 μm for IGN-05/10. The custom bundles had a larger CCS compared to the commercial bundles, with 10.08 ± 0.16 μm, 10.63 ± 0.20 μm, and 11.46 ± 0.12 μm for the 4.5, 4.7, and 5.0 μm core bundles respectively. Due to the larger CCS of the custom bundles, the custom bundles had larger OAR (0.15 – 0.16 for all three bundles) compared to the commercial bundles. The measured OAR of the commercial bundles were 0.31 for FIGH-10-500N, 0.21 for FIGH-10350S, and 0.25 for IGN-05/10. These results are summarized in Table 6.2.

Table 6.2. The effective core diameter (ECD), core to core spacing (CCS) and open area ratio (OAR) calculation for the three commercial fiber bundles and custom fiber bundles.

	FIGH-10-500N	FIGH-10-350S	IGN-05/10	C.H. (4.5 μm)	C.H. + (4.7 μm)	C.H. (5.0 μm)
ECD (μm)	2.46 ± 0.17	1.70 ± 0.11	2.66 ± 0.19	4.51 ± 0.16	4.67 ± 0.13	5.09 ± 0.11
CCS (μm)	4.63 ± 0.36	3.37 ± 0.30	4.60 ± 0.26	10.08 ± 0.16	10.63 ± 0.20	11.46 ± 0.12
OAR	0.31	0.21	0.25	0.16	0.15	0.16

6.3.2 OCT Imaging through Fiber Bundle

To investigate the modal structure of the fiber bundles, they were used for OCT imaging by scanning a focused beam across the proximal end and placing a test sample at the distal end. To implement this scheme, the scanning optics needed to be modified to match the size and numerical aperture of each fiber sample to maximize the throughput of the system. This will also improve the lateral resolution of the OCT imaging which is determined by both size of the fiber core and spot size at the fiber face. The low-cost OCT system described in chapter 5 was modified with a chromatically

corrected 10x objective lens (Zeiss EC Plan NEOFLURAR, NA = 0.3). The measured spot size was 2.1 μm, smaller than the core diameter of the all fibers studied here except the FIGH-10-350S. Prior to the OCT B-scan acquisition, the scanning of the beam across the fiber bundle was imaged with a camera located at the distal end of the bundle. All the fiber bundles used for the study were 300 mm in length and mounted on V-groove fiber holders on both ends. The commercial bundle suffered from severe crosstalk among individual fibers (Figure 6.11A-C), and the light propagation was not confined to the illuminated fibers, resulting in spectral overlap between neighboring channels. The coherent cross talk between individual fibers is not acceptable in coherent imaging. On the other hand, the custom bundles showed a promising scanning pattern where there is no leakage of light to the neighboring element as shown in Figure 6.11D-F.

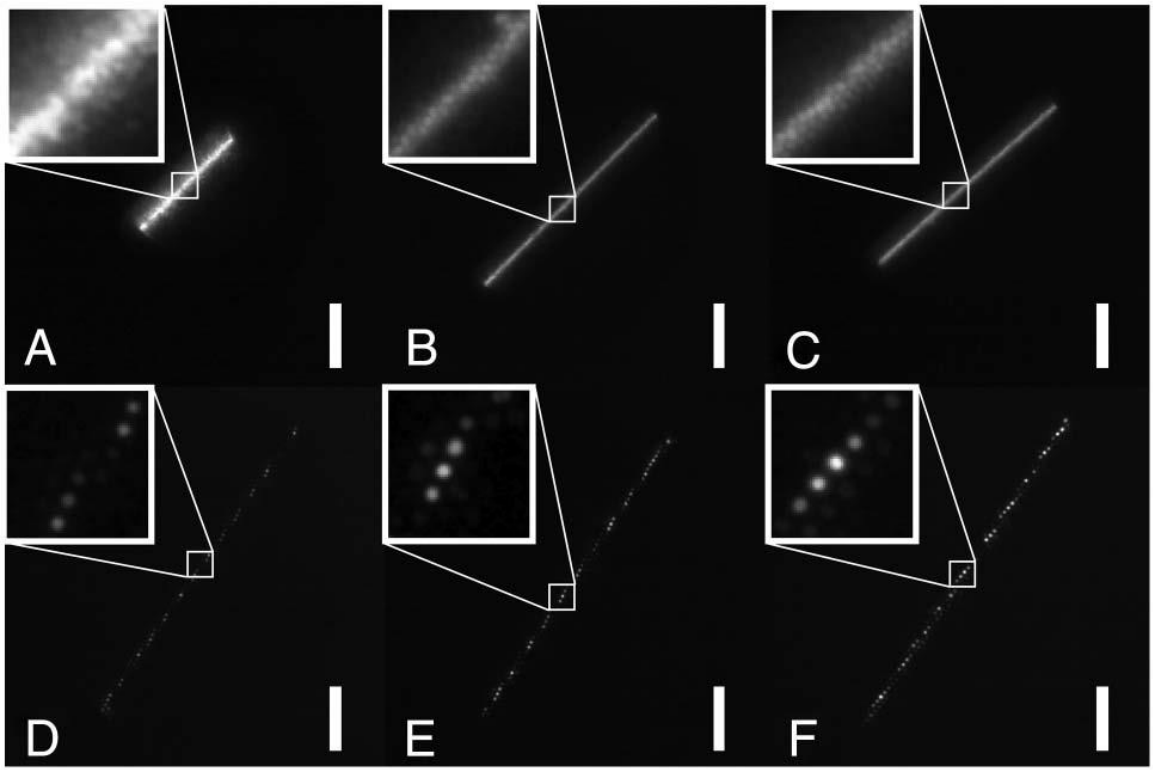

Figure 6.11. Scanning pattern captured at the distal end of the fiber bundles. A) FIGH-10-350S, B) FIGH-10-500N, C) IGN-05/10 and D-F) Collimated Holes bundles with 4.5, 4.7 and 5.0 μm diameter. The scale bar represents 100 μm. Figure taken from [94].

After confirming the illumination beam was tightly focused on the proximal end of the fiber bundle, the reference arm was path matched to the sample arm in order to implement OCT imaging in a B-scan across the fiber. The reflection from the distal end of each fiber was used as the sample light to generate the OCT images (Figure 6.12). There was noticeable optical path length (OPL) variability among the fiber elements for the commercial bundles which was worse than the Schott leached bundles. The inter-element OPL variability was more noticeable for the smaller core sized bundle (FIGH-10-350S), and the fiber bundle exhibited broad dispersion variability that could not be

numerically compensated for all elements at once. The bundles with larger cores showed less OPL and dispersion variability but the fiber bundle would still require pre-calibration, and post image registration to generate a useful OCT B-scan. The Collimated Holes bundles did not suffer from the mismatch in OPL among individual fiber elements but ghost images were visible for the bundles with 4.7 and 5.0 μm diameter cores. Surprisingly, the ghost images were absent for the bundle with 4.5 μm cores, meaning the 4.5 μm core diameter bundle is effectively single mode. However, diminishing tails appeared below the interference for all the custom fibers which suggests the fibers will degrade the axial resolution of the OCT images. The diffuse tail effect on the custom fibers are likely the result of the light leaking into the cladding although extramural absorbing glass was inserted to absorb the stray light. In order to attenuate the light travelling through the fiber cladding, a stronger or thicker absorbing material can be used. Also, a longer fiber would provide more attenuation of the stray light in the cladding than a short fiber. The diffuse tail effect is further investigated along with the modal structure of the Collimated Holes fiber bundle.

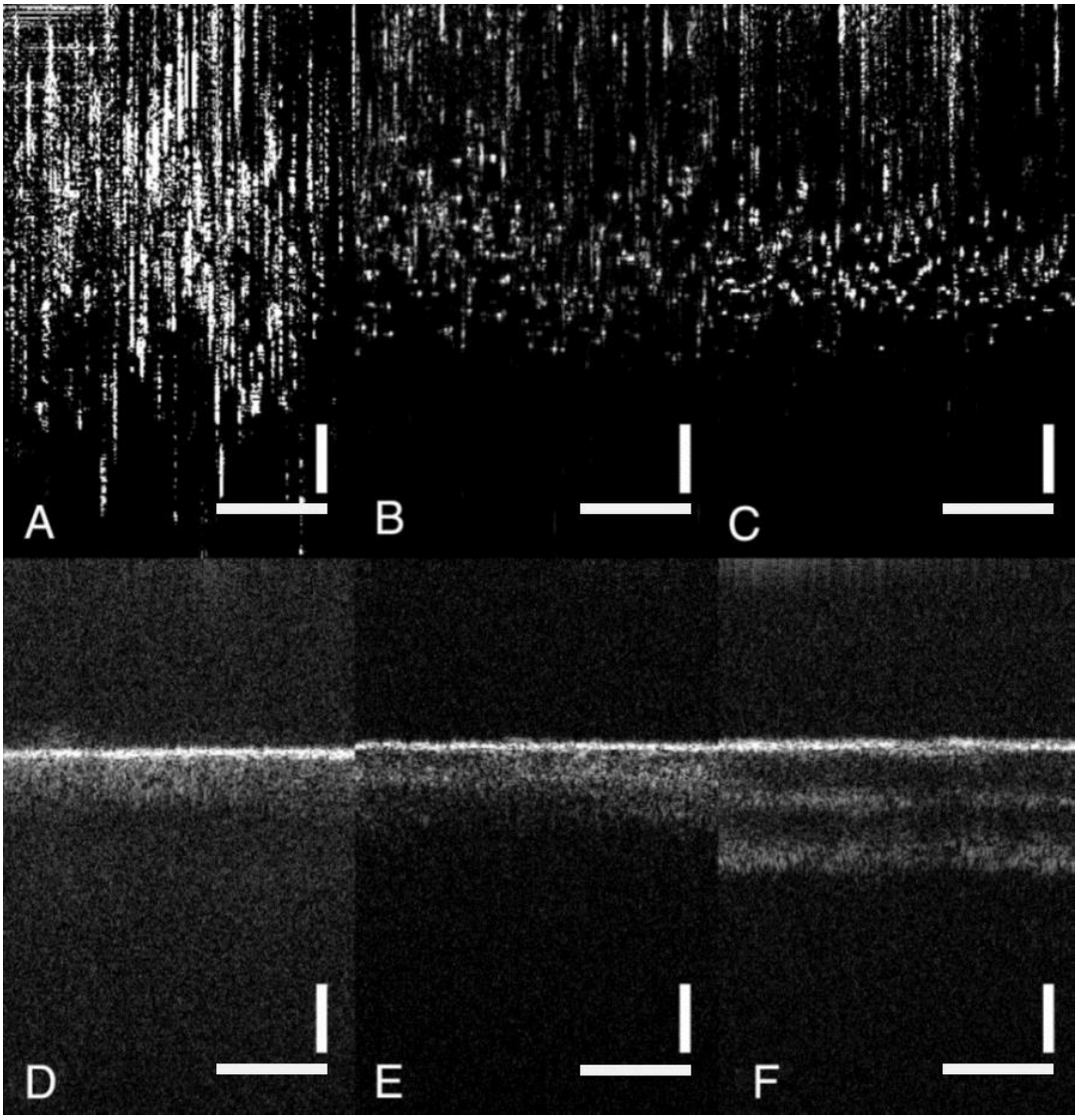

Figure 6.12. The OCT scan of a distal end of the fiber bundles (10 frames averaged). A) FIGH-10-350S, B) FIGH-10-500N, C) IGN-05/10 and D-F) Collimated Holes bundles with 4.5, 4.7 and 5.0 μm diameter. The vertical scale bar represents 200 μm and the horizontal scale bar represents 100 μm. Note the OPL variability among the fiber elements for the commercial bundles. The inter-element OPL variability was more severe for the smaller core sized bundle compared to the larger core bundles. Collimated Holes bundles did not suffer from the OPL mismatch among individual fiber, but ghost images were visible for the bundles with 4.7 and 5.0 μm diameter cores. However, the ghost images were absent for the bundle with 4.5 μm cores, meaning the 4.5 μm core diameter bundle is effectively single mode. Figure taken from [94].

The mode structure of the Collimated Holes bundles was further investigated using different lengths and core sizes. All the tested fibers were manually angle polished so that back reflection from the fiber face is not detected and thus does not reduce the dynamic range of the measurement. First, in order to confirm that the 5.0 μm core sized bundle propagates higher order modes, a mirror was imaged using the OCT system for both a 12.5 mm and 25 mm length of the bundle (Figure 6.13). As anticipated for multimode fibers, ghost images were observed from interference generated with the higher order modes with an increasing separation between modes as the modal OPL variation increased for the longer length fiber bundle.

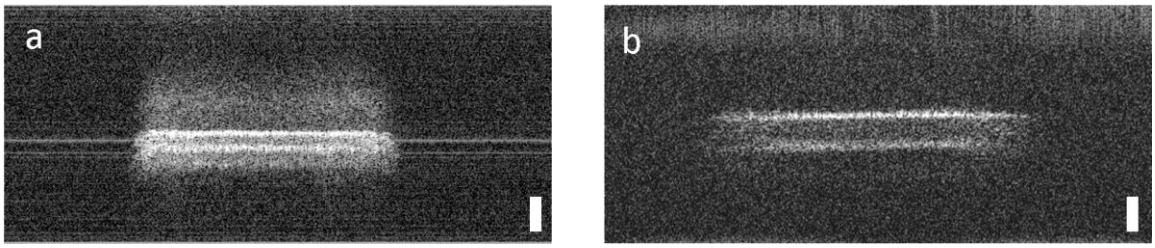

Figure 6.13. The OCT scan of a mirror using the 5 μm core sized Collimated Holes bundles at a) 12.5 mm and b) 25 mm fiber length. The scale bar is 200 μm.

Next, we received a sample of 3.2 μm core sized fiber bundle. It was expected that the smaller core sized bundle will reduce the diffuse tail which was observed following a strong interference peak in the OCT image. However, the image of the scanning beam captured at the distal end of fiber suffered from severe leakage and crosstalk compared to the 5.0 μm core sized bundle (Figure 6.14). The spread of the light at the distal end for 3.2 μm bundle was even worse than the commercially available

bundle. The core size might be too small for the mode radius, and most of the power is delivered to the adjacent cladding rather than confined within the targeted core.

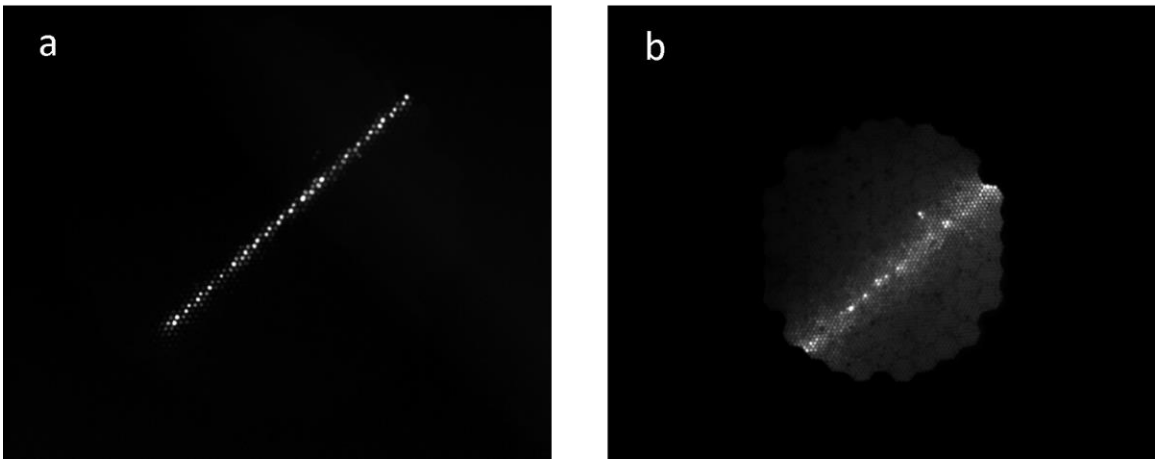

Figure 6.14. Scanning pattern captured at the distal end of the fiber bundles for a) 5 μm sized core, and b) 3.2 μm sized core.

Lastly, length dependence of the diffuse tail for the 4.5 μm bundle was investigated. A 65 mm and 250 mm length of 5 μm core bundles were angle polished and used for imaging a mirror (Figure 6.15). The diffuse tail elongated noticeably for the 65 mm bundle while the 250 mm bundle showed much less of the effect. The longer length of the fiber helps to eliminate detection of light leaked into the cladding modes, thus reducing the tail artifact. Although significant amount of the tail effect has been subdued with the longer fiber bundle, a more absorbing layer or a longer fiber bundle would be necessary to further reduce the diffuse artifact sufficiently for OCT imaging applications.

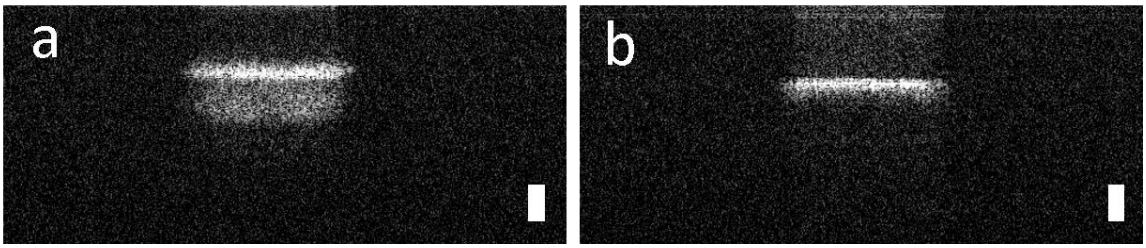

Figure 6.15. The OCT scan of a mirror using the 4.5 μm core sized Collimated Holes bundles with a) 65 mm length and b) 250 mm length. The scale bar represents 200 μm.

6.4 Summary

For simultaneous a/LCI acquisition of angularly scattered light, a custom spectrometer has been designed and implemented. The custom imaging spectrometer is designed to reduce off-axis aberration that dominates the spectrometer performance. The off-axis aberration has been corrected by using transmission optics instead of reflective optics that are corrected for the specific wavelength of interest. The performance of the first version of the imaging spectrometer has been characterized, and the design target was achieved. The FWHM spot size remained under 20 μm over the 2 mm imaging FOV with 1.2 magnification.

In order to investigate a possible a/LCI probe improvement from the previous version, multiple fiber bundles from commercially available vendors and custom fiber bundles were examined. The geometrical parameters have been measured for the fibers, and the mode structure has been investigated for coherent imagining. Most of the commercial bundles suffer severely from crosstalk between fiber elements. On the other hand, the crosstalk was only present for the small core sized bundle (3.2 μm core size)

for the custom drawn fiber bundles. The multimode behavior of the 5.0 μm core sized bundle and single mode characteristic of the 4.5 μm core sized bundle have been confirmed through OCT imaging of a mirror. Although the 4.5 μm bundle showed potential to be used as single mode fiber bundle, the diffuse tail artifact still remained as an obstacle for coherent imaging. For the future study, these fibers will be tested with a 1,300 nm OCT system instead of 800 nm to investigate their potential application as single mode imagining bundles at higher wavelength.

7. Conclusions

The work presented in this dissertation describes the development of multimodal light scattering techniques using optical coherence tomography (OCT) to improve clinical diagnosis. This includes the development of a multimodal system that combines 2D a/LCI and OCT to provide more effective light scattering analysis with a/LCI measurement. The multimodal system has shown promising advancement for the a/LCI technique, and the combined system will be integrated into an endoscopic probe in the future to detect dysplasia in Barrett's esophagus in a clinical trial. In addition, the development of low-cost, portable OCT were presented. The performance of the system has been characterized by measuring optical parameters such as the power throughput, and lateral resolution. These compared favorably to currently available commercial OCT systems. The low-cost OCT system will provide more opportunities for OCT guided diagnosis in a variety of clinical application.

The first aim presented the development of a multimodal system that combines 2D a/LCI and OCT to provide a unique analysis of sample structure that cannot be obtained using a single modality. In order to demonstrate the utility of the combined system, a scattering phantom was fabricated via soft lithography. The following aim presents examples of combined a/LCI measurements and OCT imaging on *ex vivo* tissue samples to demonstrate the utility of correlation measurements using the combined imaging system. Using the multimodal system, the rejection of improperly oriented

tissue sites were demonstrated. In addition to nuclear size determination, power law fitting analysis was demonstrated for long range correlation analysis. With the power law fitting analysis, the comparison of the normal versus diseased retinal tissue revealed significant differences in morphology, and quantitative biomarkers were determined that could be used in future studies.

The third aim describes the development of a comprehensive low-cost OCT system under $7,200 for the components including a PC, light source, customized spectrometer, and 3D printed mechanical parts. The capability of the system was demonstrated by imaging an *ex vivo* porcine eye and an *in vivo* mouse retina, as well as murine skin. In the future, further optimization and customization can be pursued to reduce the total cost of the system while also increasing functionality and portability. The form factor can be further reduced by developing customized control electronics and integrating battery power. For example, the controller boards for the MEMS mirror and liquid lens can be custom designed using a much simpler electronic circuit board, which will both contribute to further cost reduction and potentially battery powered system. Future imaging work will be performed to evaluate the diagnostic performance of the low-cost OCT system for *in vivo* human retinal imaging.

In the fourth and final aim, comprehensive examination of a broad array of imaging fiber bundles including commercially available bundle and custom ordered bundles was presented. This careful characterization of coherent fiber imaging bundles

will contribute to the integration of the developed a/LCI and OCT combined system into an endoscopic probe to detect dysplasia in Barrett's esophagus in a clinical trial. In addition this work will provide valuable insights into the potential application of coherent bundles for general coherent imaging including OCT.

Reference

1. D. Huang, E. A. Swanson, C. P. Lin, J. S. Schuman, W. G. Stinson, W. Chang, M. R. Hee, T. Flotte, K. Gregory, C. A. Puliafito and et al., "Optical coherence tomography," Science **254**(5035), 1178-1181 (1991).

2. Y. Li, J. Jing, E. Heidari, J. Zhu, Y. Q. Qu and Z. P. Chen, "Intravascular Optical Coherence Tomography for Characterization of Atherosclerosis with a 1.7 Micron Swept-Source Laser," Sci Rep-Uk **7**((2017).

3. S. Jackle, N. Gladkova, F. Feldchtein, A. Terentieva, B. Brand, G. Gelikonov, V. Gelikonov, A. Sergeev, A. Fritscher-Ravens, J. Freund, U. Seitz, S. Schroder and N. Soehendra, "In vivo endoscopic optical coherence tomography of the human gastrointestinal tract - Toward optical biopsy," Endoscopy **32**(10), 743-749 (2000).

4. D. MacDougall, J. Farrell, J. Brown, M. Bance and R. Adamson, "Long-range, wide-field swept-source optical coherence tomography with GPU accelerated digital lock-in Doppler vibrography for real-time, in vivo middle ear diagnostics," Biomedical Optics Express **7**(11), 4621-4635 (2016).

5. I. Wada, Y. Shimada, M. Ikeda, A. Sadr, S. Nakashima, J. Tagami and Y. Sumi, "Clinical assessment of non carious cervical lesion using swept-source optical coherence tomography," Journal of Biophotonics **8**(10), 846-854 (2015).

6. O. Assayag, M. Antoine, B. Sigal-Zafrani, M. Riben, F. Harms, A. Burcheri, K. Grieve, E. Dalimier, B. L. de Poly and C. Boccara, "Large Field, High Resolution Full-Field Optical Coherence Tomography: A Pre-clinical Study of Human Breast Tissue and Cancer Assessment," Technol Cancer Res T **13**(5), 455-468 (2014).

7. C. Kut, K. L. Chaichana, J. F. Xi, S. M. Raza, X. B. Ye, E. R. McVeigh, F. J. Rodriguez, A. Quinones-Hinojosa and X. D. Li, "Detection of human brain cancer infiltration ex vivo and in vivo using quantitative optical coherence tomography," Science Translational Medicine **7**(292), (2015).

8. O. M. Carrasco-Zevallos, B. Keller, C. Viehland, L. Shen, G. Waterman, B. Todorich, C. Shieh, P. Hahn, S. Farsiu, A. N. Kuo, C. A. Toth and J. A. Izatt, "Live volumetric (4D) visualization and guidance of in vivo human ophthalmic surgery with intraoperative optical coherence tomography," Sci Rep-Uk **6**((2016).

9. A. M. Zysk, F. T. Nguyen, A. L. Oldenburg, D. L. Marks and S. A. Boppart, "Optical coherence tomography: a review of clinical development from bench to bedside," Journal of Biomedical Optics **12**(5), (2007).

10. B. G. Muller, D. M. de Bruin, M. J. Brandt, W. van den Bos, S. van Huystee, D. J. Faber, D. Savci, P. J. Zondervan, T. M. de Reijke, M. P. Laguna-Pes, T. G. van Leeuwen and J. J. de la Rosette, "Prostate cancer diagnosis by optical coherence tomography: First results from a needle based optical platform for tissue sampling," J Biophotonics (2016).

11. M. Adhi and J. S. Duker, "Optical coherence tomography--current and future applications," Curr Opin Ophthalmol **24**(3), 213-221 (2013).

12. U. Schmidt-Erfurth, S. Klimscha, S. M. Waldstein and H. Bogunovic, "A view of the current and future role of optical coherence tomography in the management of age-related macular degeneration," Eye **31**(1), 26-44 (2017).

13. R. F. Spaide, J. Klancnik and M. J. Cooney, "Retinal Vascular Layers Imaged by Fluorescein Angiography and Optical Coherence Tomography Angiography," Jama Ophthalmol **133**(1), 45-50 (2015).

14. J. R. Maher, O. Chuchuen, M. H. Henderson, S. Kim, M. T. Rinehart, A. D. Kashuba, A. Wax and D. F. Katz, "Co-localized confocal Raman spectroscopy and optical coherence tomography (CRS-OCT) for depth-resolved analyte detection in tissue," Biomed. Opt. Express **6**(6), 2022-2035 (2015).

15. T. Wang, A. McElroy, D. Halaney, D. Vela, E. Fung, S. Hossain, J. Phipps, B. Wang, B. Yin, M. D. Feldman and T. E. Milner, "Dual-modality fiber-based OCT-TPL imaging system for simultaneous microstructural and molecular analysis of atherosclerotic plaques," Biomed. Opt. Express **6**(5), 1665-1678 (2015).

16. T. Liu, Q. Wei, J. Wang, S. Jiao and H. F. Zhang, "Combined photoacoustic microscopy and optical coherence tomography can measure metabolic rate of oxygen," Biomed. Opt. Express **2**(5), 1359-1365 (2011).

17. A. Wax, C. Yang, M. G. Muller, R. Nines, C. W. Boone, V. E. Steele, G. D. Stoner, R. R. Dasari and M. S. Feld, "In situ detection of neoplastic transformation and chemopreventive effects in rat esophagus epithelium using angle-resolved low-coherence interferometry," Cancer Res. **63**(13), 3556-3559 (2003).

18. W. J. Brown, J. W. Pyhtila, N. G. Terry, K. J. Chalut, T. A. D'Amico, T. A. Sporn, J. V. Obando and A. Wax, "Review and recent development of angle-resolved low-coherence interferometry for detection of precancerous cells in human esophageal epithelium," IEEE J. Sel. Top. Quantum Electron. **14**(1), 88-97 (2008).

19. N. G. Terry, Y. Zhu, M. T. Rinehart, W. J. Brown, S. C. Gebhart, S. Bright, E. Carretta, C. G. Ziefle, M. Panjehpour, J. Galanko, R. D. Madanick, E. S. Dellon, D. Trembath, A. Bennett, J. R. Goldblum, B. F. Overholt, J. T. Woosley, N. J. Shaheen and A. Wax, "Detection of dysplasia in Barrett's esophagus with in vivo depth-resolved nuclear morphology measurements," Gastroenterology **140**(1), 42-50 (2011).

20. N. Terry, Y. Zhu, J. K. Thacker, J. Migaly, C. Guy, C. R. Mantyh and A. Wax, "Detection of intestinal dysplasia using angle-resolved low coherence interferometry," J. Biomed. Opt. **16**(10), 106002 (2011).

21. D. Ho, T. K. Drake, R. C. Bentley, F. A. Valea and A. Wax, "Evaluation of hybrid algorithm for analysis of scattered light using ex vivo nuclear morphology measurements of cervical epithelium," Biomed. Opt. Express **6**(8), 2755-2765 (2015).

22. A. L. Clark, A. Gillenwater, R. Alizadeh-Naderi, A. K. El-Naggar and R. Richards-Kortum, "Detection and diagnosis of oral neoplasia with an optical coherence microscope," Journal of Biomedical Optics **9**(6), 1271-1280 (2004).

23. T. S. Ralston, D. L. Marks, P. S. Carney and S. A. Boppart, "Interferometric synthetic aperture microscopy," Nat. Phys. **3**(2), 129-134 (2007).

24. L. B. Liu, J. A. Gardecki, S. K. Nadkarni, J. D. Toussaint, Y. Yagi, B. E. Bouma and G. J. Tearney, "Imaging the subcellular structure of human coronary atherosclerosis using micro-optical coherence tomography," Nat. Med. **17**(8), 1010-U1132 (2011).

25. H. F. Ding, Z. Wang, F. Nguyen, S. A. Boppart and G. Popescu, "Fourier Transform Light Scattering of Inhomogeneous and Dynamic Structures," Phys. Rev. Lett. **101**(23), (2008).

26. T. Kim, R. J. Zhou, L. L. Goddard and G. Popescu, "Solving inverse scattering problems in biological samples by quantitative phase imaging," Laser Photonics Rev. **10**(1), 13-39 (2016).

27. R. L. Shelton, W. Jung, S. I. Sayegh, D. T. McCormick, J. Kim and S. A. Boppart, "Optical coherence tomography for advanced screening in the primary care office," J Biophotonics **7**(7), 525-533 (2014).

28. Y. S. Zhang, J. B. Chang, M. M. Alvarez, G. Trujillo-de Santiago, J. Aleman, B. Batzaya, V. Krishnadoss, A. A. Ramanujam, M. Kazemzadeh-Narbat, F. Chen, P. W. Tillberg, M. R. Dokmeci, E. S. Boyden and A. Khademhosseini, "Hybrid Microscopy: Enabling Inexpensive High-Performance Imaging through Combined Physical and Optical Magnifications," Sci Rep **6**(22691 (2016).

29. J. C. Contreras-Naranjo, Q. S. Wei and A. Ozcan, "Mobile Phone-Based Microscopy, Sensing, and Diagnostics," IEEE J. Sel. Top. Quantum Electron. **22**(3), (2016).

30. S. Knowlton, A. Joshi, P. Syrrist, A. F. Coskun and S. Tasoglu, "3D-printed smartphone-based point of care tool for fluorescence- and magnetophoresis-based cytometry," Lab on a Chip **17**(16), 2839-2851 (2017).

31. C. D. Lu, M. F. Kraus, B. Potsaid, J. J. Liu, W. Choi, V. Jayaraman, A. E. Cable, J. Hornegger, J. S. Duker and J. G. Fujimoto, "Handheld ultrahigh speed swept source optical coherence tomography instrument using a MEMS scanning mirror," Biomed. Opt. Express **5**(1), 293-311 (2013).

32. W. Jung, J. Kim, M. Jeon, E. J. Chaney, C. N. Stewart and S. A. Boppart, "Handheld optical coherence tomography scanner for primary care diagnostics," IEEE Trans Biomed Eng **58**(3), 741-744 (2011).

33. Z. Wang, H. C. Lee, D. Vermeulen, L. Chen, T. Nielsen, S. Y. Park, A. Ghaemi, E. Swanson, C. Doerr and J. Fujimoto, "Silicon photonic integrated circuit swept-source optical coherence tomography receiver with dual polarization, dual balanced, in-phase and quadrature detection," Biomedical Optics Express **6**(7), 2562-2574 (2015).

34. P. Pande, R. L. Shelton, G. L. Monroy, R. M. Nolan and S. A. Boppart, "Low-cost hand-held probe for depth-resolved low-coherence interferometry," Biomedical Optics Express **8**(1), 338-348 (2017).

35. J. M. Schmitt, A. Knuttel and R. F. Bonner, "Measurement of Optical-Properties of Biological Tissues by Low-Coherence Reflectometry," Appl Optics **32**(30), 6032-6042 (1993).

36. A. W. Sainter, T. A. King and M. R. Dickinson, "Effect of target biological tissue and choice of light source on penetration depth and resolution in optical coherence tomography," J. Biomed. Opt. **9**(1), 193-199 (2004).

37. P. Parsa, S. L. Jacques and N. S. Nishioka, "Optical-Properties of Rat-Liver between 350 and 2200 Nm," Appl Optics **28**(12), 2325-2330 (1989).

38. A. M. Smith, M. C. Mancini and S. M. Nie, "BIOIMAGING Second window for in vivo imaging," Nat Nanotechnol **4**(11), 710-711 (2009).

39. K. P. Chan, B. Devaraj, M. Yamada and H. Inaba, "Coherent detection techniques in optical imaging of tissues," Phys Med Biol **42**(5), 855-867 (1997).

40. J. D. Rogers, A. J. Radosevich, J. Yi and V. Backman, "Modeling Light Scattering in Tissue as Continuous Random Media Using a Versatile Refractive Index Correlation Function," IEEE J. Sel. Top. Quantum Electron. **20**(2), (2014).

41. J. M. Schmitt and G. Kumar, "Optical scattering properties of soft tissue: a discrete particle model," Appl Optics **37**(13), 2788-2797 (1998).

42. S. L. Jacques, "Optical properties of biological tissues: a review," Phys Med Biol **58**(11), R37-R61 (2013).

43. J. Fujimoto and W. Drexler, "Introduction to Optical Coherence Tomography," Biol Med Phys Biomed 1-45 (2008).

44. M. Choma, M. Sarunic, C. Yang and J. Izatt, "Sensitivity advantage of swept source and Fourier domain optical coherence tomography," Opt Express **11**(18), 2183-2189 (2003).

45. R. Leitgeb, C. K. Hitzenberger and A. F. Fercher, "Performance of fourier domain vs. time domain optical coherence tomography," Opt. Express **11**(8), 889-894 (2003).

46. J. F. de Boer, B. Cense, B. H. Park, M. C. Pierce, G. J. Tearney and B. E. Bouma, "Improved signal-to-noise ratio in spectral-domain compared with time-domain optical coherence tomography," Optics Letters **28**(21), 2067-2069 (2003).

47. J. A. Izatt and M. A. Choma, "Theory of Optical Coherence Tomography," Biol Med Phys Biomed 47-72 (2008).

48. R. A. Leitgeb, W. Drexler, A. Unterhuber, B. Hermann, T. Bajraszewski, T. Le, A. Stingl and A. F. Fercher, "Ultrahigh resolution Fourier domain optical coherence tomography," Opt. Express **12**(10), 2156-2165 (2004).

49. S. T. Wollman and P. W. Bohn, "Evaluation of Polynomial Fitting Functions for Use with Ccd Arrays in Raman-Spectroscopy," Appl Spectrosc **47**(1), 125-126 (1993).

50. M. Wojtkowski, R. Leitgeb, A. Kowalczyk, T. Bajraszewski and A. F. Fercher, "In vivo human retinal imaging by Fourier domain optical coherence tomography," Journal of Biomedical Optics **7**(3), 457-463 (2002).

51. M. Wojtkowski, V. J. Srinivasan, T. H. Ko, J. G. Fujimoto, A. Kowalczyk and J. S. Duker, "Ultrahigh-resolution, high-speed, Fourier domain optical coherence tomography and methods for dispersion compensation," Opt. Express **12**(11), 2404-2422 (2004).

52. A. F. Fercher, C. K. Hitzenberger, M. Sticker, R. Zawadzki, B. Karamata and T. Lasser, "Dispersion compensation for optical coherence tomography depth-scan signals by a numerical technique," Opt Commun **204**(1-6), 67-74 (2002).

53. A. Wax, C. Yang, V. Backman, K. Badizadegan, C. W. Boone, R. R. Dasari and M. S. Feld, "Cellular organization and substructure measured using angle-resolved low-coherence interferometry," Biophys. J. **82**(4), 2256-2264 (2002).

54. J. W. Pyhtila and A. Wax, "Rapid, depth-resolved light scattering measurements using Fourier domain, angle-resolved low coherence interferometry," Opt. Express **12**(25), 6178-6183 (2004).

55. J. W. Pyhtila, J. D. Boyer, K. J. Chalut and A. Wax, "Fourier-domain angle-resolved low coherence interferometry through an endoscopic fiber bundle for light-scattering spectroscopy," Optics Letters **31**(6), 772-774 (2006).

56. S. K. Yarmoska, S. Kim, T. E. Matthews and A. Wax, "A scattering phantom for observing long range order with two-dimensional angle-resolved Low-Coherence Interferometry," Biomed. Opt. Express **4**(9), 1742-1748 (2013).

57. M. Giacomelli, Y. Z. Zhu, J. Lee and A. Wax, "Size and shape determination of spheroidal scatterers using two-dimensional angle resolved scattering," Opt. Express **18**(14), 14616-14626 (2010).

58. M. G. Giacomelli, K. J. Chalut, J. H. Ostrander and A. Wax, "Review of the Application of T-Matrix Calculations for Determining the Structure of Cell Nuclei With Angle-Resolved Light Scattering Measurements," IEEE J. Sel. Top. Quantum Electron. **16**(4), 900-908 (2010).

59. M. I. Mishchenko, L. D. Travis and D. W. Mackowski, "T-matrix computations of light scattering by nonspherical particles: A review," J Quant Spectrosc Ra **55**(5), 535-575 (1996).

60. Hulst HCvd. Light scattering by small particles: Dover Publications; 1981.

61. S. Kim, S. Heflin, L. A. Kresty, M. Halling, L. N. Perez, D. Ho, M. Crose, W. Brown, S. Farsiu, V. Arshavsky and A. Wax, "Analyzing spatial correlations in tissue using angle-resolved low coherence interferometry measurements guided by co-located optical coherence tomography," Biomedical Optics Express **7**(4), 1400-1414 (2016).

62. B. Barviau, S. Randoux and P. Suret, "Spectral broadening of a multimode continuous-wave optical field propagating in the normal dispersion regime of a fiber," Optics Letters **31**(11), 1696-1698 (2006).

63. H. J. Vanstaveren, C. J. M. Moes, J. Vanmarle, S. A. Prahl and M. J. C. Vangemert, "Light-Scattering in Intralipid-10-Percent in the Wavelength Range of 400-1100 Nm," Appl Optics **30**(31), 4507-4514 (1991).

64. L. Spinelli, M. Botwicz, N. Zolek, M. Kacprzak, D. Milej, P. Sawosz, A. Liebert, U. Weigel, T. Durduran, F. Foschum, A. Kienle, F. Baribeau, S. Leclair, J. P. Bouchard, I. Noiseux, P. Gallant, O. Mermut, A. Farina, A. Pifferi, A. Torricelli, R. Cubeddu, H. C. Ho, M. Mazurenka, H. Wabnitz, K. Klauenberg, O. Bodnar, C. Elster, M. Benazech-Lavoue, Y. Berube-Lauziere, F. Lesage, D. Khoptyar, A. A. Subash, S. Andersson-Engels, P. Di Ninni, F. Martelli and G. Zaccanti, "Determination of reference values for optical properties of liquid phantoms based on Intralipid and India ink," Biomedical Optics Express **5**(7), 2037-2053 (2014).

65. J. R. Mourant, T. Fuselier, J. Boyer, T. M. Johnson and I. J. Bigio, "Predictions and measurements of scattering and absorption over broad wavelength ranges in tissue phantoms," Appl Optics **36**(4), 949-957 (1997).

66. R. C. Chang, P. Johnson, C. M. Stafford and J. Hwang, "Fabrication and characterization of a multilayered optical tissue model with embedded scattering

microspheres in polymeric materials," Biomedical Optics Express **3**(6), 1326-1339 (2012).

67. P. X. Lai, X. Xu and L. H. V. Wang, "Dependence of optical scattering from Intralipid in gelatin-gel based tissue-mimicking phantoms on mixing temperature and time," Journal of Biomedical Optics **19**(3), (2014).

68. A. Gregorieff and H. Clevers, "Wnt signaling in the intestinal epithelium: from endoderm to cancer," Gene Dev **19**(8), 877-890 (2005).

69. J. Lem, N. V. Krasnoperova, P. D. Calvert, B. Kosaras, D. A. Cameron, I. Nicolo, C. L. Makino and R. L. Sidman, "Morphological, physiological, and biochemical changes in rhodopsin knockout mice," Proc. Natl. Acad. Sci. U.S.A. **96**(2), 736-741 (1999).

70. J. W. Pyhtila, H. Ma, A. J. Simnick, A. Chilkoti and A. Wax, "Analysis of long range correlations due to coherent light scattering from in-vitro cell arrays using angle-resolved low coherence interferometry," J. Biomed. Opt. **11**(3), 34022 (2006).

71. A. Wax and J. W. Pyhtila, "In situ nuclear morphology measurements using light scattering as biomarkers of neoplastic change in animal models of carcinogenesis," Dis. Markers **25**(6), 291-301 (2008).

72. Tuchin VV. Tissue optics : light scattering methods and instruments for medical diagnosis. Bellingham, Wash.: SPIE Optical Engineering Press; 2000. xxv, 352 p. p.

73. M. Hunter, V. Backman, G. Popescu, M. Kalashnikov, C. W. Boone, A. Wax, V. Gopal, K. Badizadegan, G. D. Stoner and M. S. Feld, "Tissue self-affinity and polarized light scattering in the Born approximation: A new model for precancer detection," Phys. Rev. Lett. **97**(13), (2006).

74. J. Nature PhysicsJournal of NeuroscienceYi, A. J. Radosevich, J. D. Rogers, S. C. P. Norris, I. R. Capoglu, A. Taflove and V. Backman, "Can OCT be sensitive to nanoscale structural alterations in biological tissue?," Opt. Express **21**(7), 9043-9059 (2013).

75. R. J. Zhou, T. Kim, L. L. Goddard and G. Popescu, "Inverse scattering solutions using low-coherence light," Optics Letters **39**(15), 4494-4497 (2014).

76. P. P. Srinivasan, S. J. Heflin, J. A. Izatt, V. Y. Arshavsky and S. Farsiu, "Automatic segmentation of up to ten layer boundaries in SD-OCT images of the mouse retina

with and without missing layers due to pathology," Biomed. Opt. Express **5**(2), 348-365 (2014).

77. B. Wang, B. Yin, J. Dwelle, H. G. Rylander, 3rd, M. K. Markey and T. E. Milner, "Path-length-multiplexed scattering-angle-diverse optical coherence tomography for retinal imaging," Opt. Lett. **38**(21), 4374-4377 (2013).

78. J. Fujimoto and E. Swanson, "The Development, Commercialization, and Impact of Optical Coherence Tomography," Invest Ophth Vis Sci **57**(9), Oct1-Oct13 (2016).

79. S. Kim, M. Crose, W. J. Eldridge, B. Cox, W. J. Brown and A. Wax, "Design and implementation of a low-cost, portable OCT system," Biomedical Optics Express **9**(3), 1232-1243 (2018).

80. P. Mailankody, R. Battu, A. Khanna, A. Lenka, R. Yadav and P. K. Pal, "Optical coherence tomography as a tool to evaluate retinal changes in Parkinson's disease," Parkinsonism Relat D **21**(10), 1164-1169 (2015).

81. V. Manjunath, J. Goren, J. G. Fujimoto and J. S. Duker, "Analysis of choroidal thickness in age-related macular degeneration using spectral-domain optical coherence tomography," Am J Ophthalmol **152**(4), 663-668 (2011).

82. H. Pohl and H. G. Welch, "The role of overdiagnosis and reclassification in the marked increase of esophageal adenocarcinoma incidence," J Natl Cancer I **97**(2), 142-146 (2005).

83. D. A. Corley, C. D. Jensen, A. R. Marks, W. K. Zhao, J. K. Lee, C. A. Doubeni, A. G. Zauber, J. de Boer, B. H. Fireman, J. E. Schottinger, V. P. Quinn, N. R. Ghai, T. R. Levin and C. P. Quesenberry, "Adenoma Detection Rate and Risk of Colorectal Cancer and Death," New Engl J Med **370**(14), 1298-1306 (2014).

84. J. A. Abrams, R. C. Kapel, G. M. Lindberg, M. H. Saboorian, R. M. Genta, A. I. Neugut and C. J. Lightdale, "Adherence to Biopsy Guidelines for Barrett's Esophagus Surveillance in the Community Setting in the United States," Clin Gastroenterol H **7**(7), 736-742 (2009).

85. M. J. Gora, M. J. Suter, G. J. Tearney and X. D. Li, "Endoscopic optical coherence tomography: technologies and clinical applications [Invited]," Biomedical Optics Express **8**(5), 2405-2444 (2017).

86. Olympus. "Astigmatism Aberrations." Retrieved 2 Jul, 2018, from https://www.olympus-lifescience.com/en/microscope-resource/primer/java/aberrations/astigmatism/.

87. Saleh BEA, Teich MC. Fundamentals of photonics. 2nd ed. Hoboken, N.J.: Wiley Interscience; 2007. xix, 1175 p. p.

88. Lbsen Photonics. "Spectrometer Design Guide." Retrieved 1 Jul, 2018, from https://ibsen.com/technology/spectrometer-design-guide/.

89. Y. M. Wang, Y. H. Zhao, J. S. Nelson, Z. P. Chen and R. S. Windeler, "Ultrahigh-resolution optical coherence tomography by broadband continuum generation from a photonic crystal fiber," Optics Letters **28**(3), 182-184 (2003).

90. T. Q. Xie, D. Mukai, S. G. Guo, M. Brenner and Z. P. Chen, "Fiber-optic-bundle-based optical coherence tomography," Optics Letters **30**(14), 1803-1805 (2005).

91. L. M. Wurster, L. Ginner, A. Kumar, M. Salas, A. Wartak and R. A. Leitgeb, "Endoscopic optical coherence tomography with a flexible fiber bundle," J. Biomed. Opt. **23**(6), 1-8 (2018).

92. J. H. Han and J. U. Kang, "Effect of multimodal coupling in imaging micro-endoscopic fiber bundle on optical coherence tomography," Appl Phys B-Lasers O **106**(3), 635-643 (2012).

93. Collimated Holes. "EMA." Retrieved 2 Jul, 2018, from http://www.collimatedholes.com/ema.html.

94. Z. A. Steelman, S. Kim, E. T. Jelly, M. Crose, K. K. Chu and A. Wax, "Comparison of imaging fiber bundles for coherence-domain imaging," Appl Optics **57**(6), 1455-1462 (2018).

Biography

Sanghoon Kim was born in Seoul, South Korea on April 8th, 1986. He was raised in Changwon City, Gyeongnam, South Korea. At the age of 16, Sanghoon moved to the United States in 2002 to attend St. Anne's-Belfield School in Charlottesville, Virginia. Then he attended Duke University in Durham, North Carolina in 2005. After taking a leave of absence for mandatory military service for South Korea from 2008 to 2010, he graduated in 2012 with B.S.E. degree in biomedical engineering and B.S degree in physics. Upon graduating, he immediately began his graduate studies in biomedical engineering in the lab of Dr. Adam Wax. He expects to defend his dissertation in the summer of 2018. During his time in Dr. Wax's lab, Sanghoon attended and presented at numerous conferences, and has published 10 peer-reviewed papers (listed below).

Publications:

1. **S. Kim**, M. Crose, W. J. Eldridge, B. Cox, W. J. Brown and A. Wax, "Design and implementation of a low-cost, portable OCT system," Biomedical Optics Express 9(3), 1232-1243 (2018).

2. Y. Zhou, Y. Zhao, **S. Kim** and A. Wax, "Spectroscopic OCT: towards an effective tool for distinguishing authentic and artificial Chinese freshwater pearls," Optical Materials Express 8(3), 622-628 (2018).

3. Z. A. Steelman, **S. Kim**, E. T. Jelly, M. Crose, K. K. Chu and A. Wax, "Comparison of imaging fiber bundles for coherence-domain imaging," Applied Optics 57(6), 1455-1462 (2018).

4. Y. Zhao, W. J. Eldridge, J. R. Maher, **S. Kim**, M. Crose, M. Ibrahim, H. Levinson and A. Wax, "Dual-axis optical coherence tomography for deep tissue imaging," Optics Letters 42(12), 2302-2305 (2017).

5. **S. Kim**, S. Heflin, L. A. Kresty, M. Halling, L. N. Perez, D. Ho, M. Crose, W. Brown, S. Farsiu, V. Arshavsky and A. Wax, "Analyzing spatial correlations in tissue using angle-resolved low coherence interferometry measurements guided by co-located optical coherence tomography," Biomedical Optics Express **7**(4), 1400-1414 (2016).

6. J. R. Maher, O. Chuchuen, M. H. Henderson, **S. Kim**, M. T. Rinehart, A. D. Kashuba, A. Wax and D. F. Katz, "Co-localized confocal Raman spectroscopy and optical coherence tomography (CRS-OCT) for depth-resolved analyte detection in tissue," Biomedical Optics Express **6**(6), 2022-2035 (2015).

7. W. J. Brown, **S. Kim** and A. Wax, "Noise characterization of supercontinuum sources for low-coherence interferometry applications," Journal of the Optical Society of America A Optics Image Science and Vision **31**(12), 2703-2710 (2014).

8. D. Ho, **S. Kim**, T. K. Drake, W. J. Eldridge and A. Wax, "Wavelet transform fast inverse light scattering analysis for size determination of spherical scatterers," Biomedical Optics Express **5**(10), 3292-3304 (2014).

9. S. K. Yarmoska**, S. Kim**, T. E. Matthews and A. Wax, "A scattering phantom for observing long range order with two-dimensional angle-resolved Low-Coherence Interferometry," Biomedical Optics Express **4**(9), 1742-1748 (2013).

10. **S. Kim**, M. T. Rinehart, H. Park, Y. Z. Zhu and A. Wax, "Phase-sensitive OCT imaging of multiple nanoparticle species using spectrally multiplexed single pulse photothermal excitation," Biomedical Optics Express **3**(10), 2579-2586 (2012).